Measurement of the W boson mass and width with the L3 detector

Measurement of the W boson mass and width with the L3 detector

ACADEMISCH PROEFSCHRIFT

TER VERKRIJGING VAN DE GRAAD VAN DOCTOR
AAN DE UNIVERSITEIT VAN AMSTERDAM
OP GEZAG VAN DE RECTOR MAGNIFICUS
PROF. MR. P.F. VAN DER HEIJDEN
TEN OVERSTAAN VAN EEN DOOR HET COLLEGE VOOR PROMOTIES
INGESTELDE COMMISSIE, IN HET OPENBAAR TE VERDEDIGEN
IN DE AULA DER UNIVERSITEIT
OP VRIJDAG 24 SEPTEMBER 2004, TE 10:00 UUR

door

Sanjeev Vinodpersad Baldew

geboren te Paramaribo, Suriname

promotor: prof. dr. F.L. Linde
co-promotor: dr. ir. P. de Jong

Faculteit der Natuurwetenschappen, Wiskunde en Informatica

The work described in this thesis is part of the research programme of 'het Nationaal Instituut voor Kernfysica en Hoge-Energie Fysica' (NIKHEF) in Amsterdam, the Netherlands.

To my father and mother

Contents

Introduction

According to the ancient Greek philosophers the universe was composed of four elements or roots: Earth, air, fire and water. All matter was believed to be ultimately composed of these four elements of nature.

In about 2000 years, this view has drastically changed. The quest to the ultimate reality of which this universe is composed of has led to new insights. The study of the fundamental structure of matter and its interactions has cumulated in a theory which is at present called the "Standard Model".

This Standard Model has been extensively verified at accelerators, where high energetic particles are brought into collision to probe the internal structure of matter.

In this Standard Model, matter exists of six leptons and six quarks. In addition: each particle has a corresponding anti-particle.

The interactions between these fundamental constituents of the matter particles are described by the exchange of other particles, called bosons. Four types of interactions, also called forces, exist. The strong force is felt by the quarks and is carried by the gluons. Charged particles interact via photons, which are the carriers of the electromagnetic force. The weak force, which is for example responsible for the decay of neutrons, is carried by three heavy bosons W^+, W^- and Z. Gravitation, which is believed to be carried by the graviton, is the weakest of the four forces. From the bosons which carry the forces only the graviton is not yet observed. Except for gravitation the Standard Model has been successful in describing the other three forces in its framework.

The W^+ and W^-, which are denoted in shorthand notation as W, are the subject of study in this thesis. One of the important properties of the W-boson is the mass, which we want to determine.

At the end of the 1960s the theory predicted the existence of the W boson. However, it took until 1983 to produce them in an experiment and observe them directly at the proton-antiproton collider (SPS) at the European Laboratory for particle physics (CERN). This was one of the big triumphs of particle physics.

In 1989 the Large Electron Positron (LEP) accelerator and its four detectors ALEPH, DELPHI, L3 and OPAL became operational. In the first phase of LEP the machine operated at around a centre-of-mass energy ($\sqrt{s}$) of $91\ \mathrm{GeV}$. Since this energy is close to the mass of the Z boson, Z's were produced on resonance.

In 1996 the second phase of LEP started. The centre-of-mass energy was increased to $161\ \mathrm{GeV}$, which is approximately twice the mass of the W boson. This allowed the production of W pairs as $\sqrt{s}$ was higher than the threshold energy of twice the mass of the W boson. Gradually the energy was increased to around $208\ \mathrm{GeV}$.

In this thesis the data taken with the L3 detector is analysed to measure the mass of the W boson. The relevant theoretical aspects are described in chapter 1. The description of particles in the Standard Model framework and how these particles acquire mass is summarised in the first part of this chapter. In the second part of chapter 1 the theoretical facets of the experimental aspects of the production and decay of W bosons are outlined. In chapter 2 LEP and the L3 detector are described. This is followed by the selection of the relevant events for the analysis in chapter 3. Chapter 4 puts the focus on the kinematic fit, which aims to improve the measurement of the observed variables. The W mass analysis results are presented in chapter 5 and the systematic uncertainties in chapter 6. The last chapter is devoted to the comparison with other experiments and an outlook on future experiments is given.

Chapter 1

Theory

The W boson is predicted by the Standard Model in the electroweak sector. In this chapter the electroweak theory Lagrangian, which describes the electroweak interaction, is briefly described. How the particles and especially the W boson acquire mass is explained in more detail. Afterwards the W pair production cross-section and the corrections on the tree-level predictions are given. Also the theoretical uncertainties are discussed.

1.1 Particles and forces

In the universe, matter particles interact with each other by four fundamental forces. These interacting particles experience a certain force by means of a ‘messenger’ particle or mediator of that force.

The fundamental constituents in the Standard Model are the spin-1/2 particles, the fermions which are matter particles, and the spin-1 particles, the bosons which are mediators of the forces. Table 1.1 shows the three fermion generations with their associated electric charge Q. The quantum numbers I_3 and Y will be discussed in the next section. The fundamental forces and their associated bosons are listed in table 1.2 with their spin and electric charge quantum numbers.

The four fundamental forces are believed to arise from the same theoretical framework. They appear to be different because of some symmetry breaking mechanism.

The Standard Model describes the electromagnetic, weak and strong interaction. Gravitation is many orders of magnitude weaker at current energy scales. Therefore it plays no role in this model.

The interactions between the particles can be described by a Lagrangian. Interacting field theory requires the Lagrangian to be locally gauge invariant under some symmetry group. The local gauge invariance of the Lagrangian introduces into the Lagrangian a field associated with the bosons carrying the force. It is not a priori known which symmetry group to use. This can only be deduced from experiment. The underlying gauge symmetry group in the Standard Model appears to be a direct product of three groups, $SU(3)_C \otimes SU(2)_L \otimes U(1)_Y$. The generic special unitary $SU(n)$ groups are represented by $n \times n$ unitary matrices, $U^\dagger U = 1$, with $\det(U) = +1$. This general group has $n^2 - 1$ generators, implying that $n^2 - 1$ gauge fields are predicted by theory.

Table 1.1: *The fermions in the Standard Model are divided into three generations. The left handed and right handed states transform differently under the electroweak symmetry group $SU(2)$. The right handed states are electroweak singlets, while the left handed states are electroweak doublets.*

fermions	generations			I_3	Y	Q
leptons	$\begin{pmatrix} \nu_e \\ e \end{pmatrix}_L$	$\begin{pmatrix} \nu_\mu \\ \mu \end{pmatrix}_L$	$\begin{pmatrix} \nu_\tau \\ \tau \end{pmatrix}_L$	+1/2 -1/2	-1 -1	0 -1
	e_R	μ_R	τ_R	0	-2	-1
quarks	$\begin{pmatrix} u \\ d \end{pmatrix}_L$	$\begin{pmatrix} c \\ s \end{pmatrix}_L$	$\begin{pmatrix} t \\ b \end{pmatrix}_L$	+1/2 -1/2	+1/3 +1/3	+2/3 -1/3
	u_R	c_R	t_R	0	+4/3	+2/3
	d_R	s_R	b_R	0	-2/3	-1/3

$SU(3)_C$ governs the strong force. Quantum Chromo Dynamics (QCD) describes the interaction between quarks, particles carrying colour charge with eight massless gluons that act as a mediator. The gluons also carry colour charge. Hence, the subscript C in $SU(3)_C$, which stands for colour. The consequence of the gluons carrying colour charge is that they also interact with each other.

In the rest of this chapter I will restrict myself to the electroweak sector, i.e. $SU(2)_L \otimes U(1)_Y$. The bosons of the electroweak interaction are the γ, Z and the W^- and W^+. The photon, γ, is massless and is the mediator for the electromagnetic force. The Z and W are massive gauge bosons for the weak interaction. The way these particles acquire mass will be discussed in the next section.

1.2 Lagrangian of the electroweak theory

Interaction between the particles is introduced in the theory by requiring local gauge invariance of the Lagrangian under the $SU(2)_L \otimes U(1)_Y$ group, the weak isospin and hypercharge symmetry group for the electroweak section. To generate mass for the massive Z and W bosons, the spontaneous symmetry breaking mechanism has to be applied.

The complete Weinberg-Salam model [1, 2] Lagrangian will be built up in 4 steps:

1. In the first step we will consider the local gauge invariance of the particle field and its derivative. This will provide the lepton and quark kinetic energy and will introduce gauge fields and their interaction with these fermions.

2. In the second step the gauge field kinetic energies and self-interactions are added.

3. In the third step the $W^{\pm}$, Z , γ and Higgs masses and their couplings will be introduced by the Higgs mechanism.

Table 1.2: *The four fundamental forces. From top to bottom the interaction strength increases. Only the graviton is not discovered yet. The weak, electromagnetic and strong interactions are described by the Standard Model theory.*

interaction	bosons	spin	electric charge	mass [GeV]
gravitation	G	2	0	0
weak (charged current)	W^+, W^-	1	+1, -1	≈ 80
weak (neutral current)	Z	1	0	≈ 90
electromagnetic	γ	1	0	0
strong	g	1	0	0

4. In the fourth step the fermion masses are generated by their coupling to the Higgs.

These steps will be elaborated here.

Local gauge invariance. Electromagnetic and weak interactions

Left handed fermions, which form an isospin doublet, are noted as L while the right handed fermions, which are isosinglets, are written as R. The derivative ∂L or ∂R does not remain invariant under a $SU(2)_L \otimes U(1)_Y$ gauge transformation group.

The $U(1)_Y$ requires a spin-1 field, B_μ, to ensure gauge invariance. The subscript Y denotes the operator Y which is the generator of $U(1)_Y$ symmetry group. The eigenvalue of Y is defined as:

$$Y = 2(Q - I_3), \tag{1.1}$$

where Q is the electric charge in units of $|e|$, the absolute charge of the electron, and I_3 the third component of the weak isospin I. The hypercharges for the fermions are given in table 1.1.

Analogously the $SU(2)_L$ symmetry group requires the spin-1 field, W_μ^i with $i = 1, 2, 3$, and the three generators τ_i of this group[1].

This results into the covariant derivatives:

$$\mathcal{D}_\mu \equiv \partial_\mu + ig'\frac{Y}{2}B_\mu, \tag{1.2}$$

for the right handed fermions, while:

$$\mathcal{D}_\mu \equiv (\partial_\mu + ig\frac{1}{2}\vec{\tau} \cdot \vec{W}_\mu + ig'\frac{Y}{2}B_\mu), \tag{1.3}$$

[1]In the fundamental representation the generators τ_i are:

$$\tau_1 = \begin{pmatrix} 0 & 1 \\ 1 & 0 \end{pmatrix}, \tau_2 = \begin{pmatrix} 0 & -i \\ i & 0 \end{pmatrix}, \tau_3 = \begin{pmatrix} 1 & 0 \\ 0 & -1 \end{pmatrix}.$$

is the covariant derivative for the left handed fermions

The coupling strengths, g and g', of the gauge fields to the particles must be determined experimentally.

The first term of the electroweak Lagrangian, which includes the lepton and quark kinetic energies and their interactions with the electroweak gauge bosons, is then given by:

$$\mathcal{L}_1 = \overline{L}\gamma^\mu i(\partial_\mu + ig\frac{1}{2}\vec{\tau}\cdot\vec{W}_\mu + ig'\frac{Y}{2}B_\mu)L + \overline{R}\gamma^\mu i(\partial_\mu + ig'\frac{Y}{2}B_\mu)R. \tag{1.4}$$

Kinematic terms of the interacting fields

Now the second term of the electroweak Lagrangian $\mathcal{L}_2$ is added:

$$\mathcal{L}_2 = -\frac{1}{4}\vec{W}_{\mu\nu}\cdot\vec{W}^{\mu\nu} - \frac{1}{4}B_{\mu\nu}B^{\mu\nu}. \tag{1.5}$$

The two terms of the Lagrangian (1.5) contain the kinetic energies of the W, Z and γ. The exact relation between the fields $W^1_\mu, W^2_\mu, W^3_\mu$ and B_μ on the one hand and the physical fields $W^+_\mu, W^-_\mu, Z^0_\mu$ and A_μ on the other hand will become clear below.

The field strength tensors are defined in the following way:

$$B_{\mu\nu} = \partial_\mu B_\nu - \partial_\nu B_\mu, \tag{1.6}$$
$$\vec{W}_{\mu\nu} = \partial_\mu\vec{W}_\nu - \partial_\nu\vec{W}_\mu - g\vec{W}_\mu\times\vec{W}_\nu. \tag{1.7}$$

Due to the non-Abelian character of the $SU(2)_L$ transformation the third term of the field strength tensor in equation (1.7) is necessary to remain invariant. This non-linear term describes an induced self-interaction of the gauge bosons.

Spontaneous symmetry breaking. Boson mass generation

The generation of the W and Z mass and their couplings to the Higgs bosons are contained in:

$$\mathcal{L}_3 = |i(\partial_\mu + ig\frac{1}{2}\vec{\tau}\cdot\vec{W}_\mu + ig'\frac{Y}{2}B_\mu)\Phi|^2 - V(\Phi). \tag{1.8}$$

The masses emerge by means of spontaneous symmetry breaking in the following way.

The minimum assumption is that the the Higgs field forms an isospin doublet of complex scalar fields:

$$\Phi = \begin{pmatrix} \phi^+ \\ \phi^0 \end{pmatrix} = \frac{1}{\sqrt{2}}\begin{pmatrix} \phi_1 + i\phi_2 \\ \phi_3 + i\phi_4 \end{pmatrix}, \tag{1.9}$$

where ϕ_i, $(i = 1, 2, 3, 4)$, are real fields. The associated potential energy with this Higgs field is given by:

$$V(\Phi) = \mu^2|\Phi|^2 + \lambda|\Phi|^4. \tag{1.10}$$

with $\lambda > 0$. To have a theory with spontaneous symmetry breaking we choose $\mu^2 < 0$. The shape of the scalar potential $V(\Phi)$ is shown in figure 1.1.

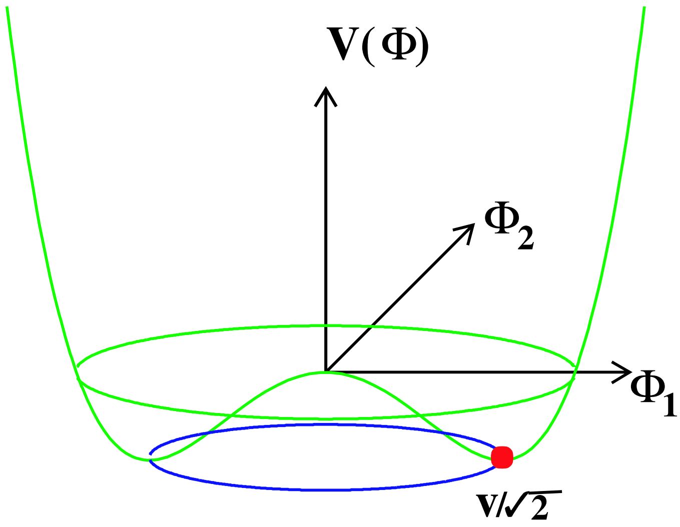

Figure 1.1: *The shape of the Higgs potential if* $\mu^2 < 0$. *The dot represents a chosen minimum* (Φ_0).

This potential has two types of extrema. A local maximum, which therefore does not correspond with the energy minimum, and an infinite number of global minima. The global minimal value of the potential defines the vacuum and is obtained from:

$$|\Phi|^2 \equiv \Phi^\dagger\Phi = \frac{1}{2}(\phi_1^2+\phi_2^2+\phi_3^2+\phi_4^2) = -\frac{\mu^2}{2\lambda}. \tag{1.11}$$

Choosing one solution,

$$\phi_1=\phi_2=\phi_4=0, \quad \phi_3^2=-\frac{\mu^2}{\lambda}\equiv v^2 \qquad \Longrightarrow \qquad \Phi_0=\frac{1}{\sqrt{2}}\begin{pmatrix}0\\ v\end{pmatrix}, \tag{1.12}$$

to represent the ground state of the vacuum, from a infinite number of solutions, breaks the $SU(2)\otimes U(1)_Y$ symmetry, while leaving the vacuum invariant under $U(1)_Q$ symmetry. The scalar field $\Phi(x)$ can be expanded around the vacuum. One can parametrise the fluctuations from the vacuum in terms of the real fields $\vec{\theta}$ and the Higgs field H which are shown in figure 1.1,

$$\Phi(x) = e^{i\vec{\tau}\cdot\vec{\theta}(x)/v}\begin{pmatrix}0\\ \frac{v+H(x)}{\sqrt{2}}\end{pmatrix}, \tag{1.13}$$

where $\vec{\theta}(x)$ and $H(x)$ become zero when $\Phi=\Phi_0$, the vacuum state.

By a certain choice of parametrisation the three real fields $\vec{\theta}(x)$ can be removed. This so-called unitary gauge then yields:

$$\Phi(x) = \begin{pmatrix}0\\ \frac{v+H(x)}{\sqrt{2}}\end{pmatrix}. \tag{1.14}$$

Substituting Φ_0 back into equation (1.8) and ignoring the spatial derivative and potential, one obtains for the terms quadratic in the gauge fields:

$$|(ig\frac{1}{2}\vec{\tau}\cdot\vec{W}_\mu + ig'\frac{Y}{2}B_\mu)\Phi_0|^2 = \frac{1}{8}\left|\begin{pmatrix} gW^3_\mu + g'B_\mu & g(W^1_\mu - iW^2_\mu) \\ g(W^1_\mu + iW^2_\mu) & -gW^3_\mu + g'B_\mu \end{pmatrix}\begin{pmatrix} 0 \\ v \end{pmatrix}\right|^2$$

$$\begin{aligned} &= \tfrac{1}{8}v^2g^2[(W^1_\mu)^2 + (W^2_\mu)^2] + \tfrac{1}{8}v^2(g'B_\mu - gW^3_\mu)(g'B^\mu - gW^{3\mu}) \\ &= \tfrac{1}{8}v^2g^2[(W^1_\mu)^2 + (W^2_\mu)^2] + \tfrac{1}{8}v^2[g^2(W^3_\mu)^2 - 2gg'W^3_\mu B^\mu + g'^2B^2_\mu] \qquad (1.15) \\ &= \tfrac{1}{8}v^2g^2[(W^1_\mu)^2 + (W^2_\mu)^2] + \tfrac{1}{8}v^2[gW^3_\mu - g'B_\mu]^2 + 0[gW^3_\mu + g'B_\mu]^2. \end{aligned}$$

The fields W^i_μ and B_μ are recombined and normalised, and emerge as the physical photon field A_μ, the neutral massive vector particle Z_μ, and the charged doublet of massive vector particles $W^\pm_\mu$:

$$W^\pm_\mu = \frac{1}{\sqrt{2}}(W^1_\mu \mp iW^2_\mu), \qquad (1.16)$$

$$Z_\mu = \frac{gW^3_\mu - g'B_\mu}{\sqrt{g^2 + g'^2}}, \qquad (1.17)$$

$$A_\mu = \frac{gW^3_\mu + g'B_\mu}{\sqrt{g^2 + g'^2}}. \qquad (1.18)$$

Putting these relations in equation (1.15), and identifying the masses of the physical particle results in:

$$(\frac{vg}{2})^2W^+_\mu W^{-\mu} + \frac{1}{2}(\frac{v}{2})^2(g^2 + g'^2)Z_\mu Z^\mu + \frac{1}{2}(0)^2A_\mu A^\mu. \qquad (1.19)$$

Hence, the masses of the gauge bosons from the electroweak sector are:

$$M_{\mathrm{W}^\pm} = \frac{1}{2}vg, \qquad (1.20)$$

$$M_{\mathrm{Z}} = \frac{1}{2}v\sqrt{g^2 + g'^2}, \qquad (1.21)$$

$$M_\gamma = 0. \qquad (1.22)$$

As can be seen from equation (1.17) and (1.18), the (A_μ, Z_μ) and (W^3_μ, B_μ) bases are related by a simple rotation matrix

$$\begin{pmatrix} A_\mu \\ Z_\mu \end{pmatrix} = \begin{pmatrix} \cos\theta_W & \sin\theta_W \\ -\sin\theta_W & \cos\theta_W \end{pmatrix}\begin{pmatrix} B_\mu \\ W^3_\mu \end{pmatrix}, \qquad (1.23)$$

where θ_W is known as the Weinberg or weak mixing angle, and is determined by the coupling strengths,

$$\cos\theta_W = \frac{g}{\sqrt{g^2+g'^2}}, \tag{1.24}$$

$$\sin\theta_W = \frac{g'}{\sqrt{g^2+g'^2}}. \tag{1.25}$$

On the assumption that the Higgs field is a doublet we get:

$$\frac{M_\mathrm{W}}{M_\mathrm{Z}} = \cos\theta_W. \tag{1.26}$$

Thus we can define a parameter ρ,

$$\rho \equiv \frac{M_\mathrm{W}^2}{M_\mathrm{Z}^2\cos^2\theta_\mathrm{W}}, \tag{1.27}$$

which is the relative strength of the neutral and charged current weak interaction. At tree-level for a single weak isospin Higgs doublet we get $\rho = 1$. Other scenarios than the one given above could result in $\rho \neq 1$. Deviations from $\rho = 1$ would indicate new physics.

Following a similar procedure by substituting equation (1.14) into the potential term (1.10) and examining the mass sector, we can read off the mass of the Higgs boson to be:

$$M_\mathrm{H} = v\sqrt{2\lambda}. \tag{1.28}$$

The Higgs mass is not predicted by theory but an unknown parameter of the Standard Model, although v $(246\mathrm{GeV})$ is known from muon decay measurements by the identification:

$$\frac{G_F}{\sqrt{2}} = \frac{g^2}{8M_\mathrm{W}^2} = \frac{1}{2v^2} \quad \Rightarrow \quad v = (\sqrt{2}G_F)^{-\frac{1}{2}} \approx 246\ \mathrm{GeV}, \tag{1.29}$$

while λ is not. Hence M_H has to be determined experimentally.

Fermion mass generation

For the fermions to acquire mass, it is not possible to put a mass term, $-m\overline{\psi}\psi$, in the Lagrangian, because this term would violate gauge invariance. The masses of the fermions are also generated through the mechanism of spontaneous symmetry breaking. For this purpose it is necessary to introduce an interaction of these fermions with the Higgs boson into the Lagrangian for each fermion, these are the Yukawa terms. The additional interaction Lagrangian must be invariant under $SU(2)_L \otimes U(1)_Y$ local gauge transformations, prior to the spontaneous symmetry breakdown. This results into fermion masses which are given by

$$M_f = \frac{v}{\sqrt{2}} g_f. \tag{1.30}$$

The couplings g_f, which are arbitrary numbers for the different fermions, are not predicted. Therefore the masses of the fermions are free parameters of the Standard Model.

1.3 W pair production and cross section in e^+e^- collisions

1.3.1 W pair production

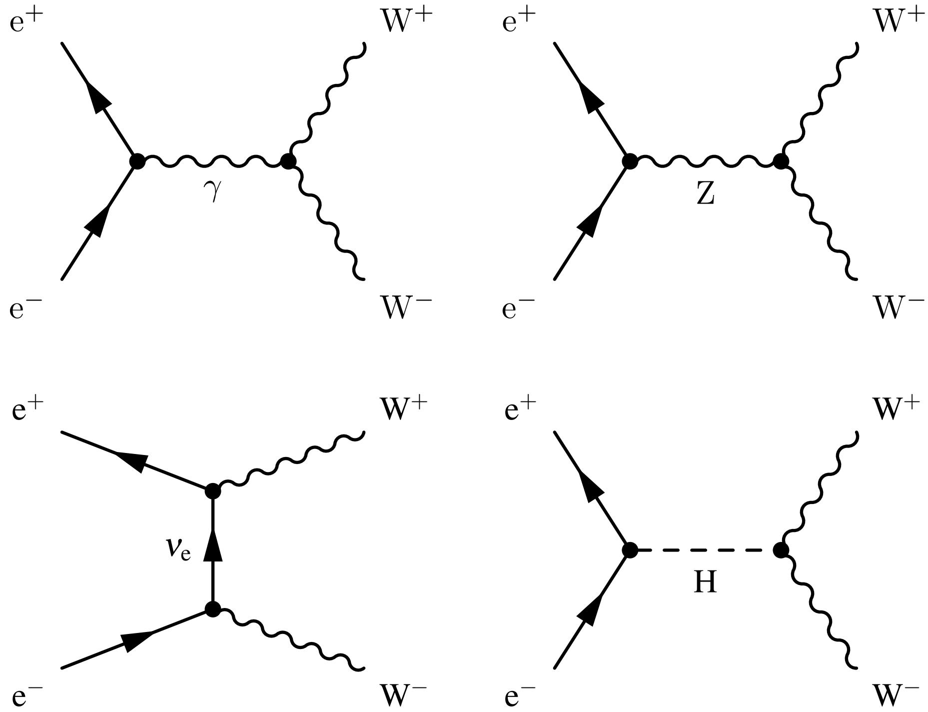

Figure 1.2: *The four Feynman diagrams at lowest order for the W pair production. The top diagrams show the s-channel* γ *and* Z *exchange. At the bottom the t-channel by* ν_e *exchange is shown and the s-channel Higgs exchange, which has a negligible contribution.*

The production of a W pair at tree-level proceeds through the four Feynman diagrams shown in figure 1.2. The Higgs exchange diagram is suppressed by a factor M_e^2/M_W^2 and is negligible. The remaining three diagrams are often referred to as CC03, where CC stands for Charged Current and the 03 for the numbers of contributing diagrams. The W boson is not a stable particle, and consequently has a finite lifetime or, equivalently, a non-zero width Γ_W. The W boson will decay into a fermion antifermion pair. In an e^+e^- collider this allows the following process:

$$e^+ + e^- \to W^- + W^+ \to f_1 + \overline{f_2} + f_3 + \overline{f_4}. \tag{1.31}$$

The leading order cross section for the W boson resonance with a finite width is described by a double integral of the on-shell cross section weighted with Breit-Wigner factors:

$$\sigma^0(s) = \int_0^s \int_0^s ds_- ds_+ \rho(s_-)\rho(s_+)\sigma^0_{\mathrm{CC03}}(s; s_-, s_+), \tag{1.32}$$

where s_- and s_+ are the masses of the two internal W^- and W^+ bosons. If we choose $s_- = s_+ = M_W^2$ then $\sigma^0_{\mathrm{CC03}}(s; s_-, s_+)$ is the on-shell cross section and contains the terms corresponding to the Feynman diagrams in figure 1.2 and their interferences. The full form of $\sigma^0_{\mathrm{CC03}}(s; s_1, s_+)$ can be found in [3].

The finite width, Γ_{W}, of the decaying W is included in the Breit-Wigner densities which are given by

$$\rho(s_\pm) = \frac{1}{\pi}\frac{M_{\mathrm{W}}\Gamma_{\mathrm{W}}}{(s_\pm - M_{\mathrm{W}}^2)^2 + M_{\mathrm{W}}^2\Gamma_{\mathrm{W}}^2}. \tag{1.33}$$

The inclusion of a finite width smears the steep rise near the threshold region, $\sqrt{s} \approx 2M_{\mathrm{W}}$, which is shown in figure 1.3. The correction in this region is about 5% [4] compared with the zero-width cross section.

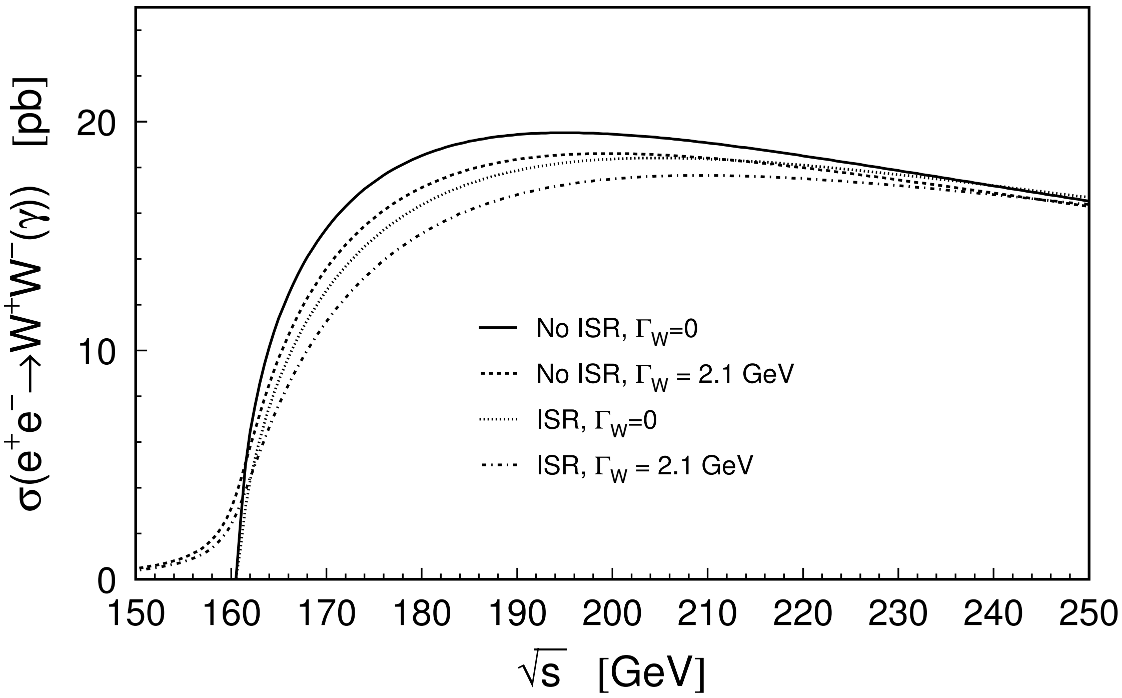

Figure 1.3: *The total cross section as a function of the centre-of-mass energy* $\sqrt{s}$. *The graphs show the effect of inclusion of the finite width of the W boson and initial state radiation (ISR).*

1.3.2 Finite width

The W is an unstable particle which will decay into a lepton and neutrino or into an up-type and down-type quark. The partial width for a W boson decaying into two fermions, (f and f') with mass M_f and $M_{f'}$ is given by [5]:

$$\begin{aligned}\Gamma_{\mathrm{W}\to f\overline{f}'} = \; & N_C^f \tfrac{G_F M_{\mathrm{W}}^3}{6\sqrt{2}\pi}|V_{f\overline{f}'}|^2 R_{QCD} \\ & \times\sqrt{1-\tfrac{(M_f+M_{f'})^2}{M_{\mathrm{W}}^2}}\sqrt{1-\tfrac{(M_f-M_{f'})^2}{M_{\mathrm{W}}^2}}\left[1-\tfrac{M_f^2+M_{f'}^2}{2M_{\mathrm{W}}^2}-\tfrac{(M_f^2-M_{f'}^2)^2}{2M_{\mathrm{W}}^4}\right].\end{aligned} \tag{1.34}$$

The matrix V is the unit matrix for leptonic decay. For the quark sector this matrix V is the CKM matrix, which relates the mass eigen states and the weak eigenstates. N_C^f is the colour factor and equals 1 for the leptons and 3 for the quarks.

The electroweak corrections are incorporated in the width by parametrising the lowest order width in terms of G_F and M_{W} instead of α and $\sin^2\theta$.

$$R_{QCD} = (1 + \frac{\alpha_s(M_{\mathrm{W}}^2)}{\pi}) \tag{1.35}$$

is the QCD correction factor given in the first order of the strong coupling constant α_s, which takes into account QCD colour factor and QCD radiative corrections ($R_{QCD} \equiv 1$ for leptons).

As the fermion masses are much smaller than the W mass, we can neglect them and equation (1.34) simplifies to,

$$\Gamma_{\mathrm{W}\to l\nu} = \frac{G_F M_{\mathrm{W}}^3}{6\sqrt{2}\pi}, \tag{1.36}$$

$$\Gamma_{\mathrm{W}\to q\bar{q}'} = \frac{G_F M_{\mathrm{W}}^3}{2\sqrt{2}\pi}|V_{q\bar{q}'}|^2(1 + \frac{\alpha_s(M_{\mathrm{W}}^2)}{\pi}), \tag{1.37}$$

$$\tag{1.38}$$

and hence with the dominant hadronic decay of W and $V_{u\bar{d}} \sim V_{c\bar{s}}$,

$$\Gamma_{\mathrm{W}} = \Gamma_{W\to \mathrm{e}\nu} + \Gamma_{W\to\mu\nu} + \Gamma_{W\to\tau\nu} + \sum_{q\bar{q}'\neq t,\bar{t}} \Gamma_{W\to q\bar{q}'} = \frac{3G_F M_{\mathrm{W}}^3}{2\sqrt{2}\pi}(1 + \frac{2\alpha_s(M_{\mathrm{W}}^2)}{3\pi}). \tag{1.39}$$

The various ratios,

$$\mathrm{BR}_{\mathrm{W}\to q\bar{q}} = \frac{\sum_{q,\bar{q}\neq \mathrm{t},\bar{\mathrm{t}}} \Gamma_{\mathrm{W}\to q\bar{q}}}{\Gamma_{\mathrm{W}}}, \tag{1.40}$$

$$\mathrm{BR}_{\mathrm{W}\to\ell\nu} = \frac{\Gamma_{\ell\nu}}{\Gamma_{\mathrm{W}}}, \tag{1.41}$$

known as the branching ratios, determine the production rates for the allowed decay channels of the pair W, the decay fraction (DF)

$$\mathrm{DF}_{\mathrm{WW}\to q\bar{q}q\bar{q}} = (\mathrm{BR}_{\mathrm{W}\to q\bar{q}})^2, \tag{1.42}$$

$$\mathrm{DF}_{\mathrm{WW}\to q\bar{q}\ell\nu} = 2(\mathrm{BR}_{\mathrm{W}\to q\bar{q}})(1 - \mathrm{BR}_{\mathrm{W}\to q\bar{q}}), \tag{1.43}$$

$$\mathrm{DF}_{\mathrm{WW}\to\ell\nu\ell\nu} = (1 - \mathrm{BR}_{\mathrm{W}\to q\bar{q}})^2. \tag{1.44}$$

The Standard Model values of the branching ratios (BR) [5] and decay fractions (DF) are given in table 1.3.

1.4 Four fermion final states

At lowest order there are also other diagrams with the same initial state $\mathrm{e}^+\mathrm{e}^-$ and final state $(f_1 + \overline{f_2} + f_3 + \overline{f_4})$, but with a different intermediate state than the doubly resonant W. These diagrams interfere with the CC03 diagrams and should be taken into account, as they change the cross section.

The total number of diagrams depends on the final state and is summarised in table 1.4.

Table 1.3: *The Standard Model branching ratios for the decaying* W *into hadrons or leptons is shown in the left table. The branching fraction of the leptons is for one channel only, i.e.* $l = \mathrm{e}$ *or* μ *or* τ*. The total decay fraction for the fully hadronic, the fully leptonic and the semi leptonic channel is given in the right table* $(l = \mathrm{e} + \mu + \tau)$.

Decay	BR (%)
$q\bar{q}$	67.51
$\ell\nu$	10.83

Decay channel	DF (%)
$q\bar{q}q\bar{q}$	45.58
$q\bar{q}\ell\nu$	43.86
$\ell\nu\ell\nu$	10.56

- The **boldface** numbers are the states with 2 different fermion pairs without the electron or electron neutrino. Because the neutrinos do not couple to photons, there are less than 11 diagrams in case of a final state $l\nu$ pair.

- The roman numbers indicate the states with an electron and electron neutrino. There are additional diagrams with t-channel exchange of the gauge boson.

- The *italic* numbers are the state with two mutually conjugated pairs. The production may also proceed through neutral boson exchange.

Table 1.4: *Numbers of lowest order Feynman diagrams which contribute to the W pair cross section for the different four fermion final states.*

	$\mathrm{u\bar{d}}$	$\mathrm{c\bar{s}}$	$\mathrm{e}^+\nu_e$	$\mu^+\nu_\mu$	$\tau^+\nu_\tau$
$\mathrm{d\bar{u}}$	*43*	**11**	20	**10**	**10**
$\mathrm{e}^-\bar{\nu}_e$	20	20	*56*	18	18
$\mu^-\bar{\nu}_\mu$	**10**	**10**	18	*19*	**9**

Figure 1.4 shows all diagrams contributing to $\mathrm{e^+e^-} \rightarrow u\bar{d}s\bar{c}$. Graphs 1, 6 and 7 are CC03 double resonant diagrams.

The interference of these diagrams with the CC03 diagrams can be reduced by applying cuts for the signal selection, since their contribution is usually limited to particular phase space regions.

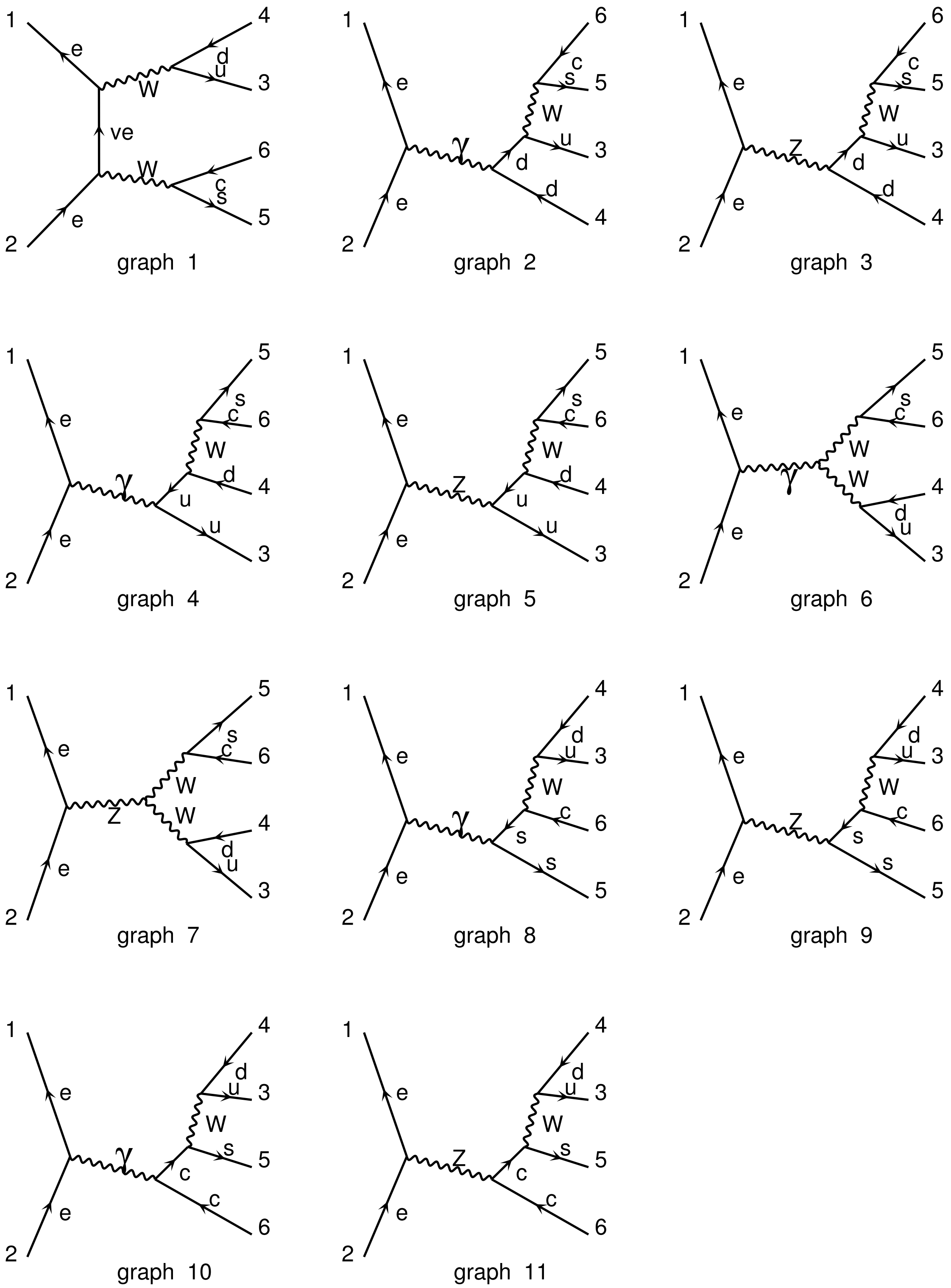

Figure 1.4: *The lowest order Feynman diagrams for the process* $\mathrm{e}^+\mathrm{e}^- \to u\bar{d}s\bar{c}$.

1.5 Theoretical uncertainties

1.5.1 Radiative corrections

To match the current precision of the experimental results, the lowest-order tree-level calculations, including initial state radiation (ISR) and Coulomb corrections, are not enough. To increase the precision in the Monte Carlo programs, more complete radiative corrections have to be included in the calculation. The radiative corrections of the Standard predictions takes into account the higher order diagrams and applies the renormalisation procedure [6].

The radiative corrections to the four fermion process consist of virtual corrections, originating from loop diagrams, and real corrections. These corrections can be factorisable and non-factorisable. Factorisable corrections can be assigned either to the production of the W boson pair or the decay sub-processes, as can be seen in figure (1.5). In the non-factorisable process the production and decay sub-process do not proceed independently. Three examples of non-factorisable processes are shown in figure (1.6). Due to the interference between the production and decay stage their matrix elements do not have two independent W propagators.

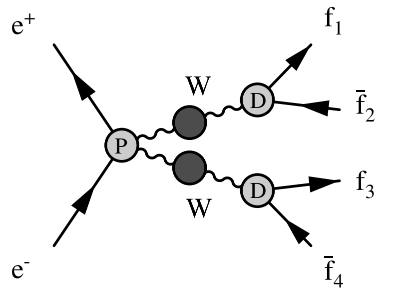

Figure 1.5: *The generic structure of the virtual factorisable corrections to* W *pair production. The dark shaded circles indicate the Breit-Wigner resonances, whereas the light shaded circles denote the Green function for the on-shell production (P) and the on-shell decay (D) sub-processes up to* $\mathcal{O}(\alpha)$ *precision.*

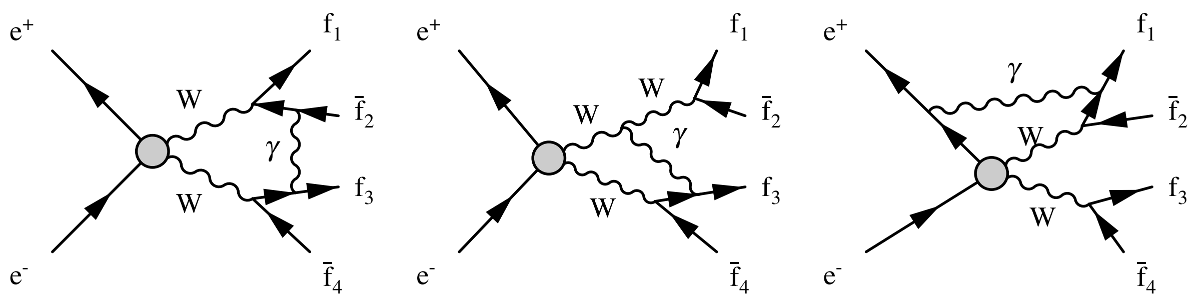

Figure 1.6: *Examples of virtual non-factorisable corrections to* W *pair production. The shaded circles denote the lowest-order Green functions for the production of the virtual* W *boson pair.*

The full electroweak correction to $\mathcal{O}(\alpha)$ is required. However, the full set of $\mathcal{O}(\alpha)$ calculations is not available due to technical problems like $\mathcal{O}(10^3 - 10^4)$ diagrams per four fermion final state and numerical instability amongst others. Therefore, the so-called Double Pole Approximation (DPA) [7] is used. This method is currently implemented in the Monte Carlo programs RacoonWW [8, 9] and YFSWW3 [10, 11]. Figure 1.7 shows the agreement between data and the DPA calculations of RacoonWW and YFSWW3 for the W pair cross section. The difference between both Monte Carlos is estimated to be 0.4%.

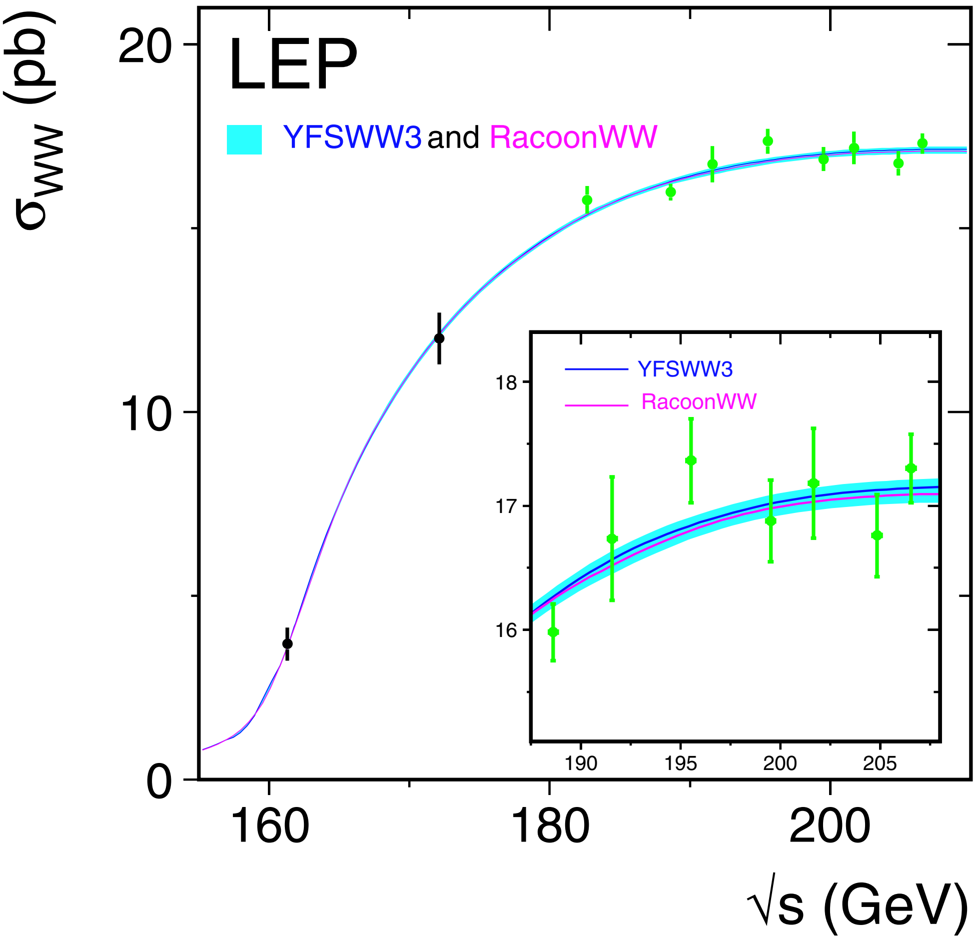

Figure 1.7: *The* W *pair cross sections from the LEP2 data and the Monte Carlos RacoonWW and YFSWW3 are compared. The shaded area indicates the uncertainty on the estimated theoretical prediction. This uncertainty is about* 2% *for* $\sqrt{s} < 170$ GeV *and ranges from* 0.7% *to* 0.4% *above* 170 GeV.

The estimated theoretical uncertainty of the W pair cross section based on the tree-level calculations, while trying to include as much as possible the universal corrections (ISR, Coulomb effect) by constructing an improved Born approximation yields a precision of $\pm 2\%$. The DPA calculations reduce this theoretical error to a level of $\pm 0.5\%$. The total cross section compared to the CC03 cross section prediction is lowered by between 2.5% and 3%.

For the analysis in this thesis the KandY [12] Monte Carlo is used. KandY consists of two complementary event generators: KoralW and YFSWW3. KoralW evaluates all four fermion processes in $\mathrm{e}^+\mathrm{e}^-$ annihilation, $\mathrm{e}^+\mathrm{e}^- \rightarrow 4f$, but with simplified radiative corrections. YFSWW3 evaluates the process $\mathrm{e}^+\mathrm{e}^- \rightarrow \mathrm{WW} \rightarrow 4f$ using Monte Carlo techniques, including $\mathcal{O}(\alpha)$ corrections in DPA calculation for virtual and real corrections as discussed above.

1.5.2 Jet evolution

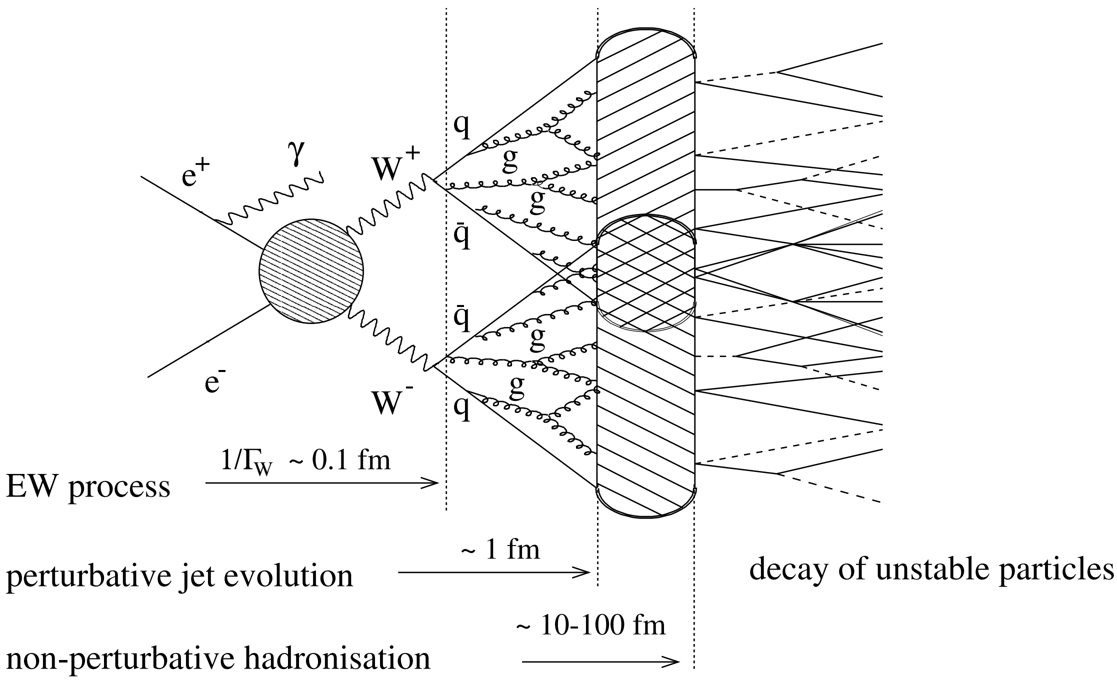

Figure 1.8: *The decay of the* W *into quarks and the subsequent fragmentation and hadronisation jet evolution process. The first phase of the jet evolution can be described by perturbative QCD. The second phase, the non-perturbative hadronisation, is described by phenomenological models. The last phase is the decay of unstable hadrons into stable particles.*

Due to the QCD confinement rule, quarks cannot exist as free particles. The colour-carrying quarks produced in the decay of the W couple to form colourless hadrons. This transformation occurs via the fragmentation and hadronisation process and gives rise to jets of particles.

The above process involves two stages, which are distinguished by different length scales, as is shown in figure 1.8. The first phase can be described by perturbative QCD calculations. The second phase is the non-perturbative region.

Different models exist for both the first and second steps of the fragmentation and hadronisation process. These are implemented in the Monte Carlo programs.

For the first stage two main approaches exist. The first method is the matrix element (ME) method, in which the QCD Feynman diagrams are calculated up to $\mathcal{O}(\alpha_s^2)$, while the other method is the parton shower (PS) approach derived within the framework of the leading logarithmic approximation. The primary quarks which are produced off-shell are iteratively branched into an arbitrary number of virtual partons. JETSET [13] implements both the ME and the PS model. HERWIG [14] and ARIADNE [15] contain the PS model. ARIADNE uses the colour-dipole radiation approach to model the parton shower, whereas JETSET and HERWIG describe the repetitive emission from the individual partons.

For the non-perturbative regime two approaches are employed. JETSET and ARIADNE use the Lund string model: as two partons move apart a stretching string colour field is produced between them. When this string breaks up, a new colourless quark antiquark system is created leading to the formation of a new colour string. Another method, the cluster fragmentation model, is used by HERWIG. In this model the parton showering continues up to a mass scale of a few GeV. The remaining gluons are split into a quark antiquark pair. These pairs form colourless clusters which decay depending on the mass of the fragmenting cluster to clusters of smaller mass or directly into hadrons.

A large fraction of the particles produced in the fragmentation and hadronisation phase are unstable. The mentioned models have a decay scheme for the particles created during hadronisation. These are based on the masses, life times and branching ratios of the hadrons.

All the methods have free model parameters which are determined by tuning them with the Z production data collected at L3 [16–18].

1.5.3 Final state interactions

Final State Interactions (FSI) may alter the phase space when one or two of the W bosons decay hadronically.

The relative short distance of the two decay vertices of the W boson of approximately 0.1 fm in comparison with the distance of > 1 fm over which quarks and gluons hadronise, implies a significant space-time overlap of the wave functions of the two decaying systems. This means that interactions may occur between the decay products of the two W bosons.

Colour Reconnection (CR) and Bose-Einstein Correlations (BEC) are two such cross-talk phenomena. They lead to interactions between particles from different W bosons, modifying the phase space of hadrons, which may alter the reconstructed invariant mass. This has an effect on the W mass and width measurement.

Colour Reconnection

Colour Reconnection (CR) originates from the strong interaction. Colour singlet parton systems of different origin may interact by the strong interaction between the systems. This effect changes the evolution of the two nearby jets which as a consequence perturbs the kinematics of the hadrons.

In the hard perturbative phase, where gluons are emitted with energy $E_g > \Gamma_{\mathrm{W}}$, CR effects are thought to be suppressed [19, 20], while soft gluons, $E_g < \Gamma_{\mathrm{W}}$, could be affected by both decaying W systems, which could lead to non-negligible effects on the hadronisation process.

Several phenomenological models exists for the description of the CR process.

SK I, II [21]: These models are based on colour string rearrangement binding a colour singlet during the fragmentation process.

The string in the SK I model is a flux tube. When these tubes overlap a reconnection can occur. The reconnection probability P_{reco} depends on the overlap volume O of the two strings:

$$P_{reco} = 1 - \exp(-\kappa \cdot O), \tag{1.45}$$

where κ is a free parameter which governs the reconnection probability.

In the SK II model the string has no transverse dimension. The reconnection happens when two strings cross. The reconnection probability is one in this case.

ARIADNE [22]: This model is based on the reconnection of colour dipoles. Parton reconnection only happens if it is energetically favourable, leading to a string with a lower mass.

HERWIG [14]: This model is based on the reconfiguration of the partons before the cluster formation. Reconnection is allowed with a fixed probability when it reduces the sum of the squared size of the formed clusters. The space-time separation of the production vertices of the partons forming the cluster defines the size of a cluster.

Bose-Einstein Correlations

Bose-Einstein Correlation (BEC) is a quantum mechanical phenomenon. For identical bosons quantum mechanics requires the total decay amplitude to be symmetric under the exchange of these bosons. This could induce cross-talk between the two decaying W bosons, since most of the observed particles in a hadronic final state event are pions, spin-1 bosons. An enhanced production of pairs of identical bosons from different W bosons close in phase space could be expected from theory due to amplitude symmetrisation. As a consequence, the measured momenta and therefore the mass is affected by this correlation.

The current available Bose-Einstein models are based on the enhancement of production of identical bosons close in phase space. The LUBOEI [23] algorithm is such a model. The final state particles are reshuffled to reproduce the two particle correlation function. However, energy-momentum conservation is violated. To solve this, additional reshuffling of other pairs of particles is required. Different types of models are developed to incorporate these additional reshuffling, for example BE_0 and BE_{32} [23].

Alternative methods exists to implement BEC besides LUBOEI: the Global reweighting method [24, 25] and Lund string fragmentation models [26, 27]. Only the LUBOEI method was available for this analysis.

1.6 Standard Model relation for G_F and M_W

The muon decay constant, also called the Fermi constant G_F relates the masses M_W and M_Z. It is one of the fundamental parameters in the Standard Model. Its value is determined in the muon decay, $\mu^- \rightarrow \nu_\mu \mathrm{e}^- \overline{\nu}_e$. Fermi made the first attempt to formulate a theory of charged weak interactions [28] where two currents interact in one point. Within the Standard Model the interaction is now coupled by the W boson. Figure 1.9 shows the two concepts.

In the low energy limit where the interaction is essentially described by the four fermion interaction at a point the Fermi constant is:

$$\frac{G_F}{\sqrt{2}} = \frac{g^2}{8M_\mathrm{W}^2} \tag{1.46}$$

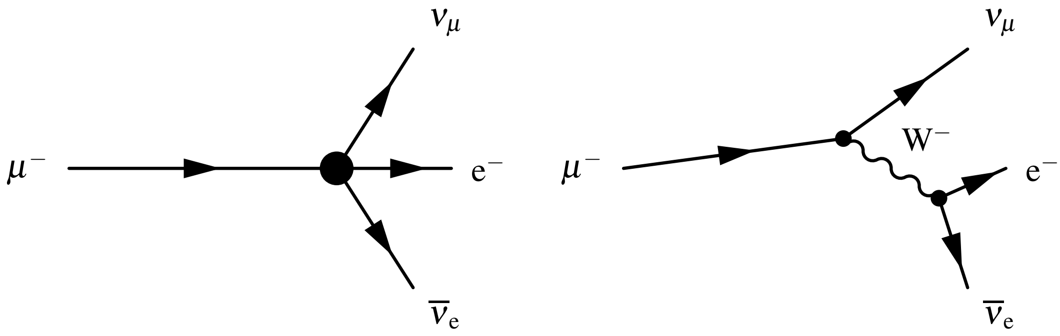

Figure 1.9: *The decay of the muon. The figure on the left shows the muon decay as a contact interaction as in the four fermion theory. On the right side the muon decay is described by the exchange of the* W^- *boson.*

In the Born approximation the Fermi constant G_F relates M_{W} and M_{Z} in the following way:

$$G_F = \frac{\alpha\pi}{\sqrt{2}M_{\mathrm{W}}^2(1 - M_{\mathrm{W}}^2/M_{\mathrm{Z}}^2)}, \tag{1.47}$$

where α is the electromagnetic coupling constant, which is related to the electron charge $e = \sqrt{4\pi\alpha}$. This gives a possibility to extract the W mass from this Standard Model relation.

$$M_{\mathrm{W}} = \frac{\left(\frac{\alpha\pi}{\sqrt{2}G_F}\right)^{\frac{1}{2}}}{\sin\theta_{\mathrm{W}}} = \frac{37.2805(2)}{\sin\theta_{\mathrm{W}}}\ \mathrm{GeV} \tag{1.48}$$

However equation (1.47) is on the Born level. Higher order radiative effects should be included. This is done by a correction factor

$$\frac{1}{1-\Delta r} = \frac{1}{1-\Delta\alpha(M_{\mathrm{Z}}^2)} \cdot \frac{1}{1-\Delta r_w}, \tag{1.49}$$

where Δr consists of different correction terms.

$\Delta\alpha(M_{\mathrm{Z}}^2)$ arises from the Quantum Electro Dynamic (QED) contribution, the photon self-energy, described by fermion loops in the photon propagator. It is usually divided into three separately calculated terms: the leptonic loops, top quark loops and the light quark loops, which is the most uncertain term of the three;

$$\Delta\alpha(M_{\mathrm{Z}}^2) = \Delta\alpha_{leptonic}(M_{\mathrm{Z}}^2) + \Delta\alpha_{top}(M_{\mathrm{Z}}^2) + \Delta\alpha_{had}^{(5)}(M_{\mathrm{Z}}^2). \tag{1.50}$$

The QED corrections are absorbed into α, and taken as the running value of the electromagnetic α at M_{Z},

$$\alpha \equiv \alpha(0) \to \alpha(s) = \frac{\alpha}{1-\Delta\alpha(s)}, \tag{1.51}$$

where $\alpha(M_{\mathrm{Z}}^2) = (127.938 \pm 0.027)^{-1}$ [29]. This yields:

$$G_F = \frac{\alpha(M_{\mathrm{Z}}^2)\pi}{\sqrt{2}M_{\mathrm{W}}^2(1 - M_{\mathrm{W}}^2/M_{\mathrm{Z}}^2)} \cdot \frac{1}{1-\Delta r_w}. \tag{1.52}$$

The variable Δr_w takes into account the weak radiative correction, of which two examples are shown in figure 1.10. The weak radiative corrections are for large top quark and Higgs boson masses $(M_\mathrm{H} \gg M_\mathrm{W})$ given by [30]

$$\begin{aligned}\Delta r_w = -\tfrac{G_F M_\mathrm{W}^2}{8\sqrt{2}\pi^2} \quad & [3\cot^2\theta_\mathrm{W}\tfrac{M_\mathrm{t}^2}{M_\mathrm{W}^2} + (2\cot^2\theta_\mathrm{W} - \tfrac{1}{3})\ln\tfrac{M_\mathrm{t}^2}{M_\mathrm{W}^2} \\ & -\tfrac{11}{3}\ln\tfrac{M_\mathrm{H}^2}{M_\mathrm{W}^2} \\ & +\tfrac{4}{3}\ln\cos^2\theta_\mathrm{W} + \cot^2\theta_\mathrm{W} + \tfrac{41}{18}].\end{aligned} \tag{1.53}$$

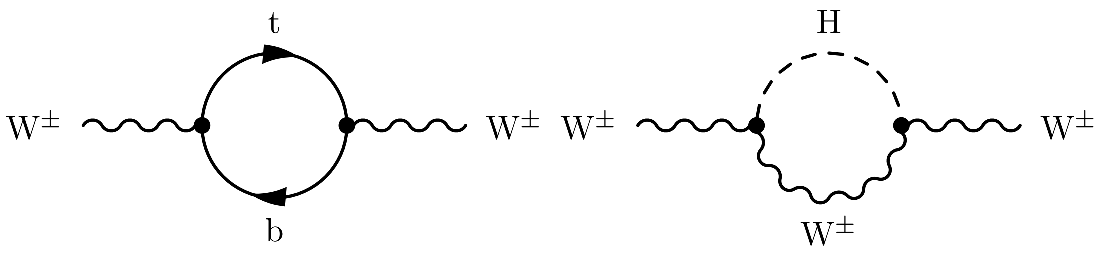

Figure 1.10: *Examples of one loop radiative corrections to the propagator of the W. The left diagram shows a fermionic loop proportional to $M_\mathrm{t}^2/M_\mathrm{W}^2$. The right figure shows a bosonic loop, containing the Higgs, proportional to $\ln(M_\mathrm{H}^2/M_\mathrm{W}^2)$.*

Chapter 2

Experimental setup

In this chapter the main experimental features will be described. First the LEP collider and the beam energy calibration will be discussed. Then the L3 detector's main characteristics will be explained. Finally the event reconstruction and simulation will be described.

2.1 LEP accelerator

The Large Electron Positron (LEP) collider was located at CERN, the European Centre for Particle Physics, near Geneva on the Swiss border with France. At a depth ranging from 50 to 150 meters below the surface, lies the LEP ring with a circumference of $26.7\ \mathrm{km}$. A view of LEP is shown in figure 2.1.

Operation of the LEP machine was started in 1989. In the first period until 1995 LEP operated near the centre-of-mass energy at about $91\ \mathrm{GeV}$ which is close to the Z mass. From 1996 to 2000 the second phase of LEP started. In this LEP2 phase the energy threshold of approximately $161\ \mathrm{GeV}$ of the W-pair production was crossed. Since then the centre-of-mass energy was continuously increased every year. Starting November 2000 the detectors and collider have been dismantled.

2.1.1 LEP injection scheme

In LEP electron and positrons were stored, accelerated and collided head-on. A schematic overview of the LEP injection scheme is shown in figure 2.2.

The LEP beam exists of four bunches, where the particles are grouped, which are several centimeters long and a few millimeters high and wide over most of the LEP ring.

The acceleration of the beam is done in different stages. First, the electrons are generated by an electron gun and accelerated to 200 MeV by the LEP Injector Lineac (LIL) and shot at a tungsten target where positrons are produced. A second linear accelerator gives the beam an energy of 600 MeV. The electron and positrons are stored in the Electron Positron Accumulator ring (EPA), after which the bunches are accelerated to 3.5 GeV in the Proton Synchrotron (PS). In the Super Proton Synchrotron (SPS) these bunches of electrons and positrons are further accelerated to 20 GeV and injected into the LEP ring, where they are finally accelerated to the required beam energies.

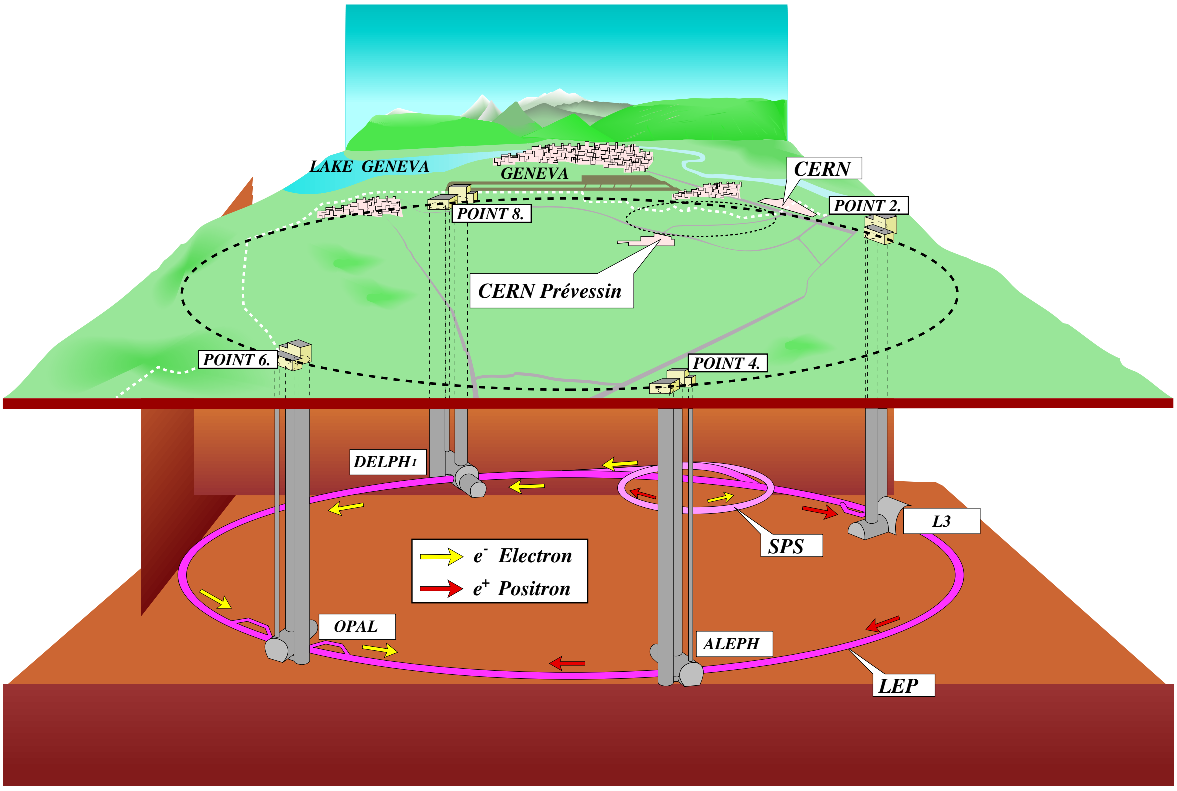

Figure 2.1: *Situation of the LEP collider and the four interaction points.*

The electrons and positrons travel in opposite directions in the vacuum beam pipe. The orbit of these bunches are controlled by 3304 bending magnets. The particles are accelerated by (superconducting) radio frequency cavities (RF cavities). These cavities also compensate for the energy loss due to synchrotron radiation. A system of quadrupoles and sextupole magnets focus the beam. An in-depth description of the LEP accelerator can be found in [31–34].

2.1.2 LEP beam energy calibration

For the W mass measurement a precise knowledge of the LEP beam energy, E_b, is important. The centre-of-mass energy in the collision point is used in the energy conservation constraint in the kinematic fit as shown in chapter 4. In particular the error on the beam energy ΔE_b results in an error ΔM_{W} on the W mass measurement,

$$\frac{\Delta M_{\mathrm{W}}}{M_{\mathrm{W}}} \approx \frac{\Delta E_b}{E_b}. \tag{2.1}$$

To calibrate the beam energy the LEP machine is described by a model containing the RF and magnet configurations as well as external influences like the tides, hydrological strains, geological movements, temperature and leakage currents from railway trains. Due to the different configurations at the different interaction points the beam energy is separately determined in every interaction point and provided to the LEP experiments.

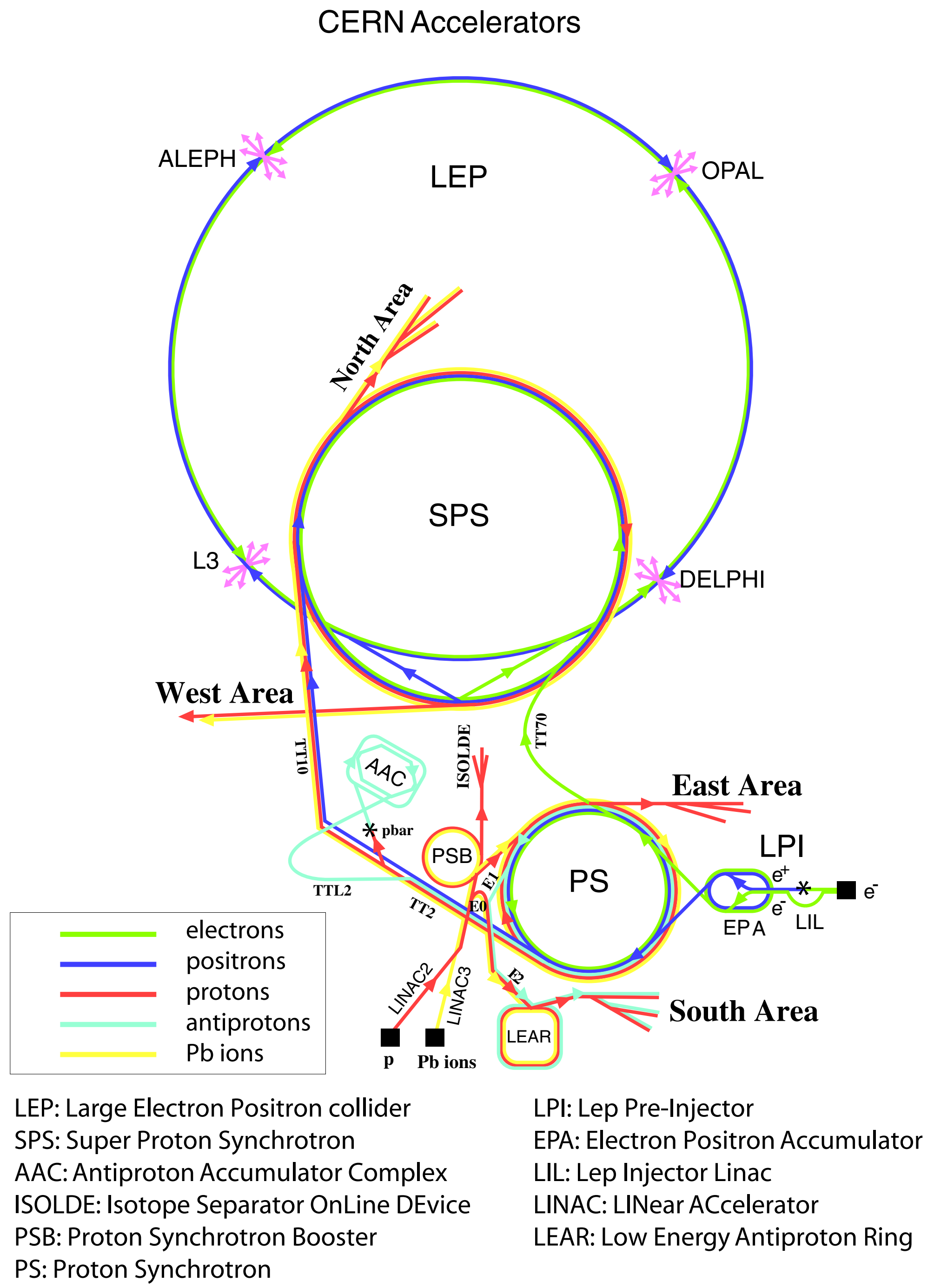

Figure 2.2: *The LEP injection scheme is shown. The different stages of injectors and accelerators of LEP are indicated.*

The first method to determine the LEP beam energy is the resonant depolarisation method. In a e^+e^- storage ring the synchrotron radiation leads to a build-up of transverse polarisation of the electron spin as described by Sokolov-Ternov [35]. Application of a small RF field will destroy the polarisation if the RF frequency matches the natural spin precession frequency. The spin precession frequency ν_s is proportional to the beam energy E_b, [36]

$$\nu_s = \frac{g_e - 2}{2} \cdot \frac{E_b}{M_e} = \frac{E_b}{440.6486(1)\ \mathrm{MeV}}, \tag{2.2}$$

where $(g_e - 2)/2$ is the electron anomalous magnetic moment and M_e its mass. The determination of this frequency yields the beam energy and has an accuracy of $1\ \mathrm{MeV}$.

However, this method is not appropriate for beam energies higher than about $60\ \mathrm{GeV}$. Beyond this energy point the level of spin polarisation becomes too low due to depolarising resonances and the increased beam energy spread.

Two other methods are available for higher beam energies: The Nuclear Magnetic Resonance (NMR) probes and the flux loop measurement.

The beam energy is proportional to the magnetic bending field B along the ring,

$$E_b \sim \oint_l B dl. \tag{2.3}$$

Sixteen NMR probes are placed to measure the field strength inside several main bending dipole magnets.

The flux loop system consists of induction coils in the bending magnets. The average magnetic field is measured by measuring the induced voltage. The flux loops cover in total 95.6% of the bending field.

The NMR probe and flux loop systems are calibrated in the energy region between 41 and 61 GeV where the resonant depolarisation method is available and very precise. To evaluate the beam energies at LEP2 physics conditions the result is extrapolated to higher energy regimes.

The estimated precision for the LEP beam energy determined this way is of the order of $20\ \mathrm{MeV}$ [37], which mainly comes from the difference between the NMR and flux loop measurement and the extrapolation procedure.

Another approach is a beam spectrometer which measures the bending angle, θ, of the beam passing through a magnetic dipole field, B. These variables are related to the beam energy by

$$E_b \sim \int \frac{B ds}{\theta}. \tag{2.4}$$

The integrated field of the placed dipole magnets can be determined with a relative accuracy of about 3×10^{-5}. With a position measurement of the beam with about $1\ \mu\mathrm{m}$ the estimated accuracy of the beam energy combined with the other approaches to determine the beam energy results in an uncertainty below $15\ \mathrm{MeV}$ [36, 37]. Another method is based on measuring the energy loss per turn by synchrotron radiation, which increases with the fourth power of energy. Observables sensitive to the energy loss per turn can be used to determine the beam energy.

2.2 General description of the L3 detector

Charged particles can be reconstructed in a detector by their interaction with the detector material. These interactions can for example be electron-hole pair creation in a semiconductor, gas ionisation, electromagnetic interaction via bremsstrahlung or strong interactions with the nuclei of the detector material. Neutral particles might be detected by their charged decay products. Neutral hadrons can also be detected by strong interactions. Photons are observed by their electromagnetic interaction with the detector material. From every sub-detector or combination of sub-detectors, one can reconstruct the type of particle, the energy, the momentum and the charge of the particle for the analysis. The basic layout of a detector and the possible detection of particles is shown in figure 2.3.

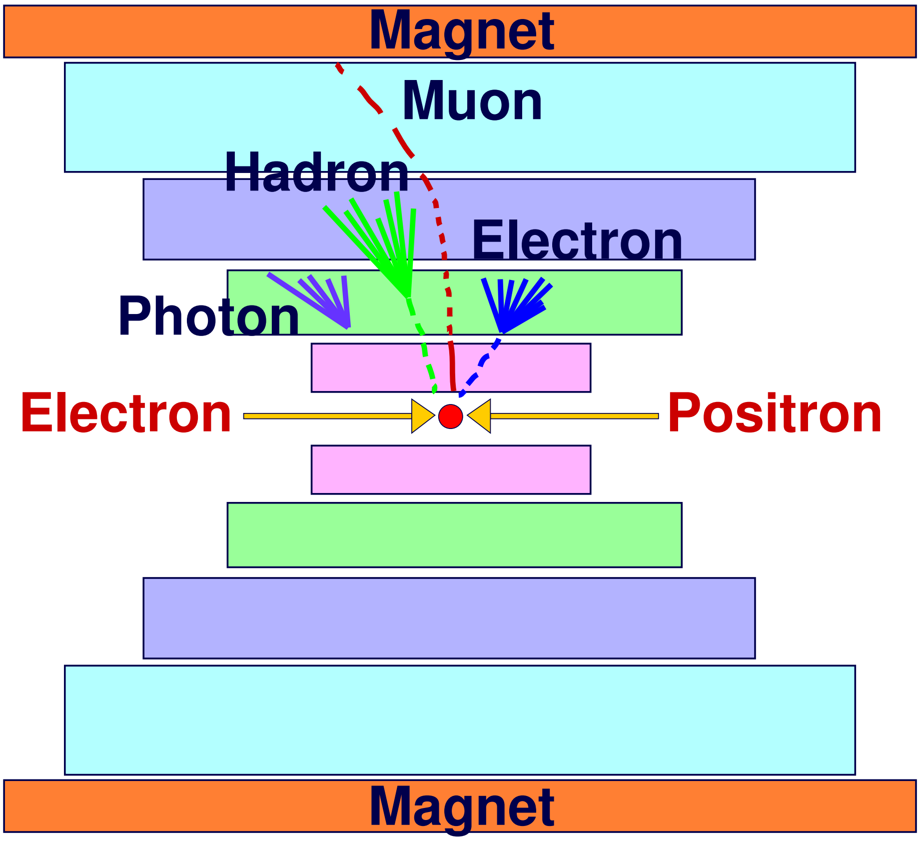

Figure 2.3: *The basic layout of a detector. Every particle leaves a certain signature in the sub-detectors from which one can infer the components of the event.*

LEP has four interaction points, where the electron and positron beams collide. At one of these four interaction points the L3 detector is situated.

The L3 detector lies approximately 50 meters underground in a cavern. The sub-detectors are enclosed in a 16 m high and 14 m long octagonally shaped solenoid magnet with a homogeneous magnetic field of 0.5 T parallel to the beam line. The inner detectors are placed in a 32 m long and 4.45 m diameter steel tube within the solenoid.

The L3 detector consists of various sub-detectors. These sub-detectors are placed cylindrically symmetric along the beam pipe around the interaction point. Moving radially outwards from the interaction point of the L3 detector in figure 2.4 the main detectors are:

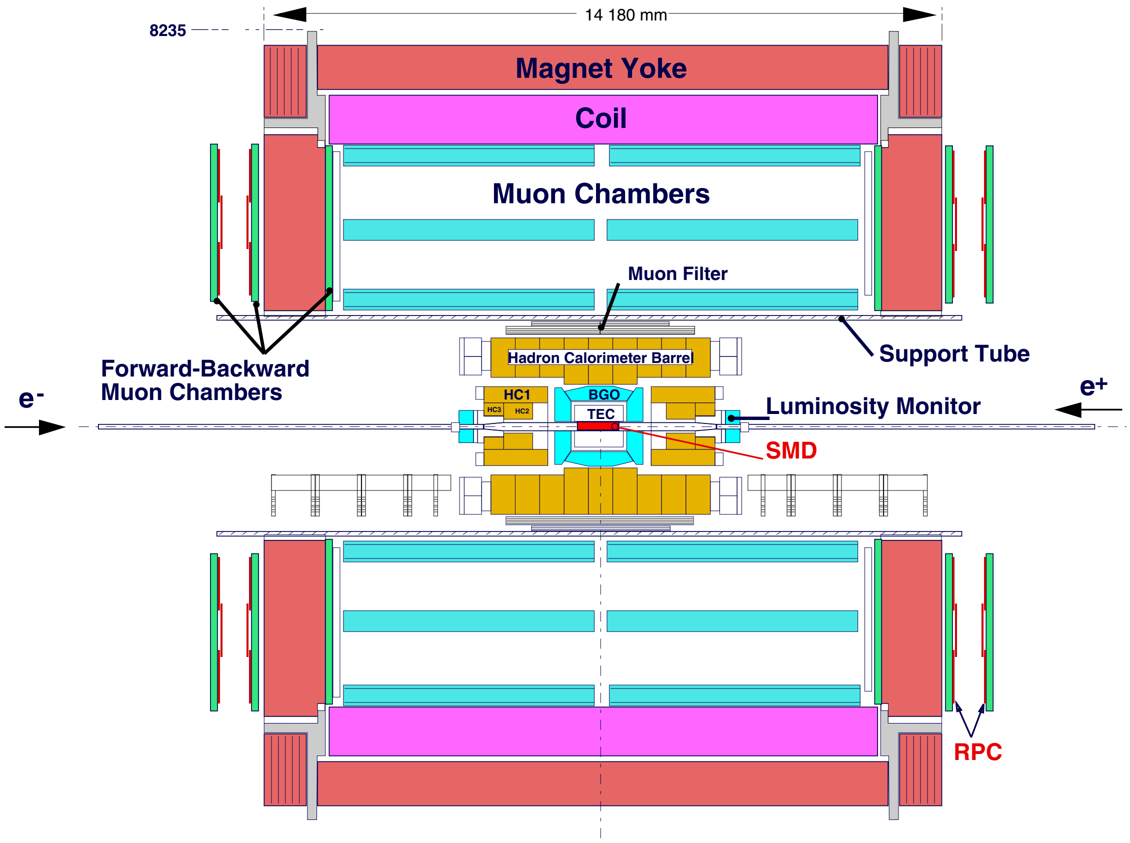

Figure 2.4: *A cross section of the L3 detector. The sub-detectors are enclosed in the L3 magnet.*

- Silicon Micro-vertex Detector (SMD);
- Time Expansion Chamber (TEC);
- Electromagnetic Calorimeter (ECAL);
- Hadronic Calorimeter (HCAL);
- Muon Chambers (MUCH).

These main detectors are complemented by various other sub-detectors and electronics:

- The scintillation counters which are located between the electromagnetic and hadron calorimeters;
- The luminosity monitor (LUMI) in the very forward direction for the measurement of the LEP luminosity, by counting the Bhabha event rate at small polar angle. The cross section for this $\mathrm{e^+e^-\to e^+e^-(\gamma)}$ process is known very accurately from the QED theory;
- The muon filter, to reduce the amount of punch-through, by adding an extra interaction length to the hadron calorimeter;

- The trigger system which is ordered into three levels of increasing complexity;
- Data Acquisition (DAQ) electronics.

In discussing these detectors and in the following it is convenient to introduce a coordinate system. A right handed Cartesian coordinate system is used with the positive x-axis pointing towards the centre of the LEP ring, the positive z-axis along the electron beam and the y-axis orthogonal on the xz-plane pointing to the surface. With respect to this Cartesian system (x, y, z) a spherical polar coordinate system is often used, which is defined in the usual way as in figure 2.5; r is the distance from the origin, the interaction point, θ is the polar angle and ϕ the azimuthal angle.

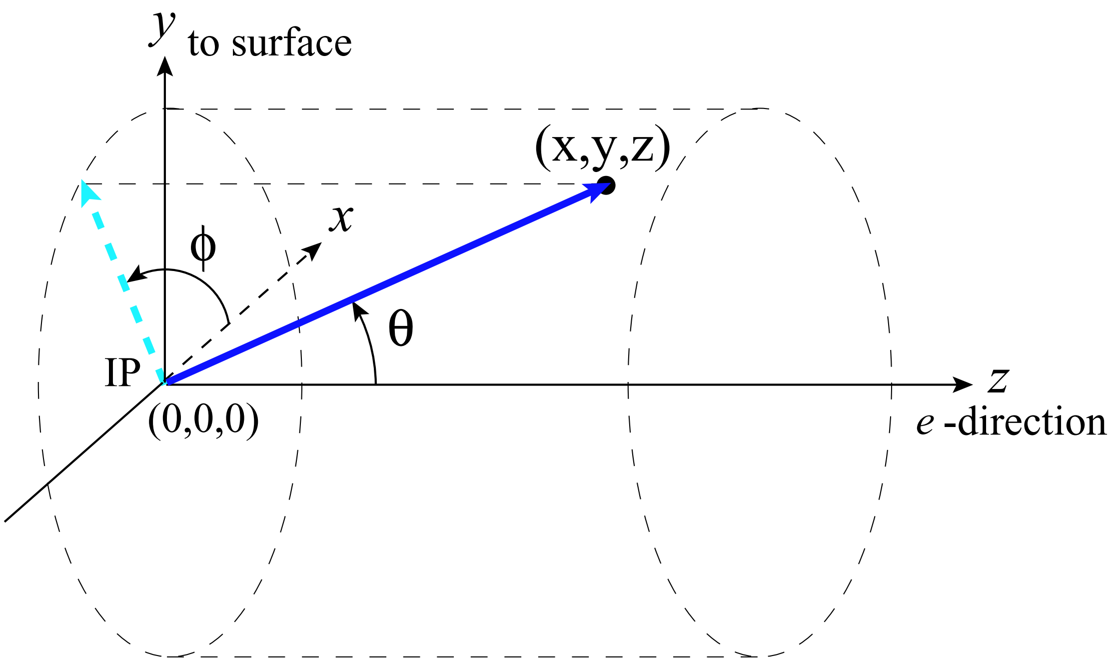

Figure 2.5: *The coordinate system as is used in this thesis. IP is the interaction point*

2.3 Central track detectors

The central track detectors consist of a Silicon Micro-vertex Detector (SMD) and a Time Expansion Chamber (TEC). The central track detectors are designed to detect charged particles.

2.3.1 Silicon microvertex detector

The SMD was installed in 1993 to improve the tracking system and the vertex reconstruction by taking advantage of the fact that the radius of the beam pipe of LEP at the interaction points was reduced from 80 mm to 55 mm [38].

The SMD is installed between the beam pipe and the TEC, as shown in figure 2.6. It consists

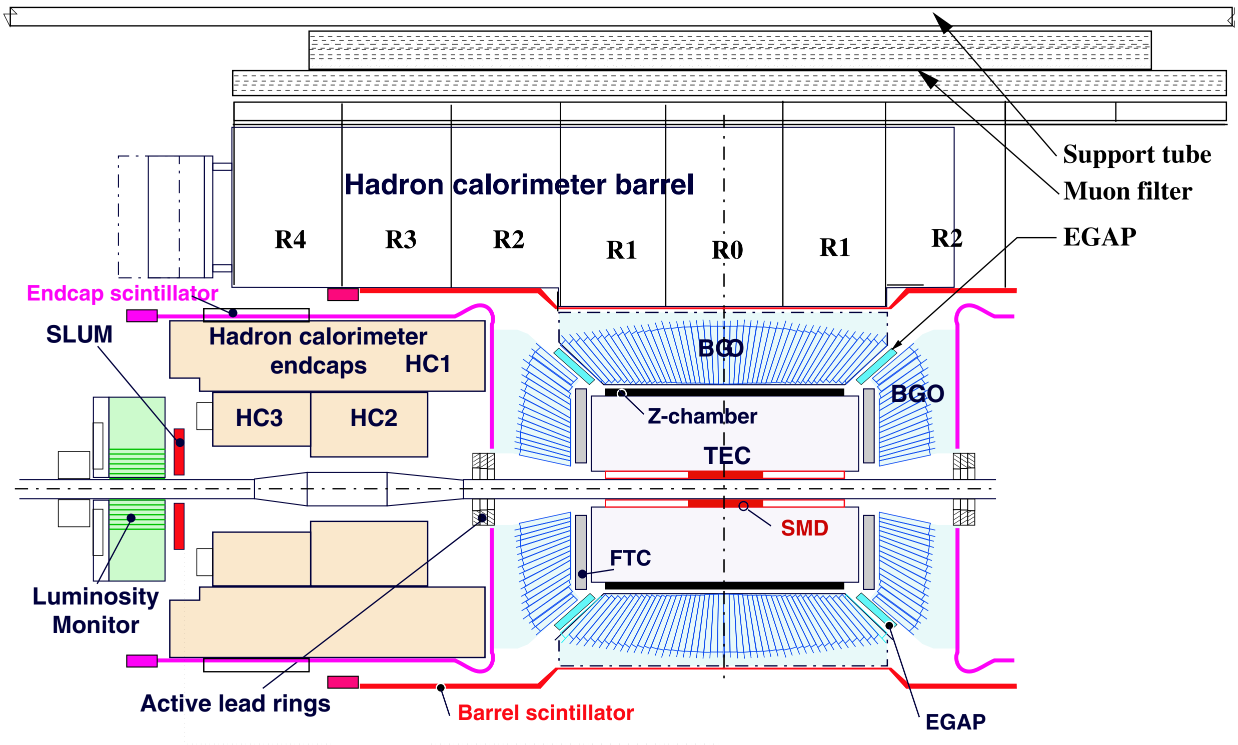

Figure 2.6: *The configuration of the inner detector.*

of two concentric cylindrical layers of silicon. When a charged particle traverses the depleted region of the silicon electron-hole pairs are created, which gives rise to a measurable signal.

The inner layer has a distance of 6.0 cm from the interaction point and the outer layer is at a radius of 7.7 cm from the interaction point. The detector exists of double sided silicon detector with an area of 70×40 mm^2 and a thickness of 300 μm. Four detectors form a ladder. The inner and outer layers are constructed by a total of 24 of such ladders.

The basic unit of the SMD is a half ladder. Subsequent inner half-ladders have an overlap of about $4.5°$ to facilitate the alignment. The outer ladders have been positioned with a stereo angle of $2°$ with respect to the inner layer [39], see figure 2.7.

The strips are implanted parallel to the beam pipe on one side and orthogonally on the other side, thus giving on one side the $r\phi$ measurement and the other side the rz measurement. These strips are referred to as $r\phi$ and z strips. The measurement in the $r\phi$ direction has a resolution of 6 μm and in the z direction 20 μm. The SMD polar angular coverage with this configuration is $22° \leq \theta \leq 158°$.

2.3.2 Time expansion chamber

In the TEC detector the track of a charged particle is reconstructed. The TEC is a multi-wire proportional chamber. It consists of two parts, the inner and outer TEC. The inner TEC is at a distance of 11 cm to 15 cm from the beam line. The radial distance of the outer part to the interaction region is up to 43 cm.

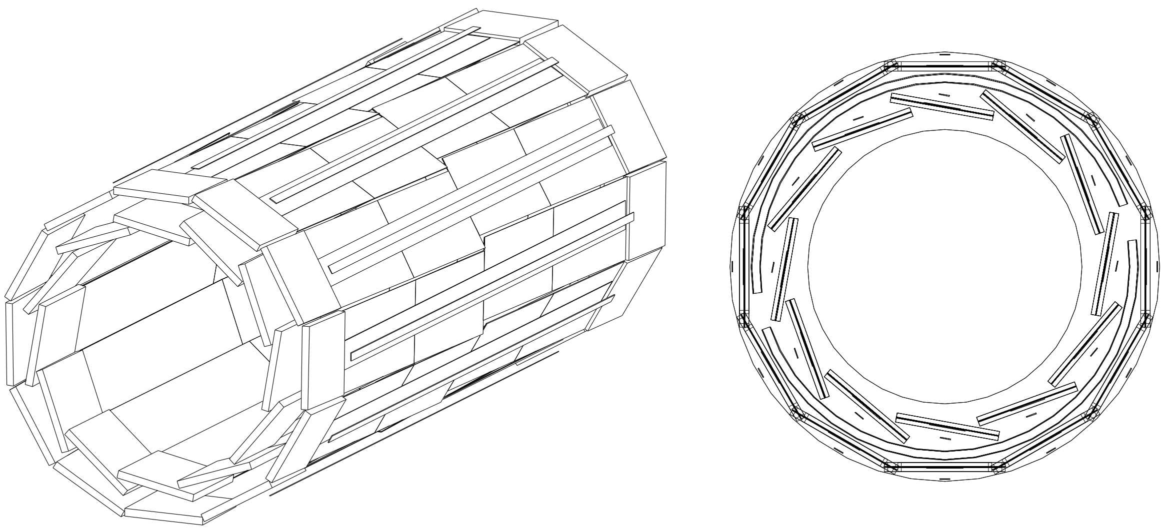

Figure 2.7: *The left figure shows a perspective view of the SMD where one can see the four wafers and the half-ladders. At the right a transverse view of the two SMD layers is seen. The overlap of the subsequent inner layers is clearly shown.*

The inner and outer TEC are divided into sectors by cathodes running parallel to the beam line. The wire configuration of a sector is shown on the right of figure 2.8. Each sector consists of anode wires. Two of these wires are read out on both ends to provide a z measurement. The two wires in each sector are the so-called charge division wires. Between these anode wires there are focus cathodes. On each side of the anode wires is a plane of grid wires at ground potential, which separates the amplification region and drift region electrically, and ensures that the electric field in the drift region is homogeneous. This is depicted on the left of figure 2.8. A group of five grid wires on both sides are isolated from the rest of the grid and are read out to resolve the left right ambiguity.

The inner TEC consists of 12 sectors with 8 anode wires, spaced $4.8\ \mathrm{mm}$ apart. The grid wire plane is at a distance of $3\ \mathrm{mm}$ from the anodes. The outer TEC has 24 sectors and 54 wires in each sector.

To have a low drift velocity a gas mixture should be characterised by a high collision cross section for the drifting electrons with the gas molecules. This is achieved in the TEC by using a gas mixture of 80% carbon-dioxide (CO_2) and and 20% iso-butane (iC_4H_{10}) at a pressure of $1.2\ \mathrm{atm}$ and a temperature of $291\ \mathrm{K}$. The average drift velocity in the amplification region is about $50\ \mu\mathrm{m/ns}$. In the drift region the velocity is about 6 μm/ns [40].

A charged particle traversing the TEC will ionise the gas volume. In the electric field the electrons will drift to the anode while the positive charged ions drift to the cathode. After the electrons have passed the drift region they come in the amplification region where electrons are accelerated and create an avalanche of ionisations. From the drift time the positional information where the ionisation took place can be extracted with an average resolution of about 50 μm. This is obtained by calibrating the detector using low multiplicity Z decays: $\mathrm{e^+e^-} \rightarrow \mathrm{Z} \rightarrow \mathrm{e^+e^-}$ and $\mathrm{e^+e^-} \rightarrow \mathrm{Z} \rightarrow \mu^+\mu^-$.

The momentum p and transverse momentum p_t are related to the magnetic field B and the curvature ρ of the trajectory which a charged particle describe in a plane perpendicular to the

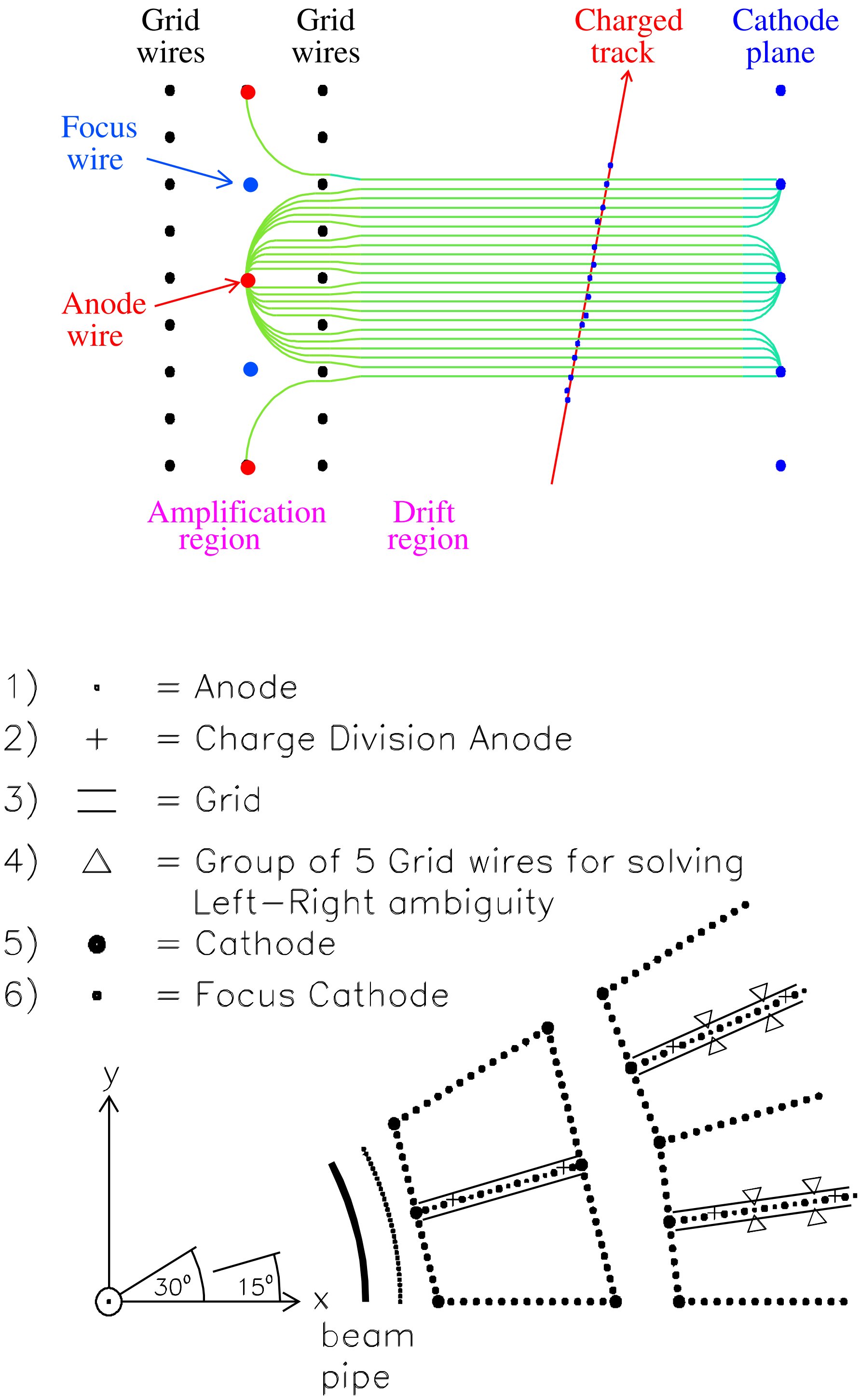

Figure 2.8: *Left: Principle of the TEC. The lines in the drift region are the electric field lines. A charged particle crossing the TEC gives rise to a track. Right: the TEC wire configuration.*

magnetic field. This relation is:

$$p_t = p\sin\theta = \frac{qB}{\rho}. \tag{2.5}$$

The charge q in units of e determines a clock-wise or counter clock-wise curve.

The most sensitive region is in the polar angular range of $44^\circ \leq \theta < 136^\circ$. In this region the charged particle will be measured by all 62 wires. Particles leaving the interaction point with an angle of $\theta < 10^\circ$ or $\theta > 170^\circ$ will completely miss detection by the TEC.

2.4 Calorimeter detectors

In the calorimeters the energies of the particles are measured. The L3 detector has two main calorimeters, the electromagnetic and hadron calorimeter.

Electrons and photons loose all their energy in the electromagnetic calorimeters.

Hadrons penetrate the electromagnetic calorimeter losing only part of their energy after which they are completely absorbed in the hadron calorimeter.

2.4.1 Electromagnetic calorimeter

In the electromagnetic calorimeter (ECAL) the energy and the positions of the electrons and photons are measured. Above a certain energy the electrons and photons loose their energy mainly through electromagnetic interactions with the nuclei. Electrons or positrons will interact with the nuclei of the detector material through which high-energetic Bremsstrahlung photons will be emitted. After interacting with a nucleus a high energetic photon will decay into an electron positron pair. In this way, the cascade of Bremsstrahlung emission and electron-positron pair creation from an incoming energetic electron or photon will create a shower. Below a certain energy (critical energy) the energy loss due to ionisation starts to dominate over Bremsstrahlung and pair production, the shower dies out. At this point ionisation and excitation of the crystal becomes important. The excited atoms emit scintillating light, which can be detected by photo-diodes at the end of the crystal.

The active material of the ECAL consists of about 11000 crystals of Bismuth Germanate ($Bi_4Ge_3O_{12}$, BGO). The threshold energy for the cascade processes is $10\ \mathrm{MeV}$ and its radiation length is $X_0 = 1.12\ \mathrm{cm}$.

These BGO crystals have a length of $24\ \mathrm{cm}$ and are in the form of a truncated pyramid with a front area of $2 \times 2\ \mathrm{cm}^2$ and the back face varying from $2.6 \times 2.6\ \mathrm{cm}^2$ to $2.9 \times 2.9\ \mathrm{cm}^2$. They are mounted with their axis to the interaction region. At the back of each crystal two photo-diodes are glued to detect the BGO scintillating light.

The ECAL is divided into two parts: the barrel and the endcap, see figure 2.6. The barrel has 48 rings and 160 crystals in the ϕ-direction, thus a total of 7680 crystal in the barrel. Each endcap counts a total of 1536 BGO crystals.

The polar angular coverage of the barrel is $42^\circ < \theta < 138^\circ$. The angular region is extended by the endcap where the coverage is $11^\circ < \theta < 38^\circ$ and $142^\circ < \theta < 169^\circ$.

The light of a Xenon lamp is sent through a system of optical fibres to each crystal to calibrate the collection efficiency of the crystals and the readout. An additional calibration is done by shooting H^- ions on a Lithium target. A photon with well known energy is then used to calibrate the BGO crystals. Bhabha events are also used to determine the angular resolution.

For electron and photon energies greater than 1 GeV the energy resolution is better than 2% while a resolution of approximate 1% is reached at energies of 45 GeV. The angular resolution is about 0.5° [41].

The $4°$ gap between the barrel and endcap was filled in 1996 by a new detector, the SPACAL or EGAP, see figure 2.9. It consists of lead brick with scintillating fibres inside. With the extended

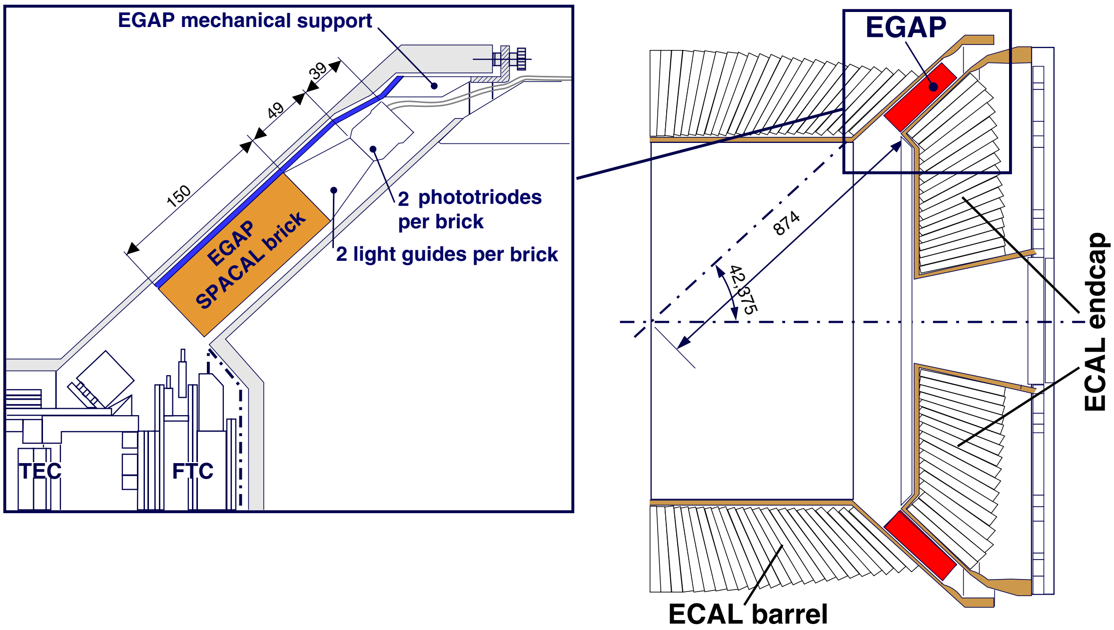

Figure 2.9: *An xz-view on the EGAP detector. The so-called EGAP-region is filled with a SPACAL detector existing of a lead brick with scintillating fibres in it.*

angular coverage the azimuthal angle can be measured for a particle passing through the gap, minimising the chance that a particle escapes detection in this region. The energy resolution in this region is about 5% at 45 GeV [41].

2.4.2 Hadron calorimeter

The hadron calorimeter (HCAL) acts as calorimeter and as a filter, allowing only non-showering particles to reach the muon detector. The energy and direction of the hadrons emerging from the $\mathrm{e^+e^-}$ collisions are measured. The HCAL consists of depleted uranium plates $(5 - 10\ \mathrm{mm})$ as an absorber, with a short nuclear interaction length of about $11\ \mathrm{cm}$ and multi-wire proportional chambers $(5.6\ \mathrm{mm})$ as sampling elements.

The HCAL barrel provides a coverage of the polar angle region of $35° < \theta < 145°$. The barrel is $4725\ \mathrm{mm}$ long with an outer radius of $1795\ \mathrm{mm}$ and an inner radius of $886\ \mathrm{mm}$ for the three inner rings and $979\ \mathrm{mm}$ for the outer rings, see figure 2.10. The endcaps cover $5.5° < \theta < 35°$ and $145° < \theta < 174.5°$. The endcap consists of three parts, an outer ring (HC1) and two inner

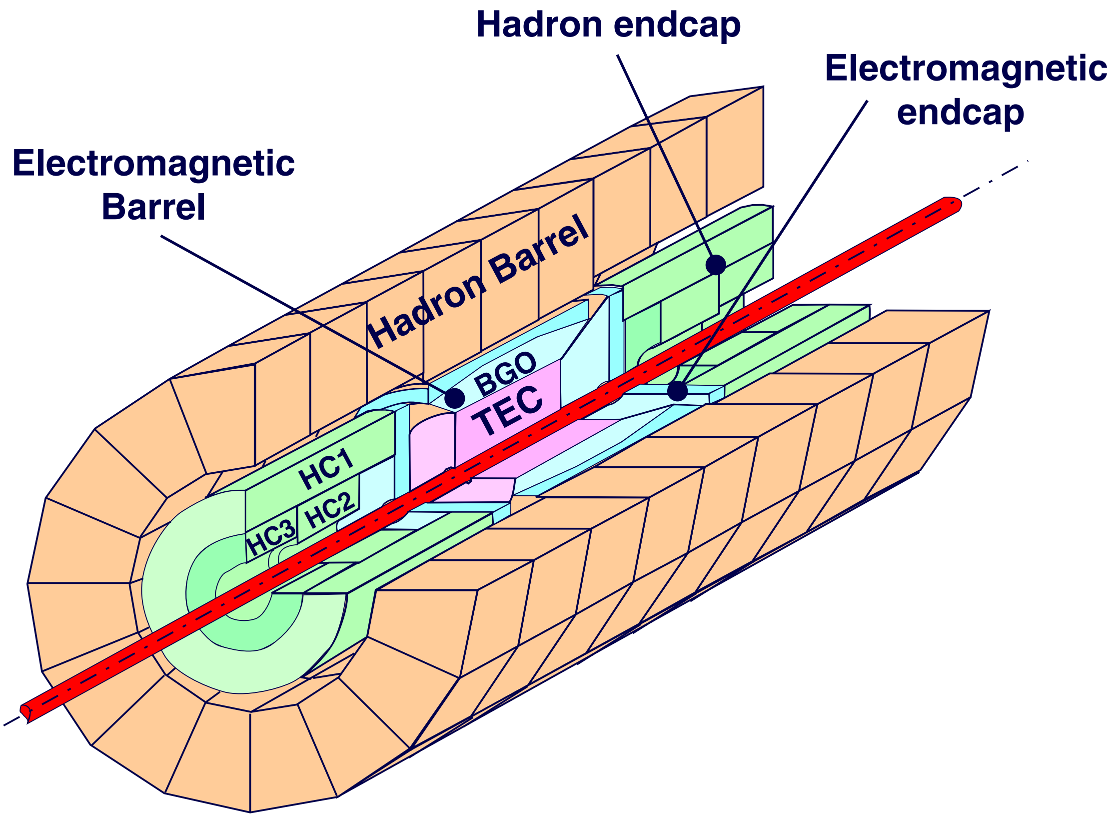

Figure 2.10: *A perspective view of the hadron calorimeter. The 9 rings and 16 modules with the 2 inner rings are clearly shown.*

rings (HC2 and HC3). The splitting into two rings in the longitudinal direction, provides access to the other central detector components. The barrel HCAL is made up of 144 identical modules grouped into 9 rings of 16 modules

A module consists of approximately 60 layers of multi-wire proportional chambers. The gas used consists of 80% Ar and 20% CO_2. The wires in alternate planes are oriented at $90°$, so that one set of wires is parallel to the beam and the other set perpendicular. The wires in each module are grouped into readout cells or towers. The wire grouping is such that there are 10 (8) towers in the radial direction and 9 layers in the ϕ and z direction. The towers cover $\Delta\phi = 2.5°$, $\Delta z = 6$ cm and $\Delta r = 8$ cm. The thickness in terms of the nuclear absorption lengths in the barrel is at least 6, including the electromagnetic calorimeter. For the endcaps it varies between 6 to 7 nuclear absorption lengths.

The resolution for a hadronic jet depends on the jet energy and direction of the jet. This improves with increasing energy and is better in the central part of the detector. Back-to-back events $e^+e^- \to Z \to q\bar{q}$ are studied for the energy calibration. The relative energy resolution for a quark jet of 45 GeV in the centre of the barrel is about 14% while the angular resolutions are about$1.43°$ for θ and about $1.52°$ for ϕ [41].

2.5 Muon spectrometer

The muon spectrometer consists of a barrel and forward-backward component. The barrel muon detector is split along the beam direction into two Ferris wheels placed inside the solenoid magnet. Each wheel is made up of eight octants in three layers, the inner layer (MI) at a distance of 2530 mm from the beam line, the middle layer (MM) at a distance 4010 mm from the beam line and the outer layer (MO) at a distance of 5425 mm from the beam line, see figure 2.11.

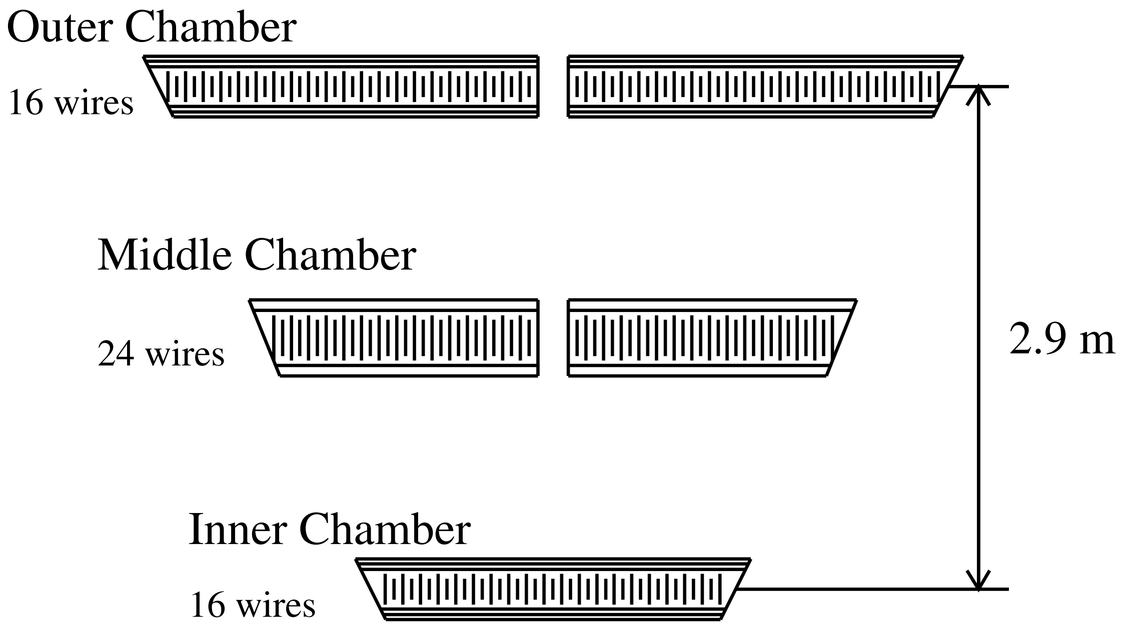

Figure 2.11: *A xy-view of one octant of the muon detector. The three layers and the number of wires per chamber are shown.*

The chambers are drift chambers. Each octant has two chambers next to each other in the outer (MO) layer with 16 wires, two chambers in the middle (MM) layers with 24 wires and one chamber in the inner (MI) layer with 16 wires. The wires in these precision (P) chambers are parallel to the beam axis and measure the $r - \phi$ coordinates of the muon. There is a solenoidal magnetic bending field in the central part of the detector. The gas mixture is 38.5% ethane and 61.5% Ar.

Both sides of the outer and inner chamber are covered by six drift chambers with the sense wires perpendicular to the beam axis, the Z chambers. The Z chambers consist of two layers of drift cells, which are offset by one half cell, to resolve the left-right ambiguity. With these detectors the z coordinate along the beam is measured. The gas mixture is 8.5 % ethane and 91.5% Ar.

The forward-backward (FB) muon chambers consists also of three layers. One is installed inside the magnet door and two outside the magnet door. The gas mixture is 86% Ar, 10% CO_2 and 4% isobutane. Coils provide a toroidal field of 1.2 T in each door.

The polar angle coverage of the barrel muon spectrometer solely is from $44^\circ < \theta < 136^\circ$. The angular region which is only covered by the forward-backward muon spectrometer is from

$22^\circ < \theta < 36^\circ$. Between 36° and 44° a muon is measured in the middle and inner chambers in the barrel and the inner chamber of the forward muon detector. In figure 2.12 a part of the different polar angular regions for muon detection are indicated.

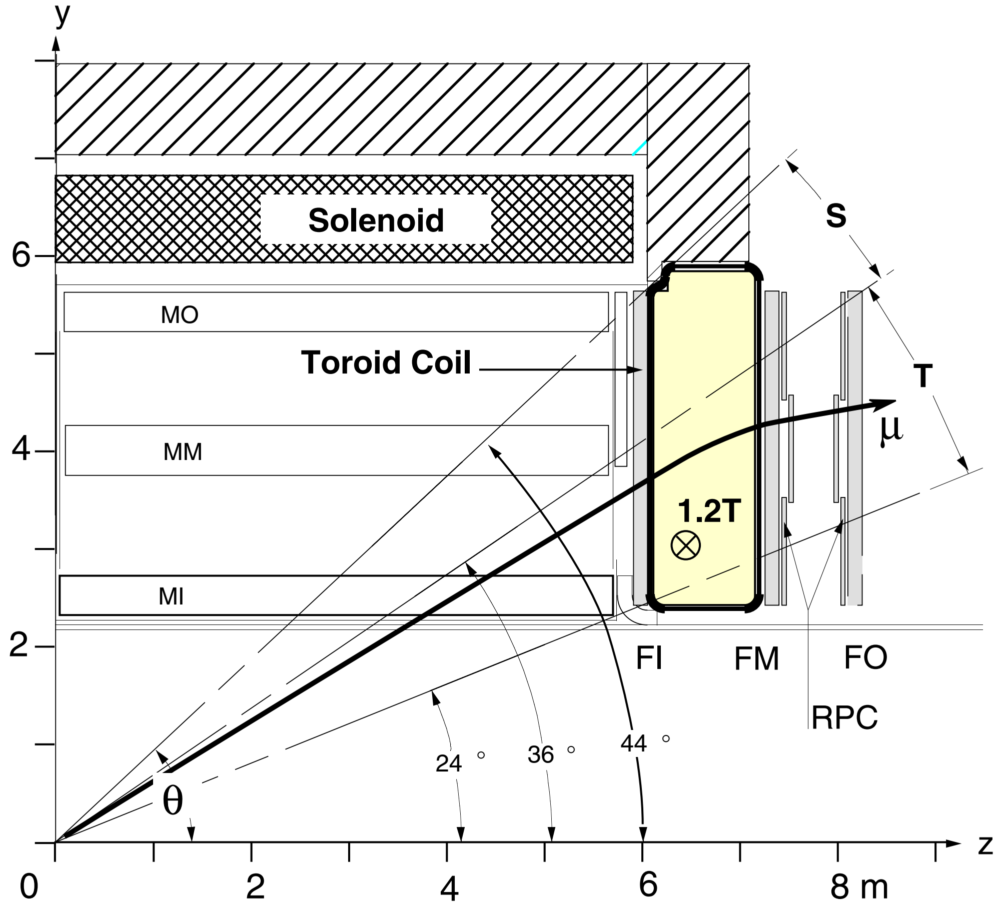

Figure 2.12: *The side view of the FB-muon detector. The inner (FI), middle (FM) and outer (FO) muon chambers are shown. The polar angular regions are indicated by S and T. In the region covered by S the muon is measured by both the barrel and forward chambers. In the angular region T the muon is only covered by the forward region.*

When measured by the three layers in the barrel, a 45 GeV muon has an accuracy of about 3.7%. This resolution is found from di-muon, $\mathrm{e^+e^-} \rightarrow \mathrm{Z} \rightarrow \mu^+\mu^-$, event studies.

2.6 Scintillation counters

The scintillation counters are mounted between the ECAL and the HCAL, as is clearly shown in figure 2.6. These counters are used to measure the time of the particles passing through the detector with respect to the beam crossing time. They are designed to trigger hadronic events and to discriminate di-muon events from cosmic muons which pass near the interaction vertex. The time difference between the hit of two opposite scintillation counters is 5.8 ns for cosmic muons and nil for genuine muon pairs, $\mathrm{e^+e^-} \to \mu^+\mu^-$.

There are 30 barrel scintillation counters and 32 endcap counters extending the polar region coverage down to $25° < \theta < 155°$.

2.7 The L3 trigger

The beam crossing rate at L3 interaction point is 45 kHz. However, not all crossings result in real $\mathrm{e^+e^-}$ collisions. Furthermore, there are background processes which include cosmics, beam gas events, beam wall events, synchrotron radiation, and noise in electronics channels.

The aim of the trigger system is to decide if a genuine $\mathrm{e^+e^-}$ event took place and if affirmative whether the event should be recorded. This is done in three different stages to avoid dead time during data taking.

- The level-1 trigger analyses the trigger data. If a positive decision is taken the data is digitised and recorded in buffer memories otherwise the electronics is cleared. This has to be done within 22 μs, which is the time between two beam crossings. The level-1 trigger neglects correlations between different parts of the detector and is the logical OR of trigger conditions from different sources: calorimetric trigger, muon trigger, TEC trigger and scintillator trigger. The trigger rate is about 20 Hz.

- The level-2 trigger receives information, e.g. charge and drift time, which was not available in time to be processed by the level-1. It can correlate signals from different sub-detectors, improving the level-1 decision. Events that fulfill more than one level-1 trigger condition, are automatically accepted by the level-2 trigger. This trigger will mainly reject background events selected by the level-1 coming from electronic noise, beam gas, beam wall interaction and synchrotron radiation.

  The average rejection rate is about 30%-50% over all accepted level-1 triggers.

- The level-3 trigger uses the complete digitised data. The selection of good events is based on

  - the correlation of the energy deposited in the ECAL and the HCAL;
  - the reconstruction of the muon track;
  - the reconstruction of the vertex in the TEC chamber.

  The output rate of the level-3 trigger is in the order of 2-3 Hz.

Finally if the event is accepted the information from all sub-detectors is collected and built into an event and written to tape.

2.8 Simulation and reconstruction

To make a comparison of the measurement with the theory and to study the effects of the detector response on the event reconstruction, Monte Carlo event generators are used to simulate the signal and background reactions. The KandY [12] event generator is used to simulate the signal of WW production and decay to the four fermion final state. This Monte Carlo combines the four fermion KORALW [42, 43] event generator, based on CC03 matrix elements with the YFSWW3 [10, 11] event generator, which implements the $\mathcal{O}(\alpha)$ radiative correction, including the non-factorisable virtual corrections in the double pole approximation. A complete four fermion description is provided by EXCALIBUR [44, 45]. For hadronic background PYTHIA [46] and KK2F [47] are used. Hadronic and leptonic two-photon collision processes are generated with PHOJET [48, 49] and DIAG36 [50] respectively. KORALZ [51] simulates muon pairs and tau pairs.

A schematic overview of the analysis steps is given in figure 2.13. The real data and simulated data are compared.

The Monte Carlo events are passed through the SIL3 simulation program. SIL3 simulates the L3 detector by simulating the interaction of the generated particles with the L3 detector material using the GEANT [52] program. GEANT models the decay of unstable particles, the effect of energy loss, multiple scattering, creation of $\mathrm{e^+e^-}$ pairs and showering in the detector material. Hadronic interaction processes are simulated by GHEISHA [53], which is embedded in GEANT. The output format is the same as produced and recorded on-line by real events in the detector.

The sample generated this way is called the ideal detector simulation. However, the detector does not have a full efficiency due to problems in the high voltage supplies, inactive crystals, inactive cells or wires, variations in drift gas, noise and so forth. During data taking these time dependent informations are recorded in a database. This database is then used to create a realistic detector simulation form the ideal detector simulation.

The raw data output of the simulation and the real data are transformed by the reconstruction program REL3 into physical quantities like tracks and energy clusters, which can be related to particles and are used in the analysis.

Some of the objects which are created by the reconstruction program are:

Track: The hits in the TEC and SMD are reconstructed to obtain a track using a pattern recognition and fitting algorithm.

ASRC: The set of contiguous hits in the ECAL/HCAL are grouped to form an energy cluster. The adjacent electromagnetic and/or hadronic clusters are combined into a single calometric cluster to form an ASRC (A Smallest Resolvable Cluster).

AMUI: A combination of muon chamber track with hits in the hadron, TEC tracks and electromagnetic calorimeter.

ASJT: An set of adjacent ASRCs is combined by the L3 reconstruction program to a ASJT (A Single JeT). The most energetic cluster is taken as the seed. All clusters within a 30° cone around the seed axis are grouped together. An energy weighted vector sum of these clusters induce a new seed axis and a new 30° cone is defined.

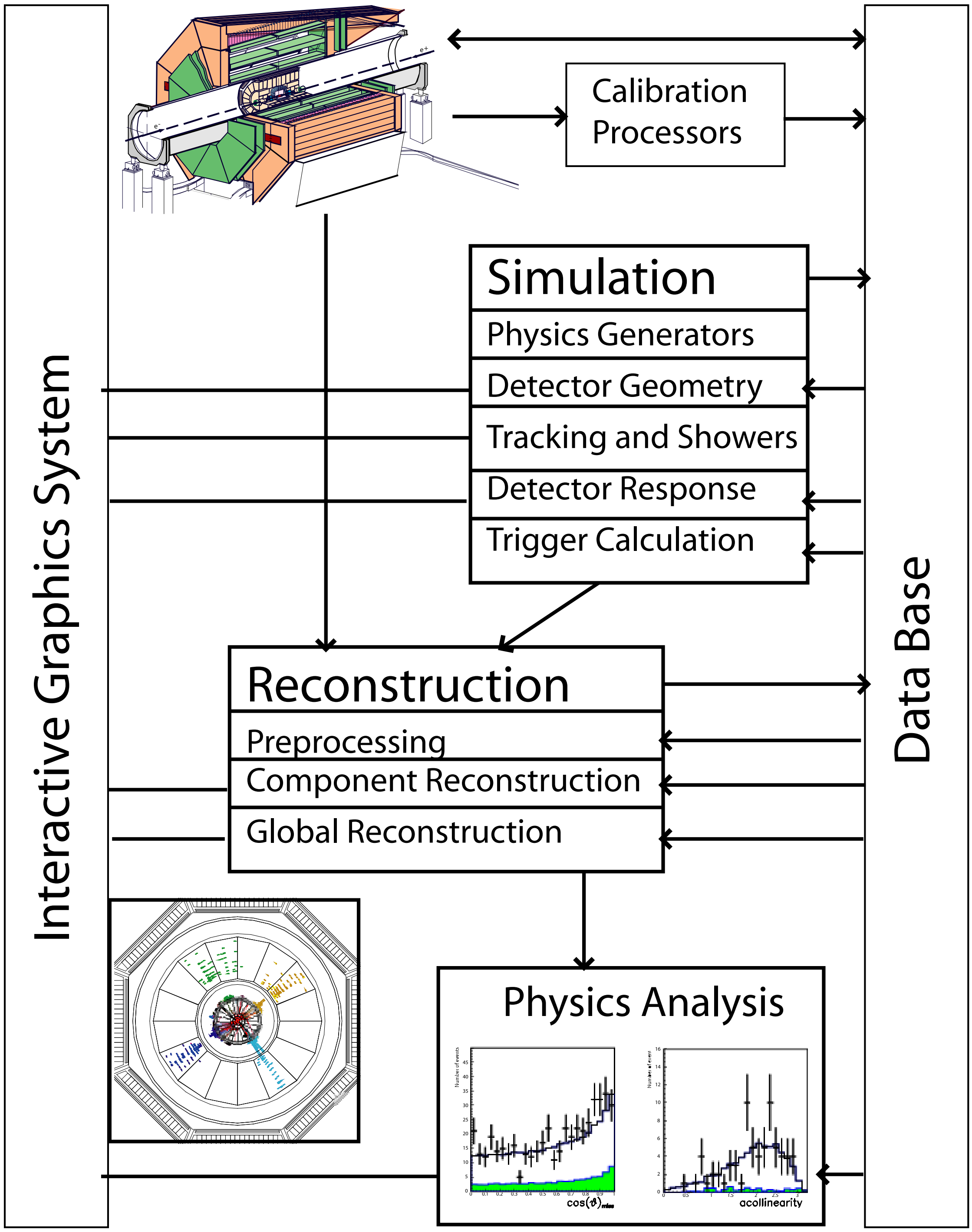

Figure 2.13: *A schematic view of the analysis steps. On one side data is collected from* e^+e^- *collisions and the reconstruction program REL3 reconstructs higher level objects from this output. On the other side Monte Carlo events are generated. The SIL3 program simulates the L3 detector response on this Monte Carlo data set. After this the REL3 program reconstructs the objects in the same sense as the real data. The data analysis is performed and a comparison of real data and Monte Carlo is made and interpreted.*

G-factors

Dead material, cables and gaps in the L3 detector deteriorate the energy measurements in the calorimeters. To improve the measurement an off-line energy calibration is performed.

The G-factors are also introduced to calibrate the ratio between electromagnetic and hadronic component of the shower. They are determined by optimising the jet energy resolution in calibration data and in Monte Carlo.

The real energy deposit in the calorimeters is obtained by scaling the energy deposition with G-factors.

2.9 Luminosity

The luminosity L, is the "brightness" of the beams: the number of possible collisions between e^+ and e^- measured in $\mathrm{cm}^{-2}\mathrm{s}^{-1}$. During data taking the luminosity L is in the order of $10^{31}\ \mathrm{cm}^{-2}\mathrm{s}^{-1}$.

The integrated luminosity is defined by:

$$\mathcal{L} = \int L dt. \tag{2.6}$$

It is determined by measuring the number of small angle Bhabha events, N_{Bhabha}. Since the cross section, σ_{Bhabha}, of this process is known very accurately from QED, the integrated luminosity can be determined from

$$N_{Bhabha} = \sigma_{Bhabha} \cdot \mathcal{L} \cdot \epsilon. \tag{2.7}$$

The efficiency ϵ, corrects for the acceptance and background.

The luminosity monitors are placed at a distance of approximately $3\ \mathrm{m}$ from the interaction point with a polar angular coverage of $1.7°$ to $3.4°$ and are made of BGO crystals. They are complemented with a tracker of single sided silicon wafers, SLUM, which optimises the accuracy of the electron and positron position measurement. The positioning of the LUMI and SLUM is shown in figure 2.6.

This thesis concerns the data of LEP2 taken in the period from 1998 until 2000. The integrated luminosity, $\mathcal{L}$, for each year and mean centre-of-mass energy, $\sqrt{s}$, is given in table 2.1. The total collected luminosity is 629.3 pb^{-1}.

The experimental systematic error on the luminosity arises from event selection criteria, detector geometry and Monte Carlo statistics and is in the order of 0.13%. The theoretical uncertainty from the BHLUMI generator is 0.12% [54]. The total uncertainty on the luminosity varies between 0.18% and 22% [55].

Table 2.1: *Integrated luminosity $\mathcal{L}$ for LEP2 and the corresponding mean centre-of-mass energy $\sqrt{s}$. The uncertainty on the integrated luminosity is in the order of* 0.18% *to* 0.22%.

year	$\sqrt{s}$ (GeV)	$\mathcal{L}$ (pb^{-1})	$\Delta\sqrt{s}$
1998	188.6	176.8	10.8
1999	191.6	29.8	10.8
	195.5	84.1	11.6
	199.5	83.3	11.8
	201.8	37.2	11.9
2000	204.8	79.0	18.5
	206.5	130.8	20.5
	208.0	8.3	20.5

Chapter 3

Event selection

In this thesis the signal events are W pairs decaying into $qqqq$ (the fully hadronic events) or $qq\ell\nu$ (the semi-leptonic events). W pairs can also decay into $\ell\nu\ell\nu$ (the fully leptonic events), but since the $\ell\nu\ell\nu$ channel has very little mass information due to the two undetected neutrinos, this channel is not considered for the W mass measurement in this thesis.

To select the desired events it is important to know their typical signature in the detector. The fully hadronic decay mode has a high multiplicity, while the semi-leptonic mode is characterised by moderate multiplicity, missing energy and an energetic lepton in case of the electron and the muon channel. Events from other sources that mimic these signatures are denoted as background events.

By putting a cut on the number of clusters, N_{ASRC}, the fully leptonic mode and the non-hadronic $\gamma\gamma$ events can be rejected from the data sample.

In case of the semi-leptonic channel, the lepton will be identified first by looking at the properties of the required lepton. After excluding the reconstructed lepton all other objects in the detector are clustered into two jets by the Durham algorithm described in appendix A.

The neutrino is reconstructed using momentum conservation:

$$\vec{p_\nu} = \vec{p}_{miss} = -(\vec{p_l} + \vec{p}_{j_1} + \vec{p}_{j_2}), \tag{3.1}$$

where $\vec{p_\nu}$ is the momentum of the neutrino, $\vec{p_l}$ the momentum of the lepton and $\vec{p}_{j_1}$ and $\vec{p}_{j_2}$ the momentum of the two jets in a WW event.

A cut-based analysis is used to discriminate signal and background. The main object is to maximise both the efficiency and the purity. On the other hand maximising one of the two usually means degrading the other. Therefore, an optimum for both the purity and efficiency is searched for. The optimisation of the event selection is done by maximising the product of efficiency and purity.

As the kinematics change with higher centre-of-mass energies, the selection requirements change too. For every $\sqrt{s}$ an optimisation for the cuts is applied to maximise the product of efficiency and purity.

The main features of the selection for the particular channels will be discussed in the following sections.

3.1 Selection of the $qqe\nu$ events

Electron identification

The electron in the detector is identified by the shower profile of the deposited energy in the ECAL. The typical shower shapes of an electron and a hadron in the ECAL are shown in figure 3.1. The shower of an electron is very narrow in contrast to the hadronic shower shape which shows a wider spread over the BGO crystals. While a hadron shows a shower profile in both ECAL and HCAL, the energy of an electron is completely absorbed in the ECAL. Hence, an electron does not have a matched shower in the HCAL.

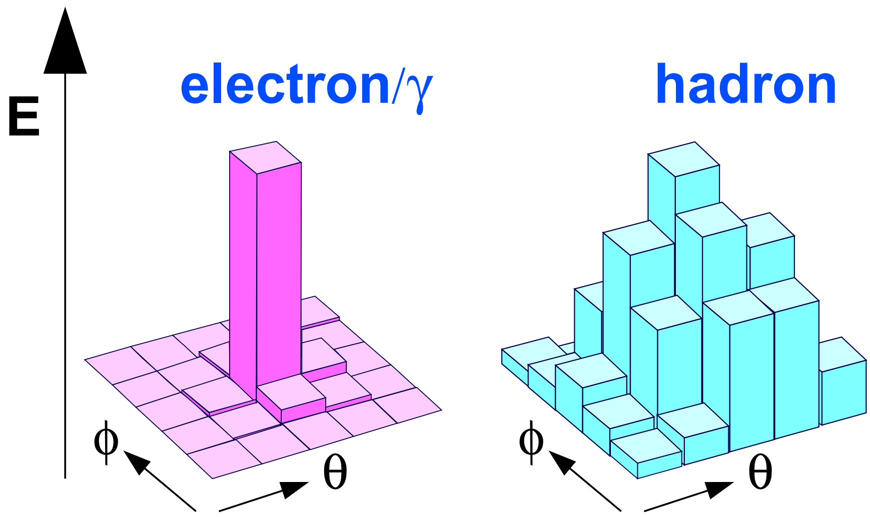

Figure 3.1: *The energy distribution in the ECAL over the crystals is much narrower for an electron (left) than for a hadron (right).*

The shower profiles of a photon and an electron are practically identical. To separate a photon from an electron, an associated TEC track matching the deposited energy in the ECAL is required.

The shower profile is studied in detail to obtain a maximum separation between a hadron and an electron. Two variables are important for the electromagnetic selection criteria. First, the variable E_9/E_{25}, which is the ratio of the energy deposit in 9 and 25 crystals surrounding the most energetic crystal. Secondly, the χ^2_{em} calculated by comparing the shower profile in a 3×3 array of crystals around the most energetic crystal with an electron shower profile obtained from test beam measurements.

The following electromagnetic selection criteria have been used:

- $E_9/E_{25} \geq 0.98$;
- $\chi^2_{em} \leq 35.0$.

The BGO bump is matched with a TEC track to dispose of possible photons. A matching track is defined as:

- $\mathrm{hits/span} > 0.5$; Span is the difference between the first and last wire hit expressed in the number of wires.

- $\mathrm{DCA} < 50$ mm; The DCA is the distance of closest approach of the reconstructed track to the event vertex.

- $p_T > 0.5$ GeV, with p_T the transverse momentum;

- $\Delta\phi \leq 20$ mrad if $|\cos\theta_e| \leq 0.90$, else $\Omega \leq 5.6$ srad. The $\Delta\phi$ cut is applied on the difference between the azimuthal angle between the track extrapolated to the ECAL and the BGO bump, where θ_e is the polar angle of the electron. And Ω is the solid angle subtended by the two jets and the electron.

After the identification of the electron, the ECAL bump and the associated TEC track are removed from the event. The remaining objects are clustered into two jets using the Durham algorithm explained in appendix A.

Selection

The main WW background comes from the $qq\tau\nu$ channel, $\mathrm{e^+e^-} \to \mathrm{WW} \to qq\tau\nu$ which, depending on the τ charge, decays as $q\bar{q}\tau^-\bar{\nu}_\tau \to q\bar{q}\mathrm{e}^-\bar{\nu}_\mathrm{e}\nu_\tau\bar{\nu}_\tau$ or $q\bar{q}\tau^+\nu_\tau \to q\bar{q}\mathrm{e}^+\nu_\mathrm{e}\bar{\nu}_\tau\nu_\tau$. The τ-lepton has a branching ratio of about 18% for the decay into a electron and two neutrinos. But the electron from the τ-decay is less energetic and the mass of the reconstructed $\mathrm{e}\nu$-system is much smaller than from the ordinary WW-decay into the $qq\mathrm{e}\nu$ channel. Hence, a cut is applied on the energy of the electron and the invariant mass $M_{\mathrm{e}\nu}$ to reject the $qq\tau\nu$ background.

A WW pair decaying into the muon channel can also fake $qq\mathrm{e}\nu$ events. An electron in a jet can have such a large angle with respect to the other objects in the jet that it is identified as an isolated electron. The electron will be removed and the muon will be clustered with the jet. To reduce this type of background, a cut on the transverse momentum of the muon with respect to the jets, $p_T(\mu, jet)$, is used. The $p_T(\mu, jet)$ of a muon coming from a jet is much smaller than the transverse momentum coming from a $qq\mu\nu$ event.

The most important non-WW background comes from the $q\bar{q}(\gamma)$ events. An electron produced in the jets can be identified as an isolated electron. Most of the radiative photons escape undetected along the beam pipe and result in large missing momenta. The distribution of the missing momenta for these events is peaked at low polar angle θ_ν. Consequently putting a cut on $|\cos\theta_\nu|$ will reduce these events. For 1999 and 2000 data the variable $\alpha_{\mathrm{ej}} \cdot |\sin\theta_\nu|$, with α_{ej} the angle between electron and nearest jet, is used to enhance the separation power. Since the electron in these background events are emanating from one of the jets, the distribution of the angle α_{ej} is also peaked at low values for $q\bar{q}(\gamma)$.

A photon from the $q\bar{q}(\gamma)$ event can convert into an $\mathrm{e^+e^-}$ pair, which can also fake the signal event. To reject these events a cut is applied on the difference in electron energy measured in the ECAL and the momentum of the associated TEC track.

The selection efficiency ranges between 78.1% and 72.8% and the purity is about 90%. The number of expected signal and background events is listed in table 3.1.

The complete set of cut values can be found in [56].

A candidate $qq\mathrm{e}\nu$ event is shown in figure 3.2.

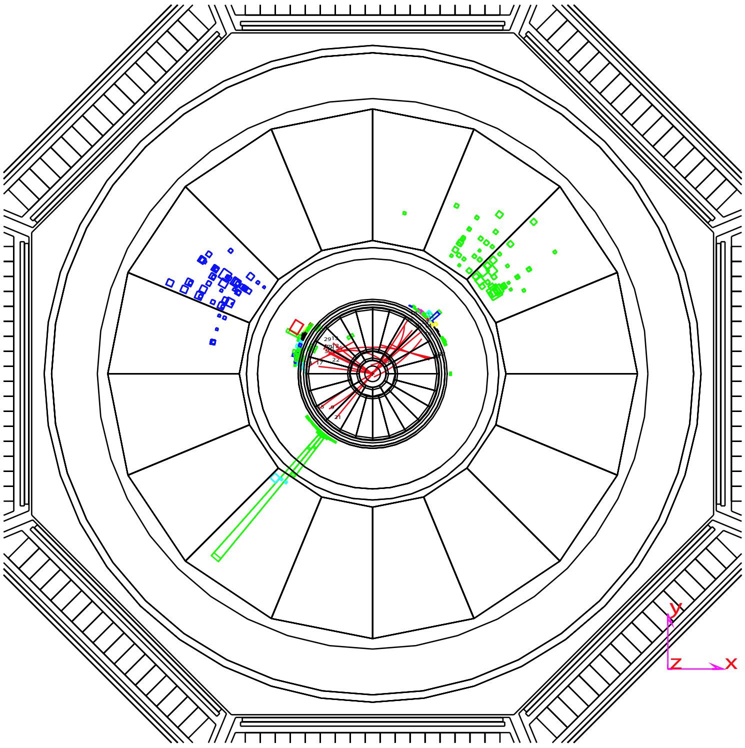

Figure 3.2: *An xy-view of a selected candidate $qqe\nu$ event at $\sqrt{s} = 196$ GeV. The main detectors, radially outward, are the TEC, ECAL, HCAL, muon filter and the inner layer of the muon chambers. The electron is represented by the large narrow bump. The clustered depositions in the HCAL represent the two jets.*

3.2 Selection of the $qq\mu\nu$ events

Muon identification

Two classes of muons have to be distinguished for the muon identification. The first type of muon, which is measured in at least two layers of muon chambers is called AMUI. The second type of muon is reconstructed by its signature of a minimum ionising particle, MIP, using information from the central tracking chamber and the electromagnetic and hadronic calorimeters. The MIP events are meant to recover events where the muon is not detected by the muon chambers.

Both muon types are reconstructed separately. A thorough description of the reconstruction of the muons can be found in [41]. The main features are given below.

- AMUI:
  - $N_{AMUI} \geq 1$, a muon reconstructed by the standard L3 routines;
  - $r\mathrm{DCA} < 100\ \mu\mathrm{m}$, $|z\mathrm{DCA}| < 500\ \mu\mathrm{m}$, where the rDCA and zDCA mean respectively the DCA in the $r\phi$-plane and in the z-direction. These requirements eliminate most cosmic muons.

- MIP:
  - $N_{MIP} \geq 1$, a MIP reconstructed by the standard L3 routines;
  - $\mathrm{DCA} \leq 2\ \mathrm{mm}$.

Selection

In the selection of the $qq\mu\nu$ channel the AMUI and MIPs are handled separately. Although most of the selection variables are the same, the cut values differ for both types of classes.

To reduce $\ell\nu\ell\nu$ background events with low multiplicity the cut $N_{ASRC} \geq 10$ is applied. The number of ASRC's in the $qq\mu\nu$ analysis is counted from all ECAL and HCAL clusters above 0.1 GeV. This cut removes all low multiplicity background.

By demanding 25 GeV $\leq M_{qq} \leq 125$ GeV and $M_{\mu\nu} \geq 53$ GeV for the AMUI and 50 GeV $\leq M_{qq} \leq 98$ GeV for the MIPs most of the hadronic $\gamma\gamma$ events are excluded.

Again $qq\tau\nu$ events form the most important background. Approximately 18% of the τ's decay into a muon plus two neutrinos. This type of events is removed by studying the muon momentum spectrum. Due to the W polarisation higher energetic muons exhibit an inclination to the forward region with respect to the W. The muons from the τ-decay are less energetic. The variable $P^* \equiv |p_\mu| - 10(\cos\theta^* + 1)(\mathrm{GeV})$, with θ^* the decay angle of the muon in the W rest frame, is introduced to get a better separation. The applied cuts for the muons are: $P^* \geq 18.5$ GeV for the AMUI, and $P^* \geq 15$ GeV for the MIP. This does not only remove the $qq\tau\nu$ channel but also takes the $q\bar{q}(\gamma)$ background into account.

As in the case of the electron a similar variable regarding the angle of the missing momentum or neutrino, θ_ν, and the angle between the muon and the closest jet, $\alpha_{\mu\mathrm{j}}$, can be defined as $\alpha_{\mu\mathrm{j}} \cdot \sin\theta_\nu$ to expunge $q\bar{q}(\gamma)$ events. For the MIPs the cut is put to be greater than $20°$ and for the AMUI to be greater than $5.5°$.

ZZ events can also mimic the signal by their decay to $q\bar{q}\mu^+\mu^-$. One of the muons may overlap with one of the jets or disappear in the beam pipe. By incorrect energy momentum measurement, a possible missing momentum is assigned.

The invariant mass of the two most energetic muons $M_{\mu\mu}$ shows a peak in the distribution of the invariant mass around the Z boson mass. A cut at $M_{\mu\mu} \leq 80$ GeV removes these events for the AMUI class of events.

There is no completely reconstructed muon for the MIP events. Therefore the velocity of the W,

$$\beta_{\mathrm{W}} = \frac{|\vec{p}_{j_1} + \vec{p}_{j_2}|}{E_{j_1} + E_{j_2}} \tag{3.2}$$

determined from the energy and momenta of the jets, is used to separate the ZZ background and signal. Because of the mass difference between the W and the Z their velocity is different for a given centre-of-mass energy. The requirement varies from $\beta_{\mathrm{W}} > 0.34$ to $\beta_{\mathrm{W}} > 0.49$ depending on the $\sqrt{s}$ from $189 - 208$ GeV.

Figure 3.3 shows an AMUI type event,while figure 3.4 is an illustration of a MIP type event.

About 85% of the muons in the selected samples are in the AMUI class. The efficiency varies from $77.7\% - 73.0\%$ while the purity ranges from $91.5\% - 90.0\%$.

The number of expected signal and background events is listed in table 3.1.

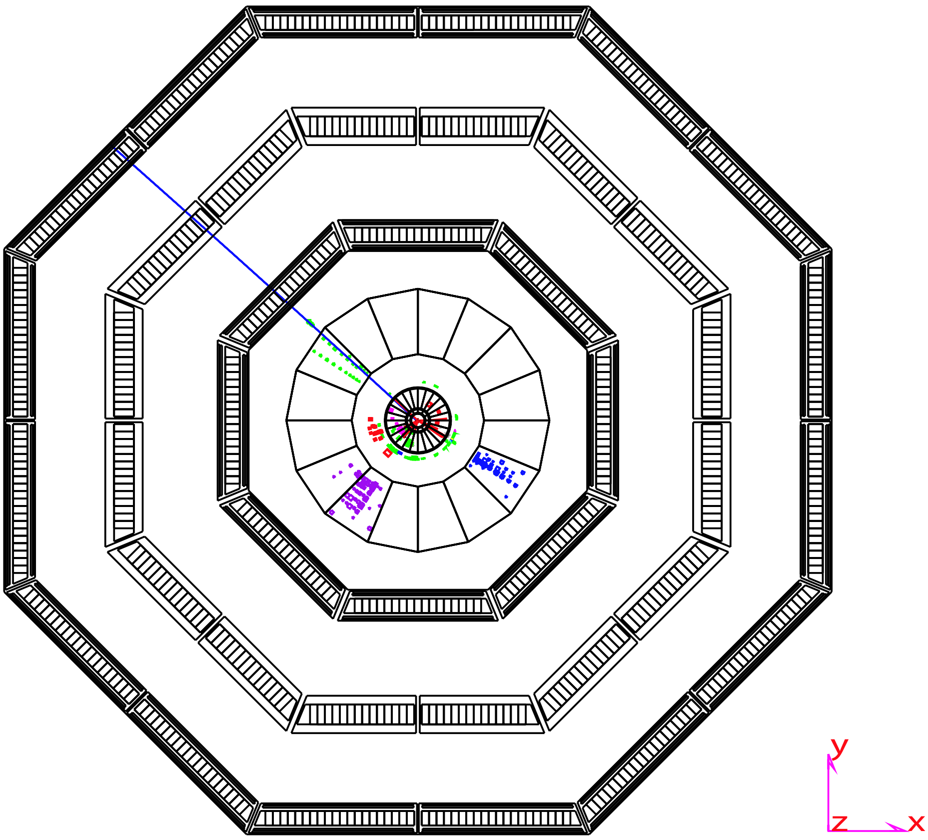

Figure 3.3: *A xy-view of a candidate $qq\mu\nu$ AMUI event at $\sqrt{s} = 200$ GeV. The three layers of the muon chambers are shown. The muon is identified by the hits in the MI, MM and MO layers.*

3.3 Selection of the $qq\tau\nu$ events

Tau identification

The τ-lepton can decay leptonically or hadronically. There are at least two neutrinos in the $qq\tau\nu$ events. In the leptonic decay of the τ another neutrino is produced. This results into reduced visible energy and missing momentum.

The electron and muon definitions are the same as described in sections 3.1 and 3.2.

If no electron or muon is found the event is analysed to look for a τ. The hadronically decaying τ-jet is identified by a neural network analysis based on the input variables:

- N_{ATRK}: the number of TEC tracks;
- N_{ASRC}: number of calorimetric clusters;
- E_{ECAL}: the energy in the ECAL;
- the half opening angle of the jet.

The jet with the highest output value of the neural network analysis is considered to be the τ-jet. The probability of misidentification is about 20%.

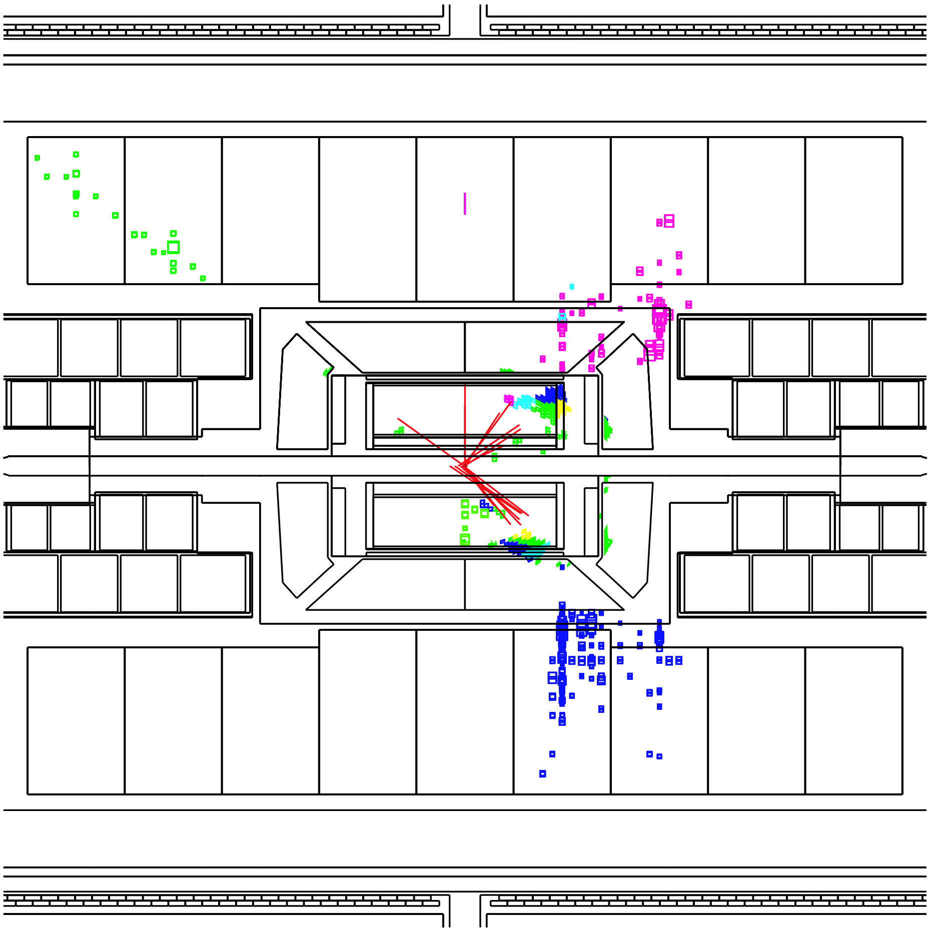

Figure 3.4: *A longitudinal view of a $qq\mu\nu$ event containing a MIP (upper left) at* $\sqrt{s} = 196$ GeV.

Selection

Pre-selection cuts dispose a part of the background events, especially $q\bar{q}(\gamma)$ and $qqqq$. The missing momentum and visible energy are strong indicators whether an event should be accepted or not. The difference between the missing momentum and visible energy has to be less than 135 GeV and the sum of the missing momentum and mass must be larger than 110 GeV. The transverse energy imbalance must be larger than 10 GeV.

The $qqqq$ background can be reduced by requiring that the solid angle between the two jets and the τ-jet has to be below 6 srad. The polar angle between the two jets should be less then 2.5 rad.

The requirement $|\cos\theta_\nu| < 0.91$ further suppresses the $q\bar{q}(\gamma)$ events in which the photon will mainly escape along the beam pipe.

The semi-leptonic WW channel $qqe\nu$, for which the electron is not identified, also needs to be rejected. A high energy deposit in the electromagnetic calorimeter and a small energy deposit in the hadronic calorimeter is an indication for these types of events. Therefore, the events where the τ-jet has more than $35\ \mathrm{GeV}$ in the electromagnetic calorimeter and less than $2\ \mathrm{GeV}$ in the hadronic calorimeter are not accepted.

Events in which the muon is not identified in the muon chamber are excluded when the τ-jet is compatible with a MIP.

A τ decaying into a lepton is shown in figure 3.5. A hadronically decaying τ is shown in figure 3.6.

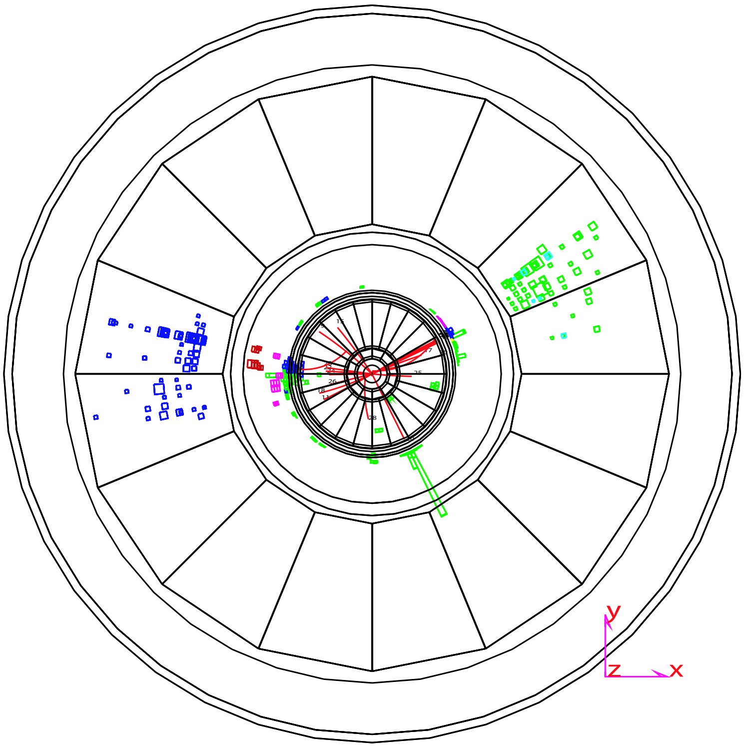

Figure 3.5: *An xy-view of a candidate $qq\tau\nu$ event at $\sqrt{s} = 196\ \mathrm{GeV}$, where the τ decays leptonically (i.e. in this case a electron).*

The selection efficiency ranges from 56.0% to 50.3%, while the purity is around 66%. The number of expected signal and background events is listed in table 3.1.

3.4 Selection of the *qqqq* events

The $qqqq$ channel is characterised by four hadronic jets. These events show a very high multiplicity. Since four jets are expected to be seen, and no lepton neutrino pair the missing energy should in addition be small. The electrons or muons produced in the jets typically will not have large energies.

The clustering into four jets is done by the Durham algorithm, see appendix A.

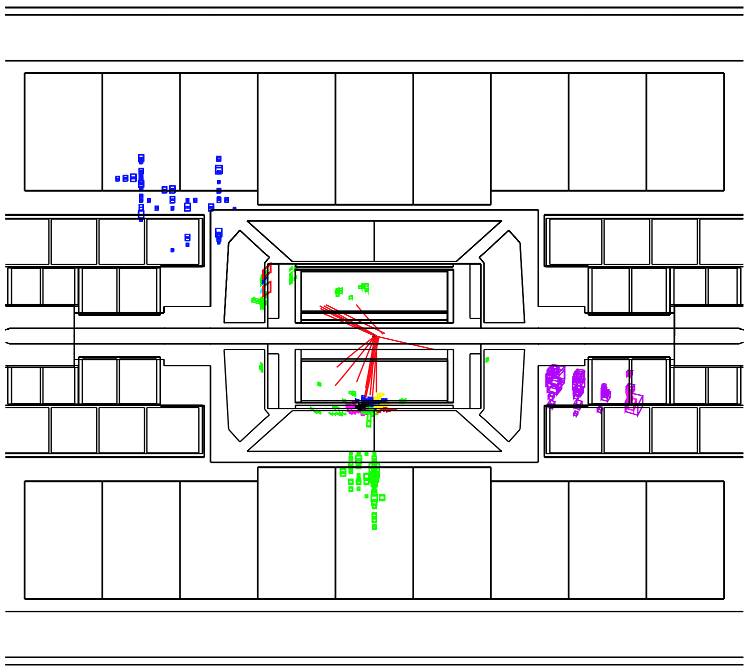

Figure 3.6: *A yz-view of a candidate $qq\tau\nu$ event at $\sqrt{s} = 200$ GeV, where the τ decays hadronically. The τ is identified in the hadron calorimeter endcaps.*

Selection

The selection of $qqqq$ events is done in two stages.

In the first stage a cut-based analysis is used to reject leptonic events and events with missing energy.

- $N_{ASRC} \geq 20$ with $E \geq 0.3$ GeV to remove events with low multiplicity;
- $E_{vis} \geq 0.75\sqrt{s}$ requires that the missing energy is small;
- $E_{\|} \leq 0.3E_{vis}$ removes events where a large amount of energy is lost in the beam pipe;
- $E_\gamma \leq 25$ GeV;
- $E_e \leq 25$ GeV, $|P_\mu| \leq 25$ GeV helps in reducing the semi-leptonic WW events;
- $y_{34} \geq 0.0015$ rejects background events with 2 and 3 jets. The definition of y_{34} is given in appendix A;
- $\frac{E_{ECAL}}{E_{ECAL}+E_{HCAL}} > 0.2$ discards events triggered due to noise in the HCAL.

The first two cuts ensure high energy and high multiplicity events, mainly disposing the $\gamma\gamma$ background. The third and fourth cuts reject $q\bar{q}(\gamma)$ events. If the photon is lost in the beam pipe there is a large longitudinal imbalance which is rejected by the third cut. If the photon is detected it is rejected by the fourth requirement.

In the second stage a neural network based analysis is used to reduce the rest of the background by training the neural network using proper input variables. The chosen variables are:

- the spherocity [57];
- track multiplicity of the jets;
- sum of the cosines of the six angles between the four reconstructed jets;
- y_{34};
- energy of the most energetic jet;
- energy of the least energetic jet;
- difference in the energies of the second and third most energetic jets;
- jet broadening [58] of the most energetic jet;
- jet broadening of the least energetic jet;
- probability of a 4C kinematic fit. (The kinematic fit will be explained in chapter 4).

These variables mainly examine whether the energy and broadening of the jets are evenly spread across jets. The large imbalance across jets in the background events arises from gluon radiation. The probability of the 4C kinematic fit is also lower due to the fake gluon jet. The signal and background neural network outputs are quite different as shown in figure 3.7, hence signal and background are rather well separated.

An event scan of a $qqqq$ candidate is shown in figure 3.8. Events are selected using a cut of 0.6 on the neural network output.

With increasing $\sqrt{s}$ the efficiency ranges from $88.1\% - 83.4\%$, while the purity changes between 79.4% and 81.6%. The number of expected signal and background events is listed in table 3.1.

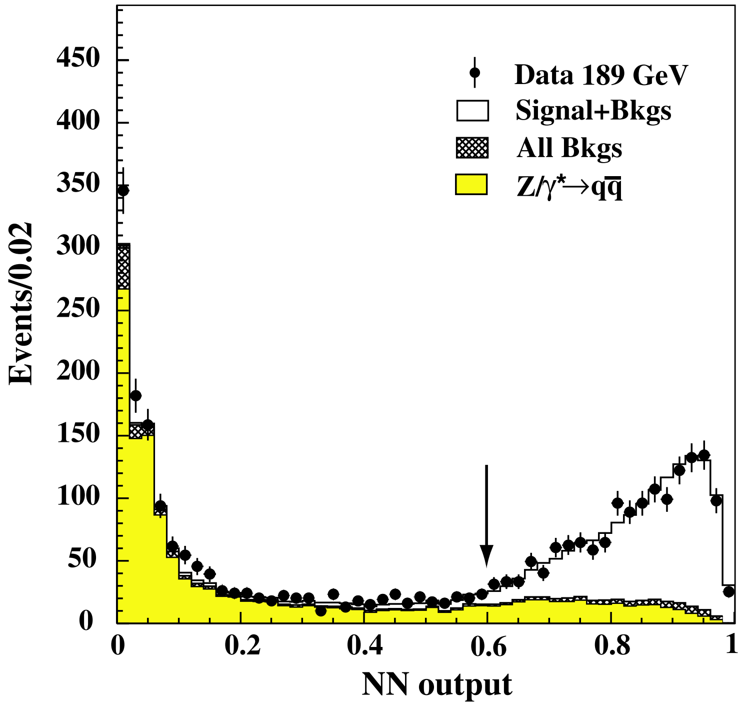

Figure 3.7: *The neural network output for the trained network using variables as described in the text. The separation between signal and background is quite well. The selection cut is placed at the value 0.6.*

Table 3.1: *Number of expected signal, 'exp', and background, 'bkg', events according to Monte Carlo simulations at different centre-of-mass energies. The total number of selected events from data is given in the column under the heading 'sel'.*

$\sqrt{s}$ [GeV]	$qqe\nu$			$qq\mu\nu$			$qq\tau\nu$			$qqqq$		
	exp	bkg	sel	exp	bkg	sel	exp	bkg	sel	exp	bkg	sel
189	329	30	347	324	35	341	238	136	436	1159	325	1477
192	56	5	73	54	6	63	41	14	61	196	51	236
196	159	15	168	159	18	157	114	64	230	562	147	665
200	155	14	152	151	17	142	110	65	190	553	137	762
202	70	7	70	69	8	79	49	18	78	247	60	301
205	146	13	176	139	15	142	102	54	168	521	128	656
207	240	22	269	236	24	240	186	86	298	858	207	1108
208	16	1	14	15	2	23	11	66	19	55	13	65

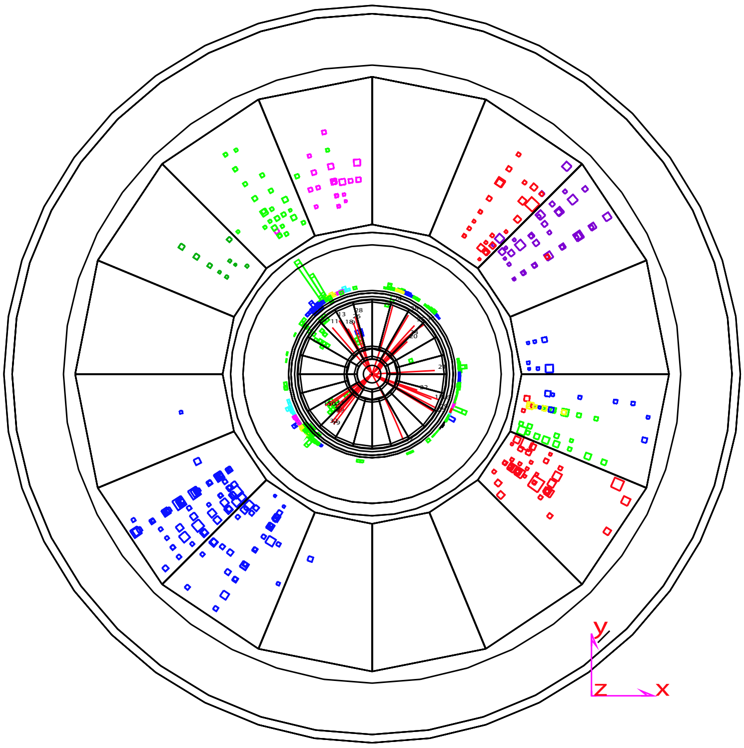

Figure 3.8: *A xy-view of a $qqqq$ event at $\sqrt{s} = 196$ GeV. In the picture the four jets can be observed.*

Chapter 4

Kinematic fit and error propagation

4.1 Kinematic fit

The energy E and the angles θ and ϕ of the jets and leptons are measured in the detector with finite resolution. In general, these quantities will not satisfy energy-momentum conservation. In the four-jet case, four-momentum conservation using the measured jets is not necessarily satisfied. In the semi-leptonic channel, $qqe\nu$ and $qq\mu\nu$, the outgoing neutrino escapes undetected. The momentum of the neutrino follows from the three-momentum conservation, but energy conservation is not automatically satisfied.

To resolve these problems and to increase the resolution, a kinematic fit is used. As a further advantage, additional constraints, such as equal mass of the decaying W's, can be imposed.

The kinematic fit is an iterative procedure, which exploits the Least-Squares Principle and the Lagrange method (following the procedure of reference [59]).

Let:

$\underline{\eta}$ Be the vector of N observables containing the energy E and the angles θ and ϕ of the detected particles.

$\underline{y}$ Be the measurements of these variables. This will be the initial guess in the iteration procedure.

$V(\underline{y})$ Be the covariance matrix, which contains the estimated errors on the measured variables and their correlation. This matrix needs not be diagonal, but in our case we simplify the problem and assume this matrix to be initially diagonal, which implies that the measurements are uncorrelated.

$\underline{\xi}$ Be the additional set of J unmeasured variables. For the semi-leptonic channel in WW production these are the energy E and the angles θ and ϕ of the undetected neutrino.

$\underline{f}(\underline{\eta}, \underline{\xi})$ Be K constraint equations, relating the measured and unmeasured variables.

In the case under study the constraint equations come from the energy and momentum conservation,

$$f_1 = \sum_{i=1}^{4} E_i = E_{CM}, \tag{4.1}$$

$$f_2 = \sum_{i=1}^{4} \beta_i E_i \sin(\theta_i) \cos(\phi_i) = 0, \tag{4.2}$$

$$f_3 = \sum_{i=1}^{4} \beta_i E_i \sin(\theta_i) \sin(\phi_i) = 0, \tag{4.3}$$

$$f_4 = \sum_{i=1}^{4} \beta_i E_i \cos(\theta_i) = 0, \tag{4.4}$$

where

$$\beta_i = \frac{\sqrt{E_i^2 - m_i^2}}{E_i}. \tag{4.5}$$

If also the equal mass condition of the two W's in the event is imposed, an additional constraint has to be added,

$$\begin{aligned} f_5 = {} & (E_1 + E_2)^2 \\ - {} & (\beta_1 E_1 \sin(\theta_1)\cos(\phi_1) + \beta_2 E_2 \sin(\theta_2)\cos(\phi_2))^2 \\ - {} & (\beta_1 E_1 \sin(\theta_1)\sin(\phi_1) + \beta_2 E_2 \sin(\theta_2)\sin(\phi_2))^2 \\ - {} & (\beta_1 E_1 \cos(\theta_1) + \beta_2 E_2 \cos(\theta_2))^2 \\ - {} & (E_3 + E_4)^2 \\ + {} & (\beta_3 E_3 \sin(\theta_3)\cos(\phi_3) + \beta_4 E_4 \sin(\theta_4)\cos(\phi_4))^2 \\ + {} & (\beta_3 E_3 \sin(\theta_3)\sin(\phi_3) + \beta_4 E_4 \sin(\theta_4)\sin(\phi_4))^2 \\ + {} & (\beta_3 E_3 \cos(\theta_3) + \beta_4 E_4 \cos(\theta_4))^2 = 0. \end{aligned} \tag{4.6}$$

The best estimate of the variables is, from the Least-Squares Principle, determined by minimising the χ^2, respecting the constraints

$$\left. \begin{aligned} \chi^2(\underline{\eta}) &= (\underline{y} - \underline{\eta})^T V^{-1}(\underline{y})(\underline{y} - \underline{\eta}) = \text{minimum} \\ \underline{f}(\underline{\eta}, \underline{\xi}) &= \underline{0} \end{aligned} \right\} . \tag{4.7}$$

Because the constraint equations are non-linear we adopt the method of the Lagrangian multipliers and use an iterative procedure solving

$$\chi^2(\underline{\eta}, \underline{\xi}, \underline{\lambda}) = (\underline{y} - \underline{\eta})^T V^{-1}(\underline{y})(\underline{y} - \underline{\eta}) + 2\underline{\lambda}\underline{f}(\underline{\eta}, \underline{\xi}) = \text{minimum}, \tag{4.8}$$

where $\underline{\lambda}$ are K Lagrangian multipliers.

If we define

$$(F_\eta)_{ki} \equiv \frac{\partial f_k}{\partial \eta_i}, \tag{4.9}$$

$$(F_\xi)_{kj} \equiv \frac{\partial f_k}{\partial \xi_j}, \tag{4.10}$$

equating the derivatives of χ^2 with respect to all unknowns to zero leads to

$$\begin{aligned} V^{-1}(\underline{\eta} - \underline{y}) + F_\eta^T \underline{\lambda} &= 0, & (4.11)\\ F_\xi^T \underline{\lambda} &= 0, & (4.12)\\ \underline{f}(\underline{\eta}, \underline{\xi}) &= \underline{0}. & (4.13) \end{aligned}$$

Assuming that the ν-th iteration is performed, the constraint equations can be expanded in a Taylor series in the point $(\underline{\eta}^\nu, \underline{\xi}^\nu)$. Neglecting the second and higher orders terms in (4.13) results in

$$\underline{f}^\nu + F_\eta^\nu(\underline{\eta}^{\nu+1} - \underline{\eta}^\nu) + F_\xi^\nu(\underline{\xi}^{\nu+1} - \underline{\xi}^\nu) = \underline{0}. \quad (4.14)$$

Together with equations (4.11) and (4.12), for the $(\nu + 1)$-th iteration and introducing

$$\begin{aligned} \underline{r} &\equiv \underline{f}^\nu + F_\eta^\nu(\underline{\eta}^{\nu+1} - \underline{\eta}^\nu), & (4.15)\\ S &\equiv F_\eta^\nu V(F_\eta^T)^\nu, & (4.16) \end{aligned}$$

we find,

$$\begin{aligned} \underline{\xi}^{\nu+1} &= \underline{\xi}^\nu - (F_\xi^T S^{-1} F_\xi) F_\xi^T S^{-1} \underline{r}, & (4.17)\\ \underline{\lambda}^{\nu+1} &= S^{-1}[\underline{r} + F_\xi(\underline{\xi}^{\nu+1} - \underline{\xi}^\nu)], & (4.18)\\ \underline{\eta}^{\nu+1} &= \underline{y} - V F_\eta^T \underline{\lambda}^{\nu+1}. & (4.19) \end{aligned}$$

The χ^2 in the $(\nu + 1)$-th step is

$$(\chi^2)^{\nu+1} = (\underline{\lambda}^{\nu+1})^T S \underline{\lambda}^{\nu+1} + 2(\underline{\lambda}^{\nu+1})^T \underline{f}^{\nu+1}. \quad (4.20)$$

The iteration stops when one of the following conditions is satisfied:

- the constraint equations are balanced to better than a required precision.
- the derivatives $\partial\chi^2/\partial\underline{\eta}$, equation (4.11), and $\partial\chi^2/\partial\underline{\xi}$, equation (4.12), are sufficiently close to 0.
- the χ^2 change per iteration step is small.

According to the number of constraints K and the number of unmeasured variables J, the fit is called a nC-fit where $n = K - J$. In case of the fully hadronic channel there are four constraints from the three-momentum and energy conservation. This fit is a $4C$-fit. Imposing equal mass constraint on the two W's changes this fit into a $5C$-fit. Similar to this, in the semi-leptonic case, without equal mass constraint, a $1C$-fit is used ($K = 4, J = 3$). Due to the undetected neutrino the momentum conservation can be fulfilled by assigning the missing three-momentum to the neutrino. However, energy conservation is not automatically satisfied. Only energy conservation remains as a constraint. In the $2C$-fit case an additional equal mass constraint is imposed for the semi-leptonic events.

4.2 Error propagation

After the iterative procedure of the kinematic fit the error on the improved variables, E, θ and ϕ, can be estimated with the law of propagation of errors. This estimation will be used in the calculation of the error on the mass.

The general principle of the law of propagation will be explained in section 4.2.1. It will be illustrated with the simple application of the mass error estimation. In section 4.2.2 the error calculation on the kinematic fit variables will be given.

4.2.1 Error on the mass

From the measured energy E and the angles θ and ϕ of the jets and leptons of an event, or in case of a neutrino taking into consideration the constraint equations in determining its E, θ and ϕ, one can calculate the mass of the hypothetical W,

$$
\begin{aligned}
M_{\mathrm{W}} = \; & [(E_1 + E_2)^2 \\
& -(p_1 \sin(\theta_1) \cos(\phi_1) + p_2 \sin(\theta_2) \cos(\phi_2))^2 \\
& -(p_1 \sin(\theta_1) \sin(\phi_1) + p_2 \sin(\theta_2) \sin(\phi_2))^2 \\
& -(p_1 \cos(\theta_1) + p_2 \cos(\theta_2))^2]^{\frac{1}{2}}.
\end{aligned}, \tag{4.21}
$$

with ${}_i = \sqrt{E_i^2 - m_i^2}$ the momentum of the lepton or jet and m_i the mass. The estimated error on this calculated mass M_{W} comes from the propagated errors of the variables, E, θ and ϕ.

The error is propagated by means of the law of propagation of errors, which takes the general form,

$$V(\underline{z}) = AV(\underline{y})A^T, \tag{4.22}$$

where $\underline{z}$ depends on the random variables $\underline{x}$,

$$z_k(\underline{x}) = z_k(y_1, y_2, \cdots, y_n), \qquad k = 1, 2, \ldots, m. \tag{4.23}$$

The matrix $V(\underline{x})$ is the covariance matrix and the matrix A is defined as,

$$\frac{\partial z_k}{\partial y_i} = A_{ki}. \tag{4.24}$$

To go from the general equation (4.22) to the special case, where we want to calculate the error on the mass, the random variable z_k is substituted by the mass M_{W} from equation (4.21). The random variables $\underline{y}$ is $(E_1, \theta_1, \phi_1, E_2, \theta_2, \phi_2)$ and the matrix A is the derivatives of M_{W} with respect to $\underline{y} = (E_1, \theta_1, \phi_1, E_2, \theta_2, \phi_2)$.

Using the improved E, θ and ϕ values found by the kinematic fit not only improves the resolution of the mass, but also the error on the mass,

4.2.2 Errors on the kinematic fit variables

To improve the resolution of a measurement and to satisfy certain physics constraints, the kinematic fit is used as discussed in section 4.1.

The errors on the variables, E, θ and ϕ are found by applying equation (4.22). If $\underline{\hat{\eta}} = \underline{\eta}^{\nu+1}$ and $\underline{\hat{\xi}} = \underline{\xi}^{\nu+1}$ then equation (4.17) - (4.19) and equation (4.15) yields [59], if all the mentioned equations are expressed in terms of $\underline{y}$,

$$\begin{aligned}\underline{\hat{\eta}} &= \underline{g}(\underline{y}) = \underline{y} - VF_\eta^T S^{-1}[I_K - F_\xi(F_\xi^T S^{-1} F_\xi)^{-1} F_\xi^T S^{-1}][\underline{f} + F_\eta(\underline{y} - \underline{\eta})], \quad (4.25)\\ \underline{\hat{\xi}} &= \underline{h}(\underline{y}) = \underline{\xi} - (F_\xi^T S^{-1} F_\xi)^{-1} F_\xi^T S^{-1}[\underline{f} + F_\eta(\underline{y} - \underline{\eta})], \quad (4.26)\end{aligned}$$

where I_K is the identity matrix.

The total covariance matrix for $\underline{\hat{\eta}}$ and $\underline{\hat{\xi}}$ from equation (4.22), is given by

$$\begin{pmatrix} V(\underline{\hat{\eta}}) & \mathrm{cov}(\underline{\hat{\eta}}, \underline{\hat{\xi}}) \\ \mathrm{cov}(\underline{\hat{\eta}}, \underline{\hat{\xi}}) & V(\underline{\hat{\xi}}) \end{pmatrix} = \begin{pmatrix} (\frac{dg}{d\underline{y}})V(\underline{y})(\frac{dg}{d\underline{y}})^T & (\frac{dg}{d\underline{y}})V(\underline{y})(\frac{dh}{d\underline{y}})^T \\ (\frac{dg}{d\underline{y}})V(\underline{y})(\frac{dh}{d\underline{y}})^T & (\frac{dh}{d\underline{y}})V(\underline{y})(\frac{dh}{d\underline{y}})^T \end{pmatrix}. \quad (4.27)$$

When we define the abbreviations,

$$\begin{aligned} G &\equiv F_\eta^T S^{-1} F_\eta, && (4.28)\\ H &\equiv F^T S^{-1} F_\xi, && (4.29)\\ U^{-1} &\equiv F_\xi^T S^{-1} F_\xi. && (4.30)\end{aligned}$$

the explicit form of the covariance matrix is,

$$\begin{aligned} V(\underline{\hat{\eta}}) &= V(\underline{y})[I_N - (G - HUH^T)V(\underline{y})], && (4.31)\\ V(\underline{\hat{\xi}}) &= U, && (4.32)\\ \mathrm{cov}(\underline{\hat{\eta}}, \underline{\hat{\xi}}) &= -V(\underline{y})HU. && (4.33)\end{aligned}$$

The fit procedure reduces the variance on the measurement and correlates the quantities even if the measurements are independent.

4.3 Example of an event fit

As a example of the kinematic fit I will show one $qqe\nu$ event at a centre-of-mass energy of $189\ \mathrm{GeV}$. Figure 4.1 shows an event in which the electron and the two jets can be clearly distinguished.

Table 4.1 gives the measured values of the energy, polar angle and azimuthal angle for the jets and electron in the selected candidate event which is shown in the event display in figure 4.1. Since the neutrino cannot be detected, it is reconstructed from the momentum conservation.

The estimated errors on these measured values, which are determined from the detector resolution as discussed in section 4.4, are shown in table 4.1. Due to the fact that the neutrino is

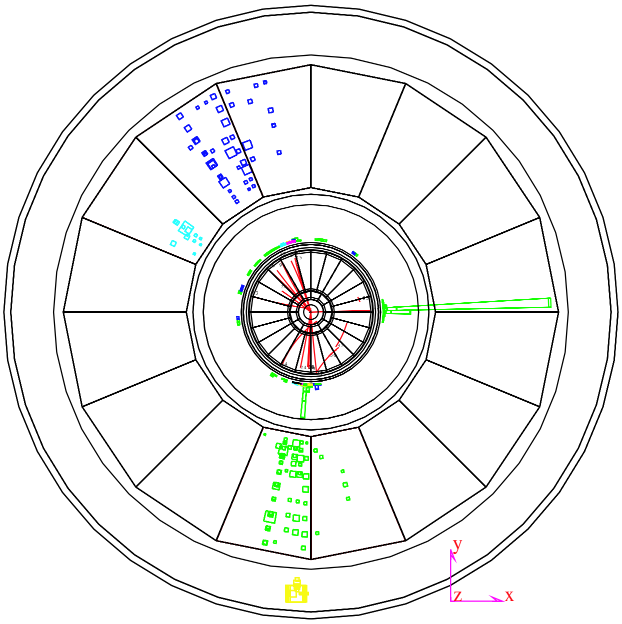

Figure 4.1: *A event display of a candidate* $qqe\nu$ *event at a centre-of-mass energy of* $189\ \mathrm{GeV}$. *The electron can be seen as a large bump on the right-hand side of the picture.*

reconstructed from the other measurements of the electron and jets it is not used in the kinematic fit which is indicated by the large values in the table.

Imposing energy-momentum conservation and equal mass of the two W bosons in the kinematic fit procedure gives the new estimation of E, θ and ϕ in table 4.2.

As discussed in section 4.2.2 the uncertainties on the kinematic fit variables can be determined from the covariance matrix in equations (4.31) and (4.32). Table 4.2 presents the results for the candidate $qqe\nu$ event.

Figure 4.2 shows, for a Monte Carlo sample at $\sqrt{s} = 196\ \mathrm{GeV}$, how the kinematic fit improves the mass resolution. The mass before and after the kinematic fit is compared with the generated mass. If the fit is not applied the difference between the generated and measured mass is much larger compared to the difference between the $2C$-fit mass and generated mass. The kinematic fit thus enhances the resolution.

4.4 Resolution

The kinematic fit requires the covariance matrix $V(\underline{y})$ as input parameter. This matrix contains the estimated errors on the measured variables and their correlations. To simplify the calculations it is assumed that the measurements are uncorrelated, i.e. the non-diagonal elements are zero.

The resolutions used in the covariance matrix for electrons, muons and jets are determined from Monte Carlo sample studies and verified with real data using $\mathrm{Z} \rightarrow f\bar{f}$.

Uncertainties on the energy and angle measurements depend on which sub-detectors are hit by the particles. Also the energy of the particle is a factor in the precision of the measurement, due to the fact that the detector is optimised for certain energy ranges. To account for these facts

Table 4.1: *The E, θ and ϕ of the two jets, the electron and the neutrino in a certain $qq\mathrm{e}\nu$ event before the kinematic fit. The parameter values of the electron neutrino are are not measured but derived from the momentum conservation. The associated errors of the measurement on E, θ and ϕ of the jets and leptons in before the kinematic fit are also given. There is no error assigned to the neutrino variables since these variables are derived from the momentum conservation.*

	q_1	q_2	e	ν_e
$E^{beforefit}$ [GeV]	57.46 ± 6.47	27.08 ± 4.56	48.56 ± 0.73	49.21
$\theta^{beforefit}$	1.837 ± 0.033	2.080 ± 0.058	1.3188 ± 0.0100	1.255
$\phi^{beforefit}$	4.640 ± 0.030	2.078 ± 0.053	0.0307 ± 0.0100	2.339

Table 4.2: *The E, θ and ϕ of the jets and electron in the candidate $qq\mathrm{e}\nu$ event and the errors on the E, θ and ϕ of jets and leptons after the kinematic fit. The errors on the variables of the neutrino are calculated by means of the law of error propagation.*

	q_1	q_2	e	ν_e
E^{2Cfit} [GeV]	60.08 ± 1.62	34.25 ± 1.64	48.39 ± 0.71	45.94 ± 0.71
θ^{2Cfit}	1.833 ± 0.033	2.061 ± 0.056	1.3182 ± 0.0099	1.155 ± 0.063
ϕ^{2Cfit}	4.632 ± 0.029	2.082 ± 0.053	0.0315 ± 0.0099	2.309 ± 0.069

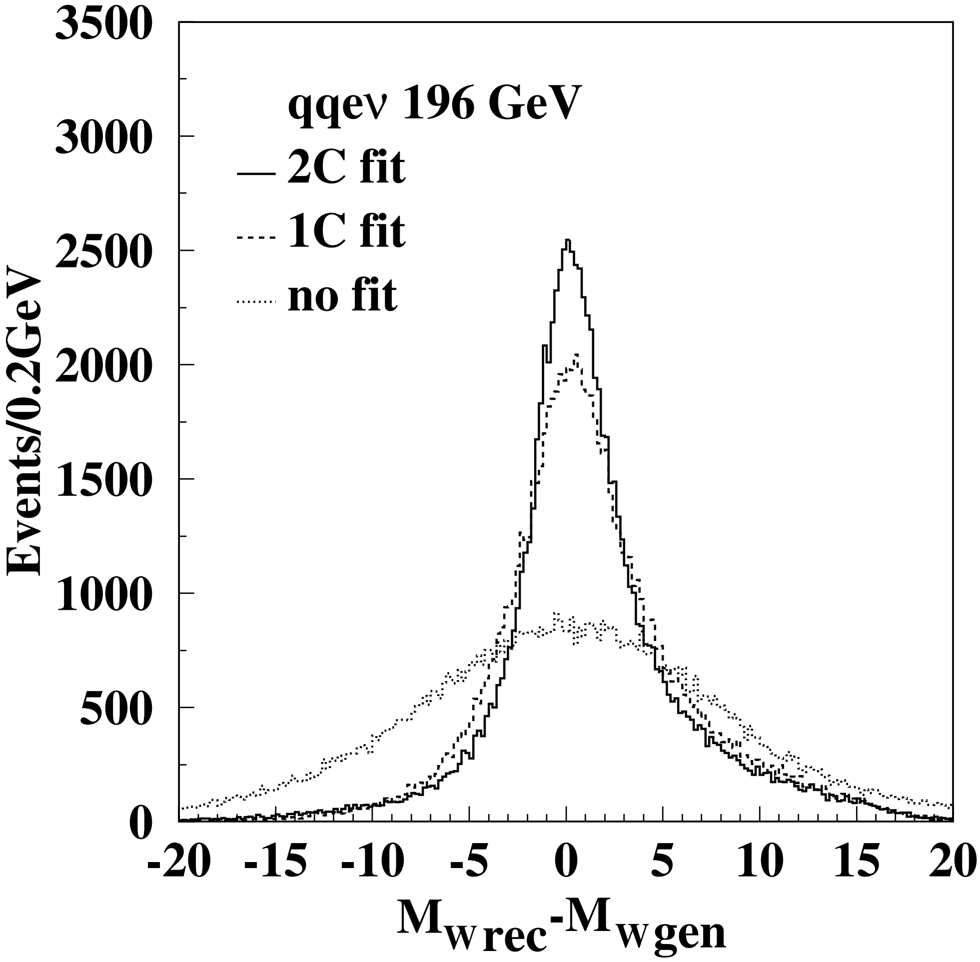

Figure 4.2: *The difference of the reconstructed mass before the kinematic fit and the generated mass shows a much broader distribution than the distribution in which the 2C fit mass is compared with the generated mass. The 1C fit also improves the resolution of the mass but less than the 2C fit. The kinematic fit clearly enhances the resolution of the mass.*

the energy, θ and ϕ resolution parametrisations are a function of E and θ. The azimuthal angle is neglected in the parametrisation, because the detector is symmetric in the ϕ direction.

4.4.1 Muon resolution

The muon energy resolution depends on the number of muon chambers that are hit and the region of the detector, i.e. barrel or forward region, as well as on the momentum of the muon itself. Muons are divided in different classes according to the number of segments reconstructed in the barrel and forward chambers. If a muon is reconstructed in all three chambers of the barrel it is denoted as '3p'. If only two barrel segments and one forward segment are reconstructed it is classified as a '2p1f'. In a similar way other types of muons are classified. Figure 4.3 [41] shows the difference between two different types of muons. The spectrum on the left-hand side is the

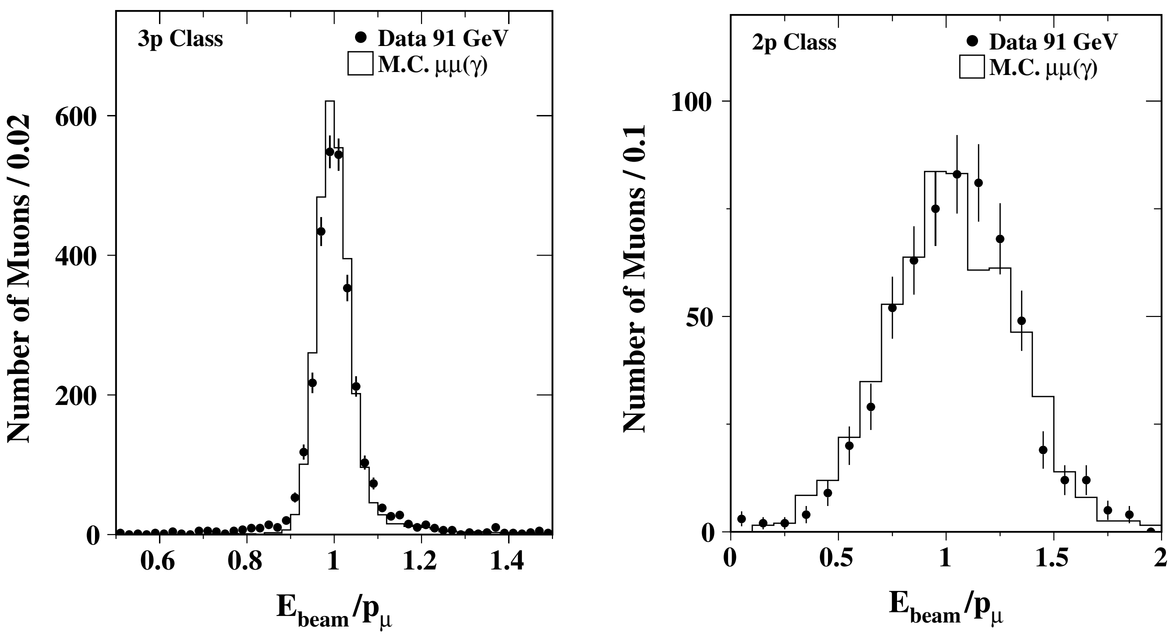

Figure 4.3: *The difference between two types of muons is shown: the resolution of the so-called 3p muons on the left-hand side is compared with the 2p muons on the right-hand side. The number of segments reconstructed in the barrel changes the resolution. The momentum resolution for the 3p class muons is* 3.4% *while for the 2p0f class it is* 27% *for data at the Z peak.*

3p muon category. The broader spectrum on the right-hand side are the events with only two segments in the barrel, 2p0f, or shortly 2p. The difference in resolution for these different types of muons can be clearly observed from these examples. For each different muon type the energy or momentum resolution is dependent on the momentum itself. The momentum dependence for a 3p class muon is shown in figure 4.4 [41]. A muon with a momentum of about 45 GeV in the 3p class has a relative resolution of 3.7% while the other muon categories are around 30% and the MIP resolution is about 40%

The polar and azimuthal angle resolutions depend on whether there is a matching TEC track or not. If there is a matching TEC track the angular measurements are much better. For θ the resolution ranges from $0.15°$ to $0.23°$, while if there is no matching track it rises to $0.46°$. If no

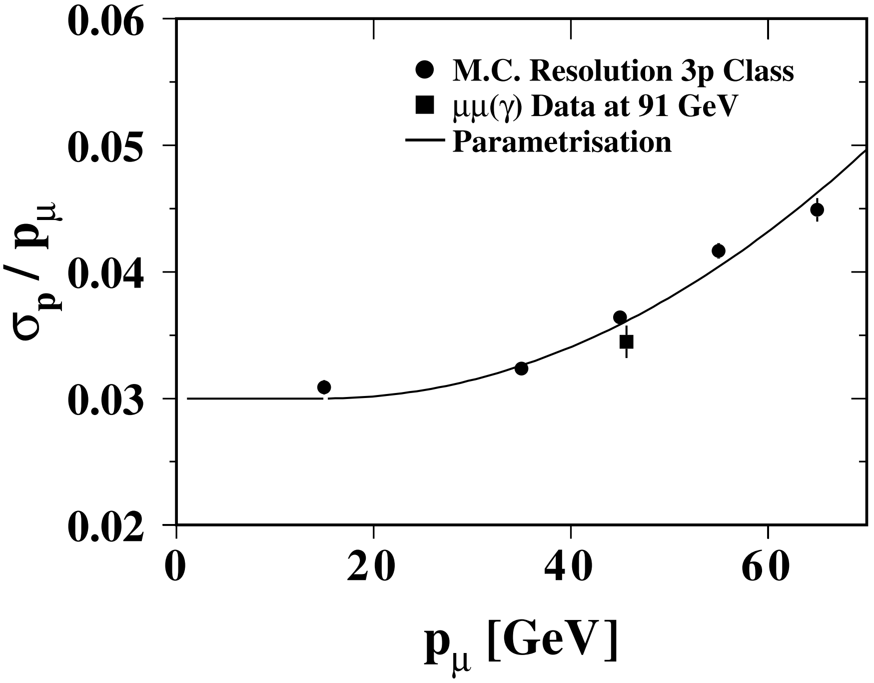

Figure 4.4: *Momentum dependence of the resolution of 3p class muons. The parametrisation is determined from Monte Carlo simulation. The square is the resolution of the Z peak data for a muon momentum of* $45\ \mathrm{GeV}$.

track is matched ϕ has an accuracy of $0.17°$ which improves to $0.01°$ with a track match.

With a Z decaying into a muon pair one can test the description of the angular resolutions. The two muons are produced practically back-to-back at the Z peak. One can extract the distributions $(\theta_1 + \theta_2 - 180°)$ and $(\phi_1 - \phi_2)$ for the two produced muons as is shown in figure 4.5 [41]. The θ resolution for a muon at $45\ \mathrm{GeV}$ is $0.26°$, whereas the ϕ resolution is about $0.021°$ for all types of measured muons conjointly. The MIP resolution is slightly worse at around $0.34°$ and $0.026°$ for θ and ϕ. A more detailed description of the Z calibration test for the muon resolution can be found in [41].

4.4.2 Electron resolution

In a similar way one may assume that the electron resolutions also depend on the direction of the electron in the detector. Moreover, if the electron has passed the EGAP it is expected to have a worse measurement. However, in the data as provided for the electron channel in this thesis the electron resolutions are fixed throughout the detector. The energy resolution has been determined to be 1.5% of the measured energy for the electron. The error on the measured polar and azimuthal angle are set to be $0.56°$. In section 4.5 it will be shown that the resolution assumptions for the electron are reasonable.

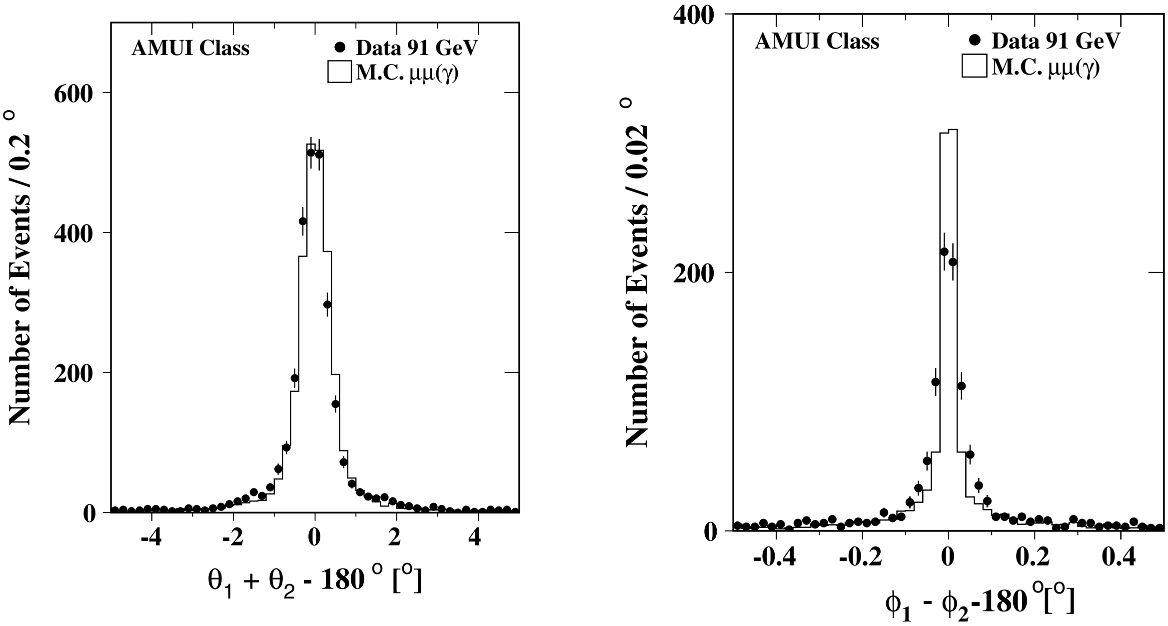

Figure 4.5: *Angular resolution for a muon. Left is the θ resolution for a* 45 GeV *muon, while the right plot shows the ϕ distribution for the same muons at Z peak.*

4.4.3 Jet resolution

The relative jet energy resolution depends on the energy itself and the polar angle of the jet. Figure 4.6 shows the parametrisation of the energy resolution function. At low polar angle and low energy of the jet the uncertainty on the measurement increases. The relative energy resolution in the central part of the detector for a jet with an energy of 45 GeV is about 14%. This is confirmed by the energy calibration of the back-to-back events $\mathrm{e}^+\mathrm{e}^- \to \mathrm{Z} \to q\bar{q}$ in figure 4.9 [41]. In the figure Monte Carlo and data for $\sqrt{s} = 91$ GeV of selected $q\bar{q}$ events are normalised to the beam energy. The relative jet energy resolution is found to be 14.6% for the data.

The polar and azimuthal resolutions are also a function of the energy and θ. Figure 4.7 shows the parametrisation for θ, while figure 4.8 indicates the ϕ resolution. The angular resolutions are affirmed by the same selected $q\bar{q}$ events at $\sqrt{s} = 91$ GeV. Here the fact is used that the jets are almost back-to-back. The left plot in figure 4.10 [41] shows an example of the polar angle resolution for data and Monte Carlo, which is $1.43°$ for data. On the right-hand side of figure 4.10 the azimuthal angular resolution is shown and its data resolution corresponds to $1.53°$.

4.5 Testing the kinematic fit

To test whether the estimated values of the parameters E, θ and ϕ are reliable or not, the χ^2 from equation (4.20) provides a measure of the goodness-of-fit. The χ^2 is converted into a chi-square probability P_{χ^2}.

The probability P_{χ^2} is uniformly distributed between 0 and 1, under the assumption that the measurements are normally distributed. Any deviation of the P_{χ^2} from a uniform distribution indicates that either the measurement or model is unsatisfactory.

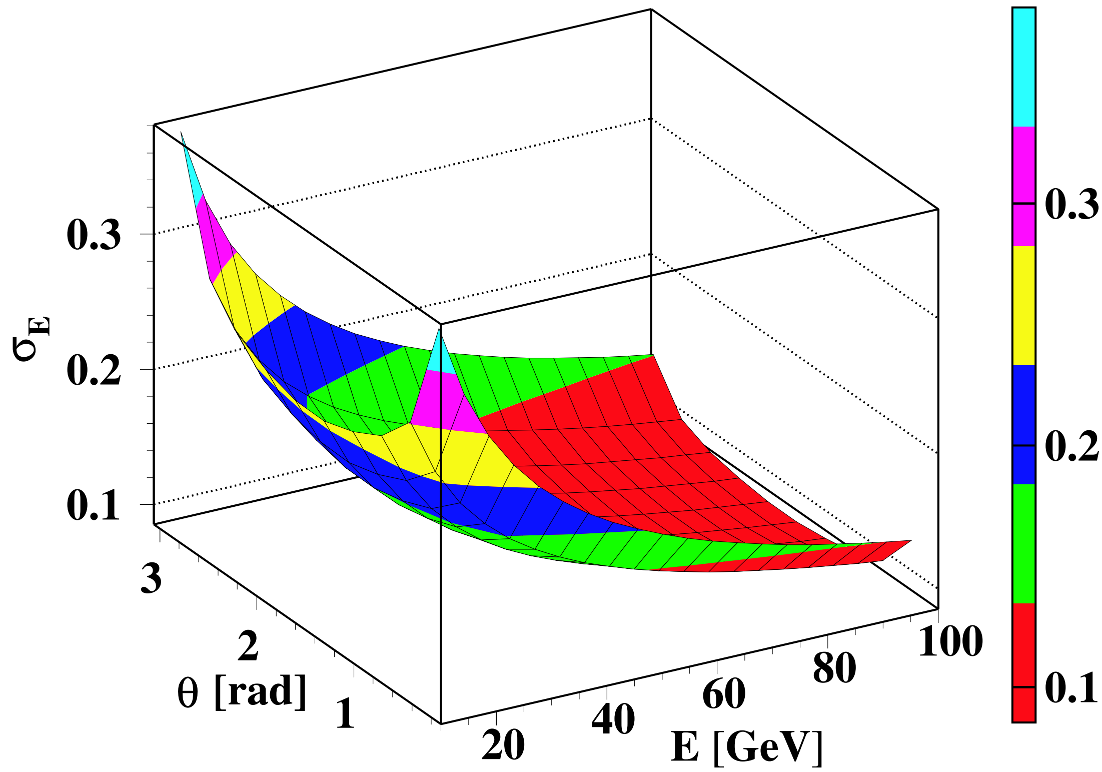

Figure 4.6: *The energy resolution for a jet is a function of energy E and polar angle θ.*

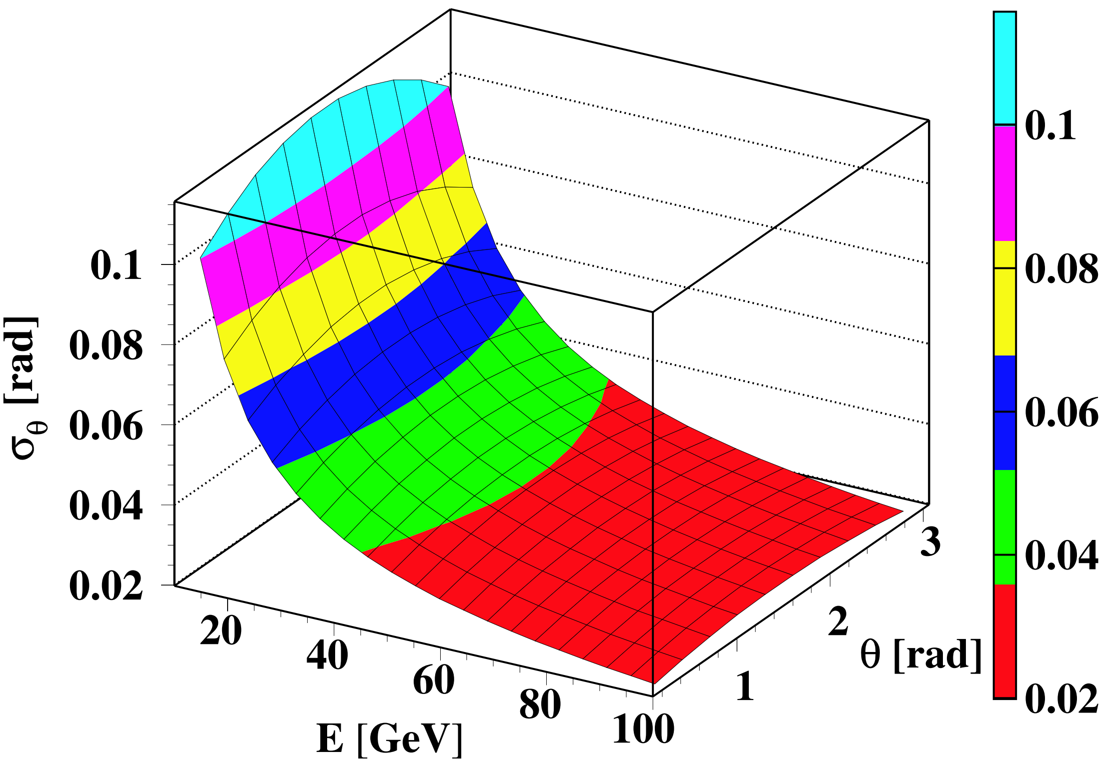

Figure 4.7: *The polar angle resolution of a jet.*

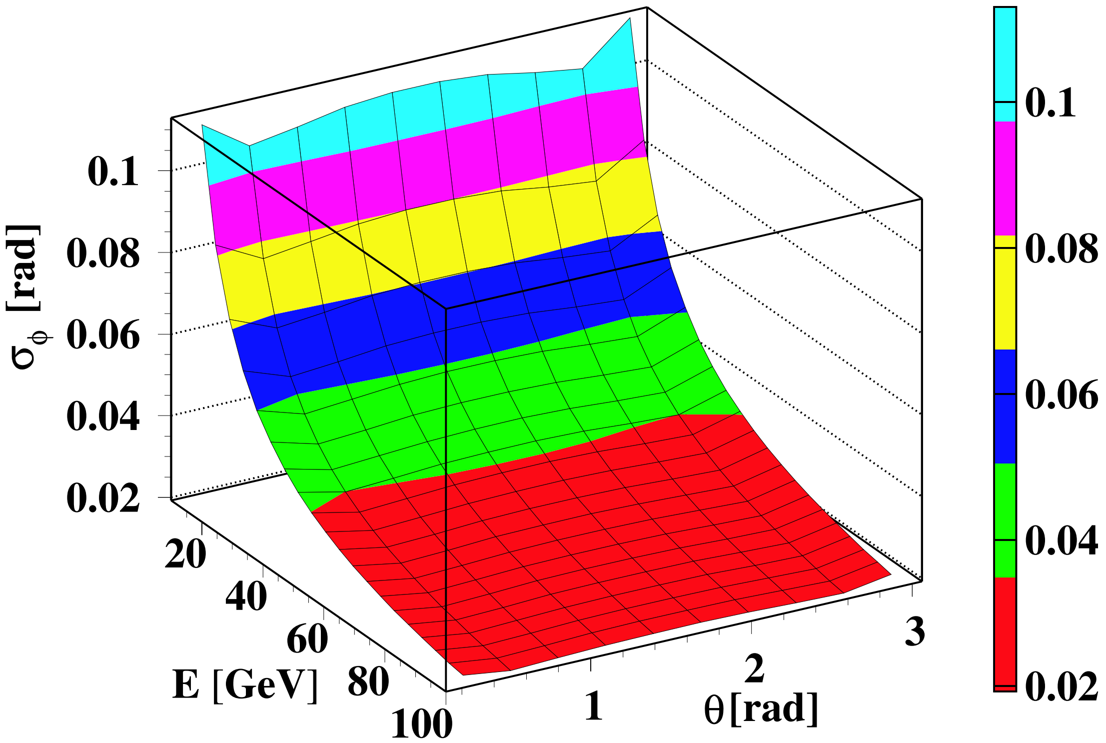

Figure 4.8: *The azimuthal angle resolution of a jet.*

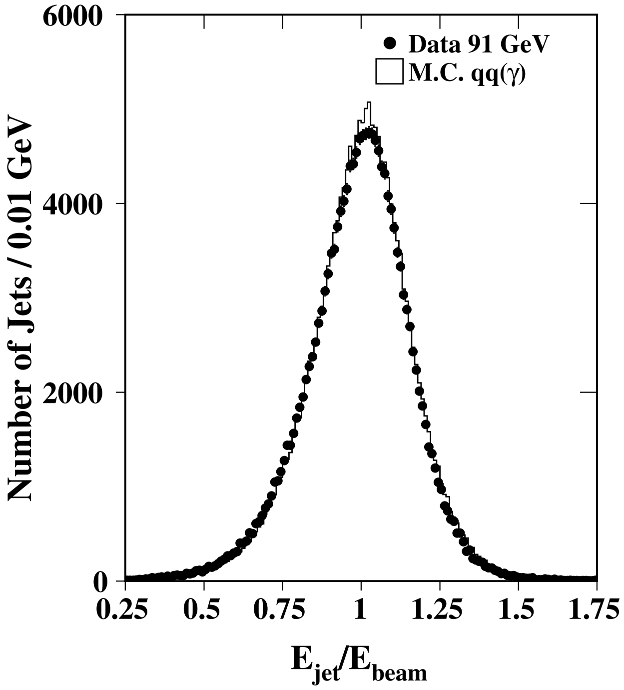

Figure 4.9: *Left: Monte Carlo and data jet energy spectrum normalised to the beam energy at* $\sqrt{s} = 91$ GeV. *The relative energy jet energy resolution is* 14.6% *for* 45 GeV *jets.*

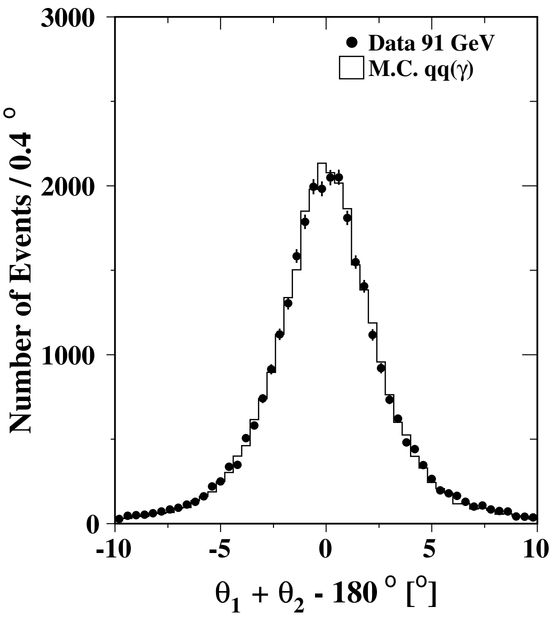

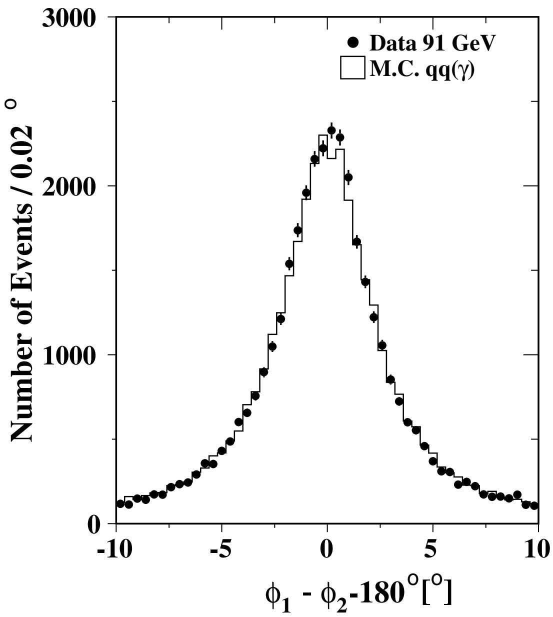

Figure 4.10: *Left: The polar angle resolution for jets measured at the Z peak. Right: The azimuthal resolution for* 45 GeV *jets.*

The probability distributions of the electron, muon and four-jet channels in figure 4.11 have a flat distribution. However, they exhibit a peak at low probability. Background events which in general do not satisfy the hypothesis of a signal event have a low probability and are revealed as contamination in this peak. But also events with bad reconstructed jets for which the kinematic fit could not properly converge can be found here. Also the measured jet momentum distribution has non-Gaussian tails. These tails can distort the chi-square probability distribution.

Aside from the peak at low probability the P_{χ^2} distribution shows a uniform distribution.

To study the fit more attentively, one can measure the deviations between the observed and fitted values with respect to the uncertainty on observed and fitted quantities. The pull of a kinematic fit for the i^{th} observation of a variable v is defined as:

$$pull(v) = \frac{v_i^{meas} - v_i^{fit}}{\sqrt{(\sigma_i^{meas})^2 - (\sigma_i^{fit})^2}}. \tag{4.34}$$

The parameters v_i^{meas} and v_i^{fit} are the measured and fitted values of v, while σ_i^{meas} is the resolution of the measured variable and σ_i^{fit} the error on the fitted value.

The pull of each variable should be a normal distribution with mean zero and standard deviation one if the measurements are normally distributed. A relative shift from zero indicates a bias in the observation. Similarly, a narrower or broader pull distribution indicates that the errors on the measurements are probably taken too large or too small respectively. Thus by examining the pull distribution it is possible to check whether the input resolutions used in the kinematic fit are reasonable.

The pull distribution for the energy, polar and azimuthal angle for the electron, muon and hadronic jet are shown in figures 4.12, 4.13 and 4.14 respectively. If the resolution functions are non-Gaussian the estimated error on the fit value σ_i^{fit} may be larger than the input resolution σ_i^{meas}. The events are put in the last bin of the plots if this happens. A good agreement between data and Monte Carlo can be seen in the examples, indicating no major error in the modelling and resolutions.

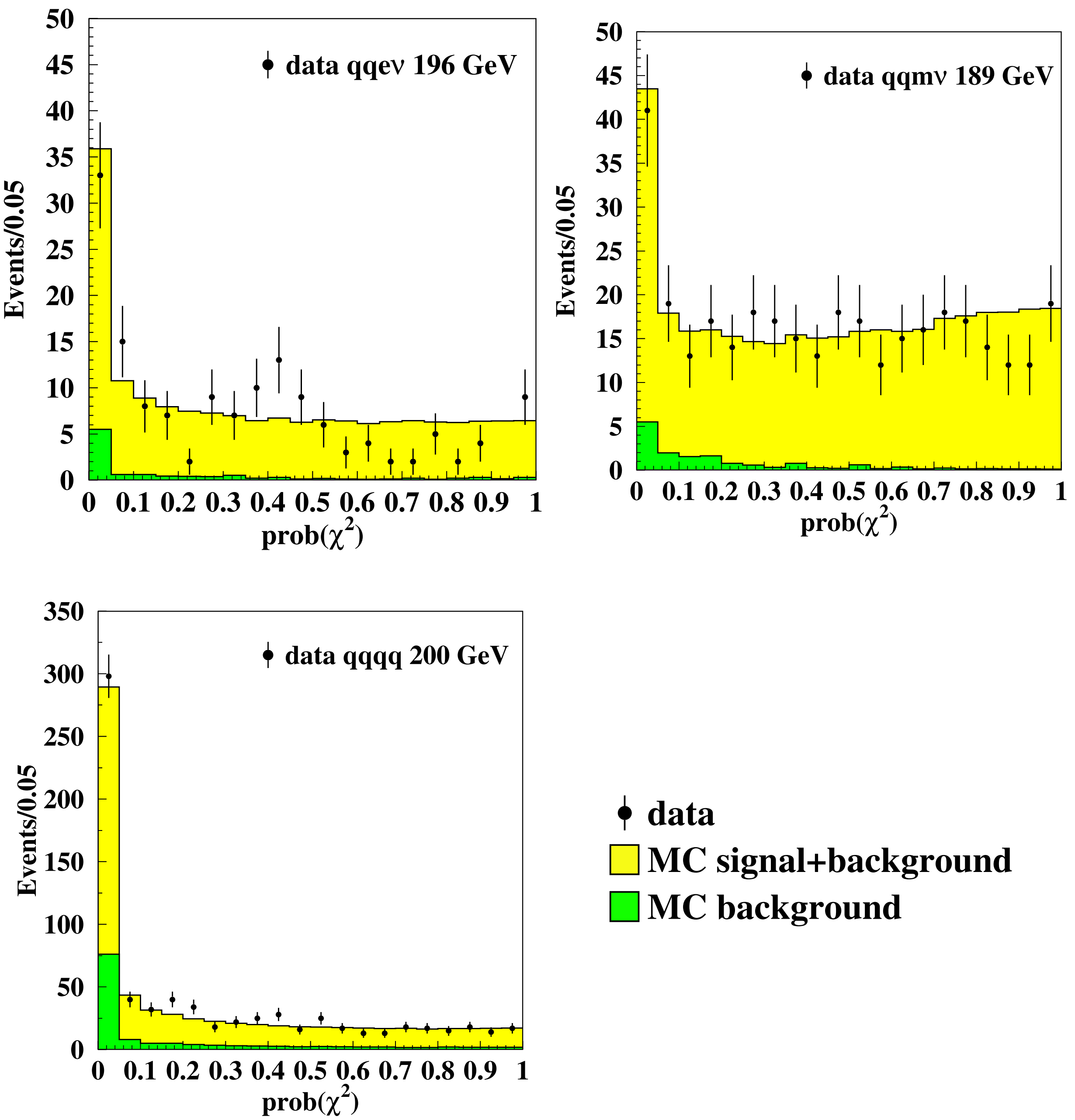

Figure 4.11: *The chi-square probability for electron, muon and four-jet channel are shown. The practically flat distributions indicate that the measurements are approximately normally distributed and that the kinematic fit model is well described.*

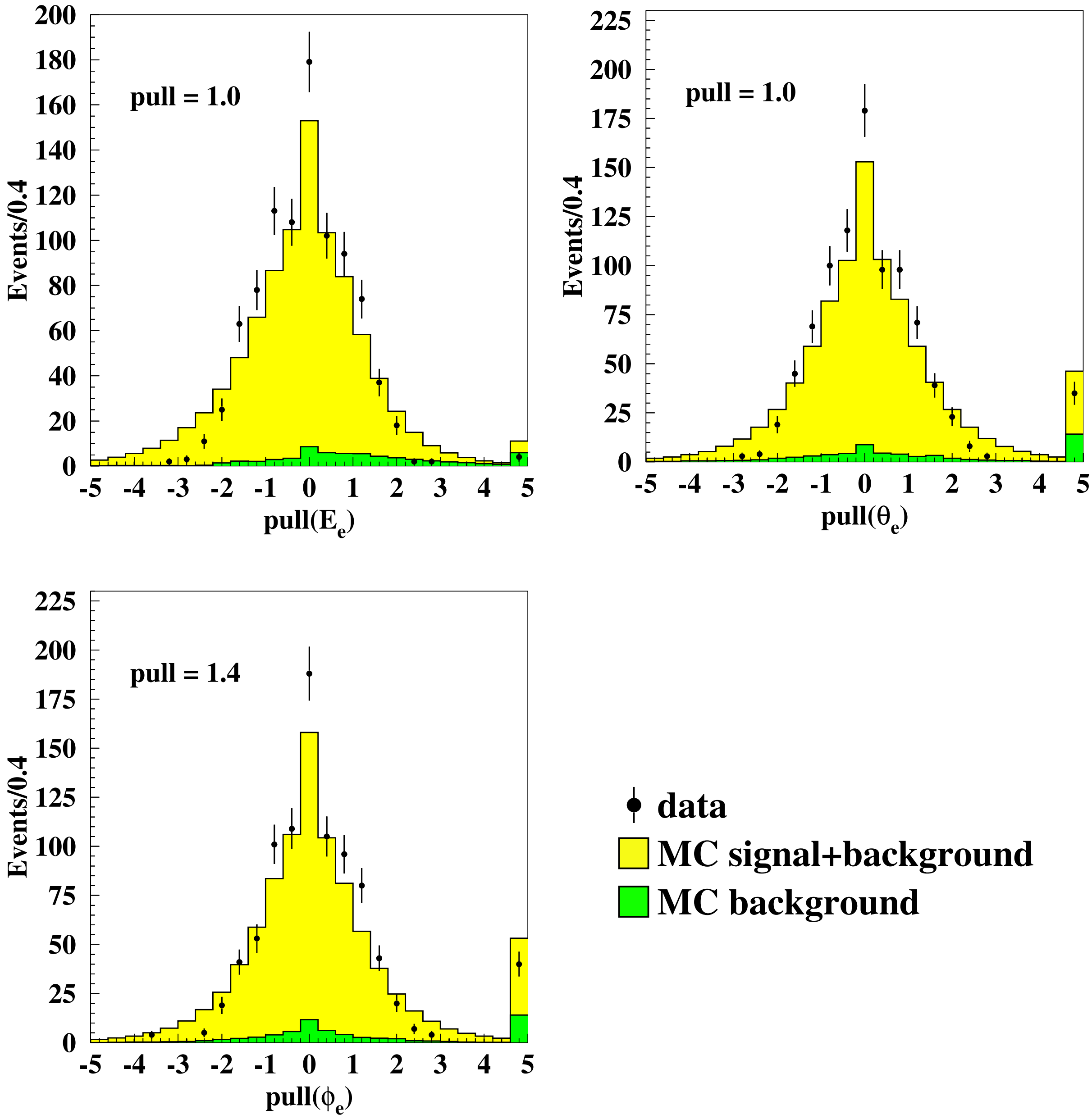

Figure 4.12: *The energy, θ and ϕ pull distributions for the electron. The last bin represents the events for which the estimated error after the fit is larger than the estimated error of the input variable. The pull is determined from a Gaussian fit through the data points.*

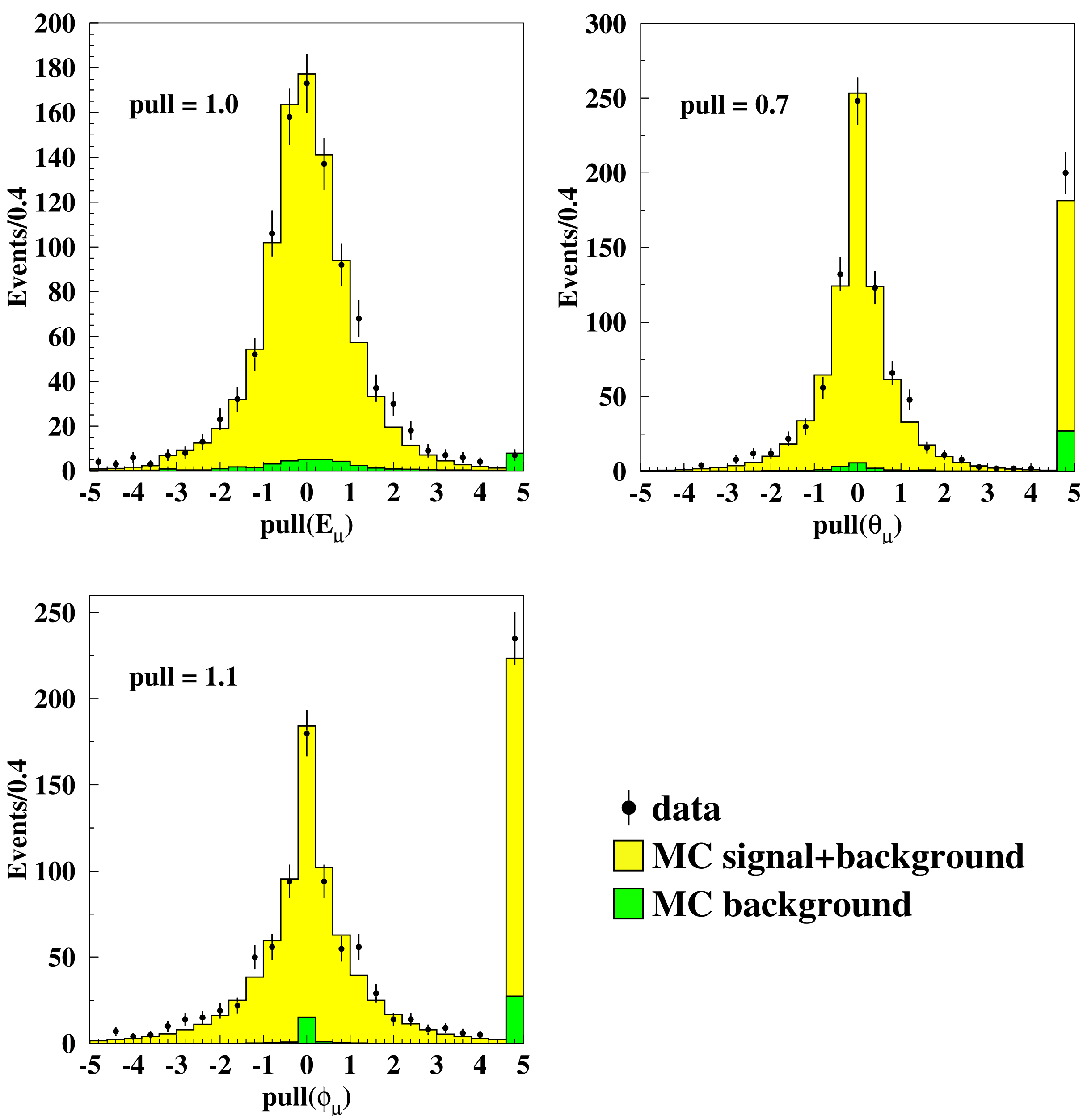

Figure 4.13: *The energy, θ and ϕ pull distribution for a muon. The last bin represents the events for which the estimated error after the fit is larger than the estimated error of the input variable. The pull is determined from a Gaussian fit through the data points.*

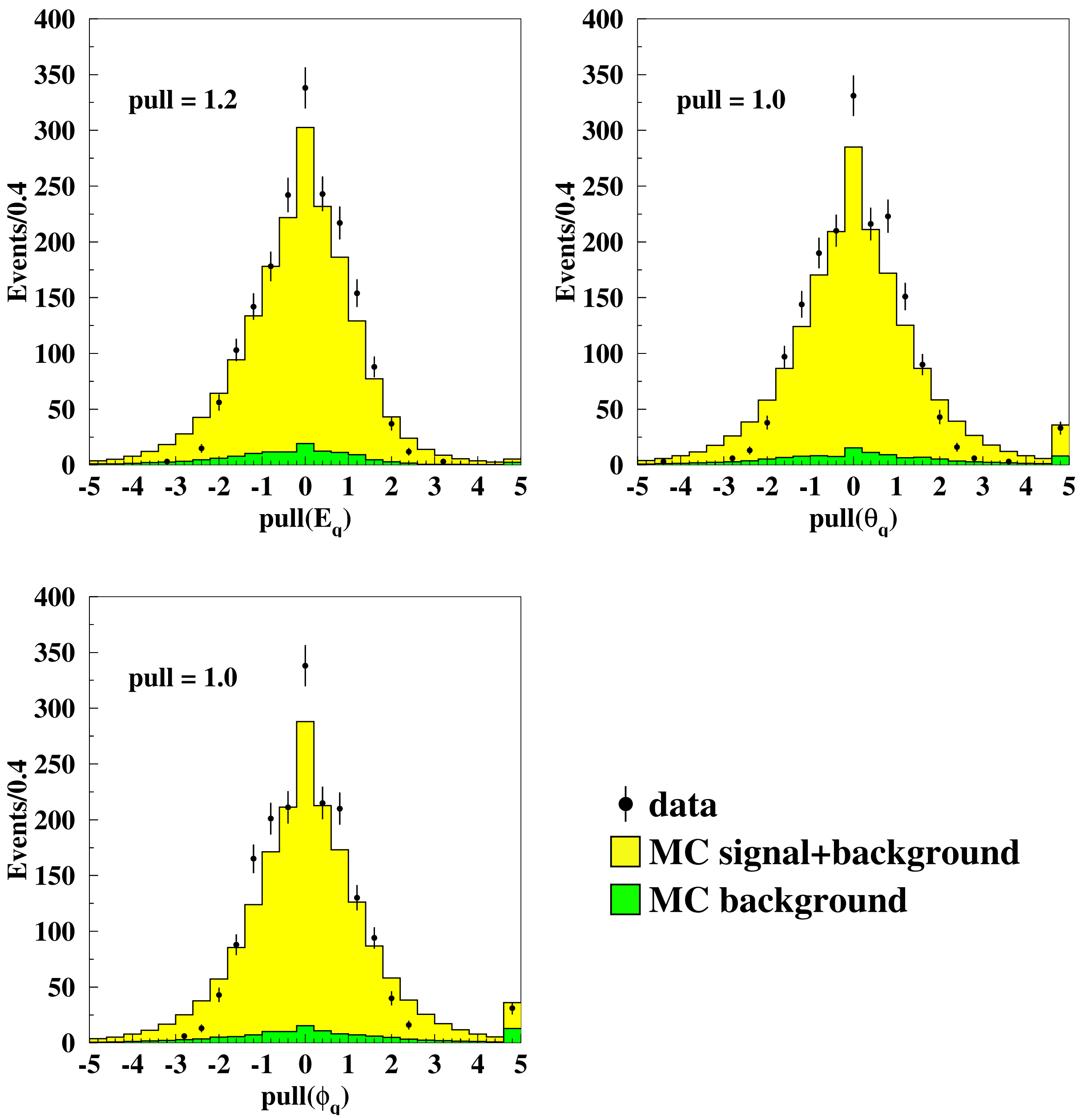

Figure 4.14: *The energy, θ and ϕ pull distribution for a jet. The last bin represents the events for which the estimated error after the fit is larger than the estimated error of the input variable. The pull is determined from a Gaussian fit through the data points.*

Chapter 5

W mass and width measurement

In this chapter the determinations of M_{W} and Γ_{W} are discussed. The mass M_{W} and width Γ_{W} are extracted from the distribution of the reconstructed invariant masses of the selected events. This is called the direct reconstruction method. The parameters M_{W} and Γ_{W} are estimated with a maximum likelihood fit.

The fitting procedure is applied for the semi-leptonic and the fully hadronic channels for the years 1998,1999 and 2000 at the different centre-of-mass energies. Finally, the sources of systematics are determined and the combination of the measurements is presented.

5.1 Likelihood function

In the direct reconstruction method the mass M_{W} and width Γ_{W} are determined with a maximum likelihood fit method. This parameter estimation method uses the invariant mass distribution after the kinematic fit with the equal mass constraint.

The probability of getting a measurement M_{inv} within a small interval $[M_{\mathrm{inv}}, M_{\mathrm{inv}} + dM_{\mathrm{inv}}]$ is given by the probability density

$$dP = \omega dM_{\mathrm{inv}}, \tag{5.1}$$

with

$$\omega(M_{\mathrm{inv}}, M_{\mathrm{W}}, \Gamma_{\mathrm{W}}) = \frac{1}{f \cdot \sigma_{\mathrm{WW}}^{acc}(M_{\mathrm{W}}, \Gamma_{\mathrm{W}}) + \sigma_{\mathrm{bg}}^{acc}} \tag{5.2}$$

$$\times \left\{ f \cdot \frac{d\sigma_{\mathrm{WW}}^{acc}}{dM_{\mathrm{inv}}}(M_{\mathrm{inv}}, M_{\mathrm{W}}, \Gamma_{\mathrm{W}}) + \frac{d\sigma_{\mathrm{bg}}^{acc}}{dM_{\mathrm{inv}}}(M_{\mathrm{inv}}) \right\}. \tag{5.3}$$

The parameter $\omega(M_{\mathrm{inv}}, M_{\mathrm{W}}, \Gamma_{\mathrm{W}})$ is the normalised differential cross-section $d\sigma/d\Omega$ at the measured invariant mass M_{inv} in the presence of background. The accepted signal W-pair production differential cross-section is denoted by $\frac{d\sigma_{\mathrm{WW}}^{acc}}{dM_{\mathrm{inv}}}(M_{\mathrm{inv}}, M_{\mathrm{W}}, \Gamma_{\mathrm{W}})$, while $\frac{d\sigma_{\mathrm{bg}}^{acc}}{dM_{\mathrm{inv}}}(M_{\mathrm{inv}})$ is the accepted background differential cross-section. The factor $(\frac{1}{f \cdot \sigma_{\mathrm{WW}}^{acc}(M_{\mathrm{W}}, \Gamma_{\mathrm{W}}) + \sigma_{\mathrm{bg}}^{acc}})$ in equation 5.3, normalises the probability distribution which is essential for the maximum likelihood method. $\sigma_{\mathrm{WW}}^{acc}(M_{\mathrm{W}}, \Gamma_{\mathrm{W}})$ and $\sigma_{\mathrm{bg}}^{acc}$ are the total accepted cross-sections of signal and background. The factor f satisfies

$$f \cdot \sigma_{\mathrm{WW}}^{acc}(M_{\mathrm{W}}, \Gamma_{\mathrm{W}}) + \sigma_{\mathrm{bg}}^{acc} = \frac{N_{data}}{\mathcal{L}}. \tag{5.4}$$

Hence f normalises the cross-section to the measured W-pair cross-section. The fluctuations in the number of data are assigned to the WW signal.

The likelihood of getting a certain set of measurements M_{inv}, $i = 1, N_{data}$, i.e. the likelihood of an observed mass distribution in the data is the product of the individual event probabilities $\omega(M^i_{\mathrm{inv}}, M_{\mathrm{W}}, \Gamma_{\mathrm{W}})$ for each selected event i,

$$L(M_{\mathrm{W}}, \Gamma_{\mathrm{W}}) = \prod_{i=1}^{N_{data}} \omega(M^i_{\mathrm{inv}}, M_{\mathrm{W}}, \Gamma_{\mathrm{W}}). \tag{5.5}$$

The likelihood in equation (5.5) should be maximised in order to determine the mass.

In practice, it is convenient to consider the negative logarithm of the likelihood function

$$-\log(L) = -\sum_{i=1}^{N_{data}} \log\omega(M^i_{\mathrm{inv}}, M_{\mathrm{W}}, \Gamma_{\mathrm{W}}). \tag{5.6}$$

The product of the individual probabilities is transformed into the sum of their logarithms which is numerically more stable. Because of the fact that the MINUIT [60] package is used, which is optimised for minimising functions, the log-likelihood is multiplied by -1. As a consequence equation (5.6) should be minimised.

In a one-parameter fit only the W boson mass M_{W} is extracted. In the one-parameter fit the M_{W} is treated as a free parameter while Γ_{W} is fixed to the Standard Model relation

$$\Gamma_{\mathrm{W}} = \frac{3G_F M^3_{\mathrm{W}}}{2\sqrt{2}\pi}(1 + \frac{2\alpha_s(M^2_{\mathrm{W}})}{3\pi}) \tag{5.7}$$

In the two-parameter fit the mass as well as the width of the W boson are simultaneously determined. Both the width and mass, Γ_{W} and M_{W}, are treated as free and independent parameters in the two-parameter fit.

5.2 Box method

The likelihood cannot be calculated analytically due to the selection criteria and smearing effects, which should be taken into account. Therefore a Monte Carlo method [61] is used to calculate the cross-section and differential cross-sections in the log-likelihood function (5.6). In this method the events from a Monte Carlo simulation are used to calculate the cross-sections. Since the Monte Carlo simulation includes as an integral part the acceptance and smearing, these effects are automatically taken into account in the calculations.

For the calculation of the cross section and differential cross section the so-called box method is used.

The differential cross-section can be calculated from the number of Monte Carlo events N^i_{box} in an interval around a data point corresponding with a mass measurement M^i_{inv}. This method may also be used in a multi-dimensional space where in general the interval is called a box. If the size of the chosen interval is V^i_{box}, the differential cross-section is approximated by

$$\frac{d\sigma^{acc}}{dM_{\mathrm{inv}}}(M^i_{\mathrm{inv}}) \approx \frac{\Delta\sigma^{acc}}{\Delta M_{\mathrm{inv}}}(M^i_{\mathrm{inv}}) = \frac{1}{\mathcal{L}_{MC}} \cdot \frac{1}{V^i_{box}} \sum_{j=1}^{N^i_{box}} 1. \tag{5.8}$$

The Monte Carlo luminosity is determined from the total number of Monte Carlo events and the total process cross-section without cuts:

$$\mathcal{L}_{MC} = \frac{N_{MC}}{\sigma^{\mathrm{tot}}}. \tag{5.9}$$

Only in the limit where the number of events in the box is infinite and the size of the box is infinitely small in equation (5.8), the exact value is obtained. Figure 5.1 shows the principle of the box method.

The box size is chosen to be as small as possible to approximate the exact value while the number of events in the box (box occupancy) has to be large enough to reduce the statistical error of the calculation in the box. Earlier studies [41] have shown that an optimal performance is reached if the box size is 0.5 GeV. A supplementary constraint on the maximum number of Monte Carlo events per box of 1000, fulfils the requirement of even smaller box sizes than 0.5 GeV, while keeping sufficient events in the box. Another constraint on the minimum number of events per box of 100 prevents the increase of the statistical error for certain data points.

The results of these conditions are graphically represented in figure 5.2. The number of events in a box is between 100 and 1000. In the region where the distribution M_{inv} is close to its maximum the maximal box occupancy of 1000 events is reached while the box volume decreases to about 0.1 GeV. The differential cross-section, which is the ratio between the box occupancy and the box volume normalised to $\mathcal{L}_{MC}$, has its peak in this region. Going away from this region the box volume increases, whereas the number of events per box remains 1000, until the size of the box is 0.5 GeV. At this point the box size remains constant at 0.5 GeV and the box occupancy decreases from 1000 to 100 events. At the tails the Monte Carlo events are less dense occupied. The box volume must increase very rapidly to fulfil the requirement of a minimum of 100 events.

The Monte Carlo prediction for the cross-section is given by:

$$\sigma_{\mathrm{WW}}^{acc} = \frac{1}{\mathcal{L}_{MC}} \sum_{j=1}^{N_{acc}^{MC}} 1, \tag{5.10}$$

where N_{acc}^{MC} is the total number of selected Monte Carlo events.

5.3 Monte Carlo re-weighting method

The cross-section and differential cross-section as determined by equations (5.10) and (5.8) are only given for the Monte Carlo generated mass M_{W} and width Γ_{W}. To compare the reconstructed mass spectrum of the data with the Monte Carlo mass spectrum, other Monte Carlo simulations with different generated M_{W} and Γ_{W} are necessary to find the parameters which minimise the log-likelihood. In principle, an infinite set of Monte Carlo samples is needed with all possible values for M_{W} and Γ_{W}. Creating several samples with a sufficient number of events would not be feasible due to the large amount of computing time. A solution which circumvents the creation of several Monte Carlo event samples, thus reducing the amount of computing time, is the re-weighting method.

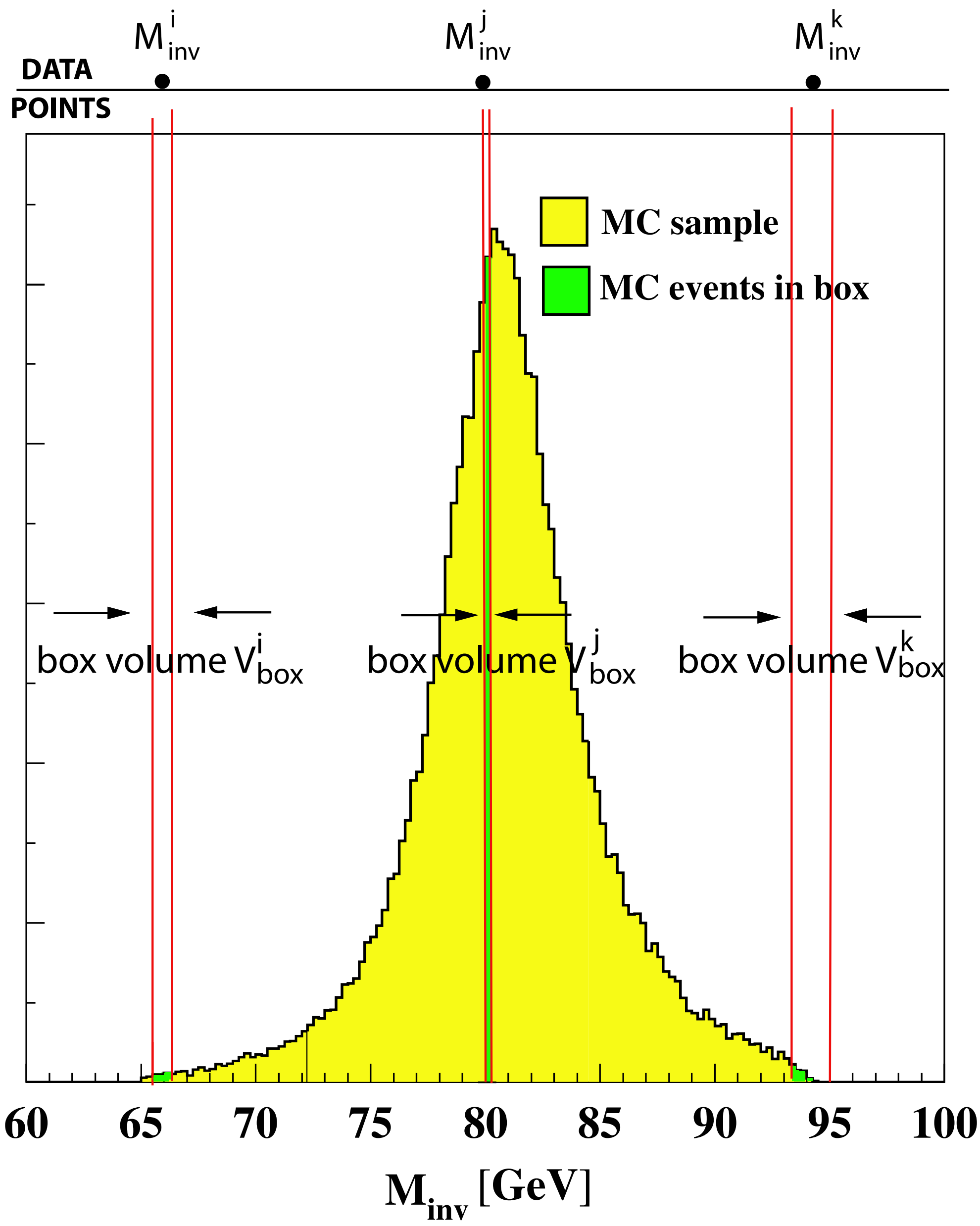

Figure 5.1: *For every data point i with invariant mass M^i_{inv} an interval is chosen, the box volume V^i_{box}. From the number of Monte Carlo events in this interval the differential cross-section can be approximated.*

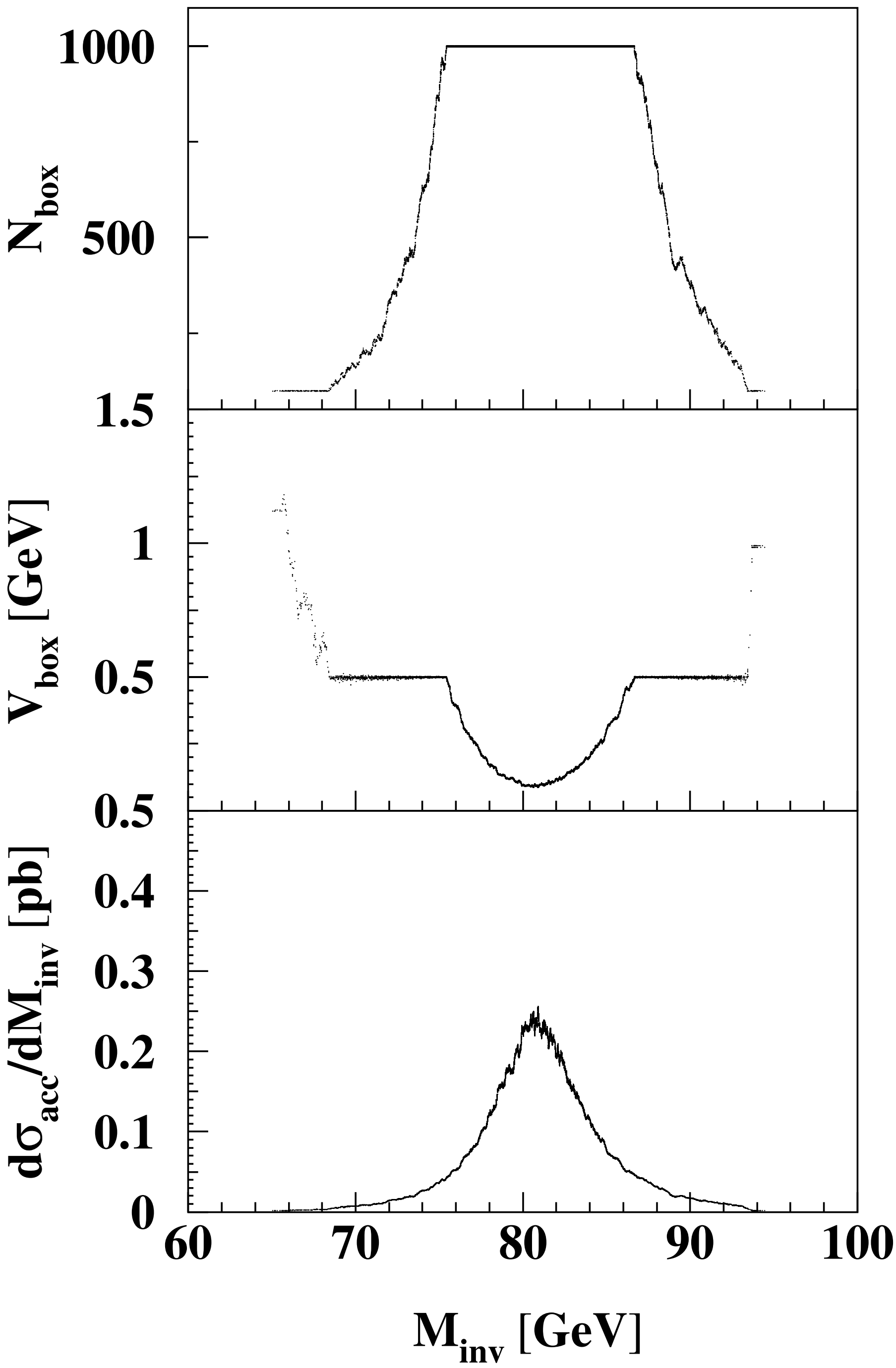

Figure 5.2: *Illustration of the box occupancy (N_{box}) and box volume (V_{box}) for the box algorithm with the required constraints of a fixed box size of* $0.5\ \mathrm{GeV}$ *unless the number of events is outside the range of 100 and 1000 events. The normalised ratio between the box occupancy and box volume is the differential cross-section.*

In the re-weighting method each Monte Carlo event is assigned a weight

$$w_i(M_{\mathrm{W}}^{fit}, \Gamma_{\mathrm{W}}^{fit}) = \frac{|\mathcal{M}_{ffff}(M_{\mathrm{W}}^{fit}, \Gamma_{\mathrm{W}}^{fit}, p_1, p_2, p_3, p_4)|^2}{|\mathcal{M}_{ffff}(M_{\mathrm{W}}^{MC}, \Gamma_{\mathrm{W}}^{MC}, p_1, p_2, p_3, p_4)|^2}, \tag{5.11}$$

which is the ratio of the squared matrix element $|M|^2$ for the process $\mathrm{e^+e^-} \rightarrow \mathrm{WW} \rightarrow ffff$ for the fit parameters M_{W}^{fit} and $\Gamma_{\mathrm{W}}^{fit}$ to the squared matrix element for a generated mass and width, M_{W}^{MC} and Γ_{W}^{MC}. The four-momenta of the final state fermions, p_1, p_2, p_3, p_4, are the generator level values.

The Monte Carlo generator EXCALIBUR [44, 45] is used to calculate the four fermion final state matrix elements. In EXCALIBUR the photon radiation is not included. However, the Monte Carlo events generated by KANDY [12] do include ISR and FSR photons. The fermion system should be transformed to a new system without radiation.

ISR reduces the centre-of-mass energy $\sqrt{s}$ and is corrected for by calculating a new effective centre-of-mass energy $\sqrt{s'}$. The four-momenta of the final state fermions are boosted to the summed ISR photon momentum. The FSR photon momentum is added to the fermion which emitted this photon.

Every event of the Monte Carlo sample can be re-weighted according to the generator level information to obtain a new Monte Carlo with mass M_{W}^{fit} and width $\Gamma_{\mathrm{W}}^{fit}$. The differential cross-section and cross-section are now determined from the weighted Monte Carlo sample as,

$$\frac{d\sigma_{\mathrm{WW}}^{acc}}{dM_{\mathrm{inv}}}(M_{\mathrm{inv}}^i) = \frac{1}{\mathcal{L}_{MC}} \cdot \frac{1}{V_{box}^i} \cdot \sum_{j \in B_i} w_j(M_{\mathrm{W}}^{fit}, \Gamma_{\mathrm{W}}^{fit}) \tag{5.12}$$

$$\sigma_{\mathrm{WW}}^{acc} = \frac{1}{\mathcal{L}_{MC}} \cdot \sum_{i=1}^{N_{acc}^{MC}} w_i(M_{\mathrm{W}}^{fit}, \Gamma_{\mathrm{W}}^{fit}), \tag{5.13}$$

where B_i is the set of Monte Carlo events for a data point i in a box. All the events have a weight of 1 in equations (5.8) and (5.10), which is now modified in equations (5.12) and (5.13) by re-weighting the events.

Figure 5.3 shows the invariant mass spectrum of a Monte Carlo sample of $80.5\ \mathrm{GeV}$ which is re-weighted to $80.0\ \mathrm{GeV}$ and $81.0\ \mathrm{GeV}$. The shift of the peak of the invariant mass spectrum, with respect to the original Monte Carlo to a lower and higher mass respectively, for the re-weighted spectrum, can be clearly observed.

5.4 Jet pairing

Chapter 4 describes the kinematic fit to improve the resolution of the measurement, while the previous sections explain the method to extract the mass from the data.

Before proceeding to the test of the fit method and to the actual fit of the data, an additional remark should be made about the four jet channel.

The $qqqq$ channel has four jets. Since the equal mass constraint is imposed in the kinematic fit, the jets should be paired together before the $5C$-fit is applied. Three different pairings can be made. To determine the mass for this channel it is necessary to find the pairs which come from

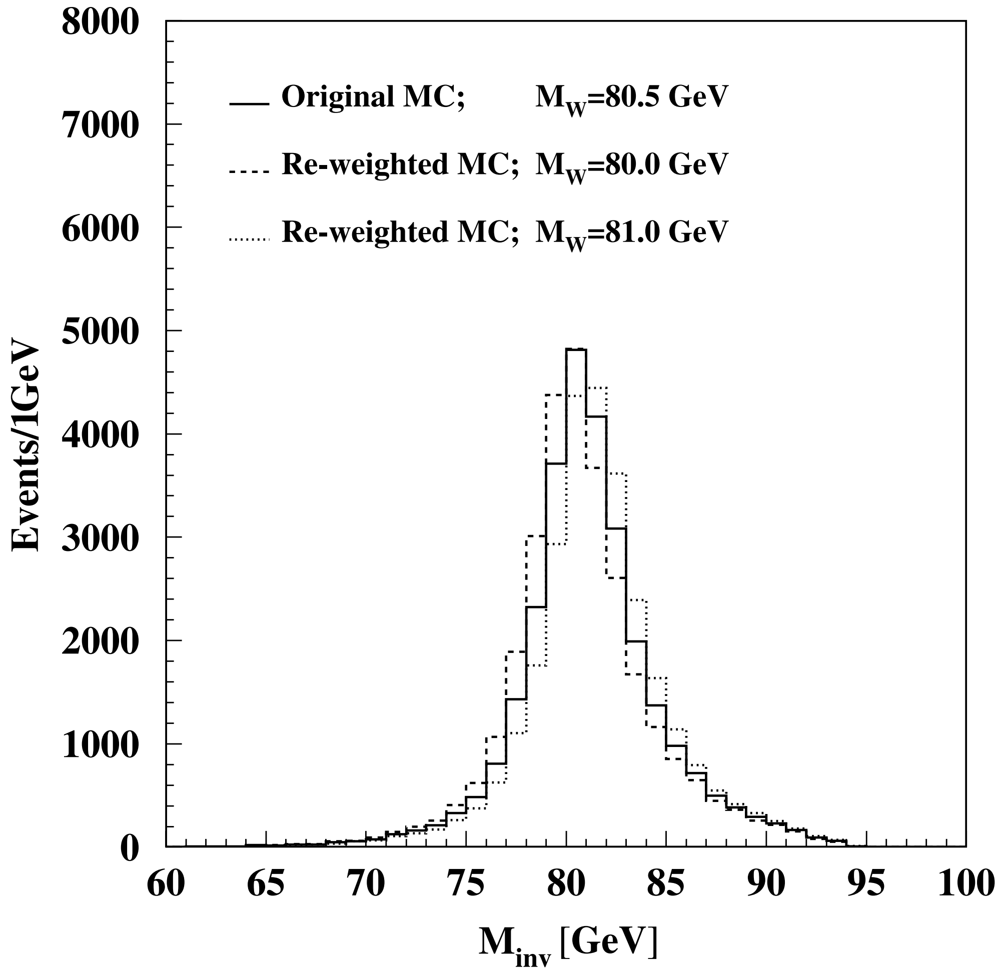

Figure 5.3: *The invariant mass spectrum of a Monte Carlo sample with a generated mass of* $M_\mathrm{W} = 80.5$ GeV *(solid line) is re-weighted to represent a Monte Carlo invariant mass spectrum with generated mass* $M_\mathrm{W} = 80.0$ GeV *(dashed line) and* $M_\mathrm{W} = 81.0$ GeV *(dotted line).*

the same W to reconstruct the mass. This is not straight forward and different approaches exist with varying efficiency to find the correct pairs [41, 58, 62, 63].

The methods typically have a pairing efficiency of about 74% for the lower energy points which drastically decreases to 65% for increasing centre-of-mass energies.

The best performance is obtained with a neural network based approach [64]. The neural network is trained at all centre-of-mass energies. The following eight input variables are used in the neural network:

- Difference of invariant masses: $\Delta M = |M(\mathrm{pair1}) - M(\mathrm{pair2})|$;
- Sum of invariant masses: $\Sigma M = M(\mathrm{pair1}) + M(\mathrm{pair2})$;
- Sum of di-jet angles: $\Sigma\alpha = \alpha(\mathrm{pair1}) + \alpha(\mathrm{pair2})$.
  The di-jet angle, $\alpha(\mathrm{pair}i)$, is the angle between two jets;
- Minimum di-jet angle: $\min\alpha = \min(\alpha(\mathrm{pair1}), \alpha(\mathrm{pair2}))$;

- Difference of pair energies: $\Delta E = |E(\text{pair1}) - E(\text{pair2})|$;
- Minimum energy difference: $\min \Delta E = \min(\Delta E(\text{pair1}), \Delta E(\text{pair2}))$;
- Matrix element: $|\mathcal{M}(M_{\mathrm{W}}, \text{pair1}, \text{pair2})|^2$.
  The matrix element is calculated with EXCALIBUR, in which $M_{\mathrm{W}} = 80.50$ GeV;
- Difference of pair charges: $\Delta Q = |Q(\text{pair1}) - Q(\text{pair2})|$.

Not only the efficiency is higher with about 77% compared to other methods, but it is also almost unchanged at all centre-of-mass energies.

In figure 5.4 the correct pairs show a peak at higher values of the neural network output, while the wrongly paired events peak at lower values of the neural network output. A small

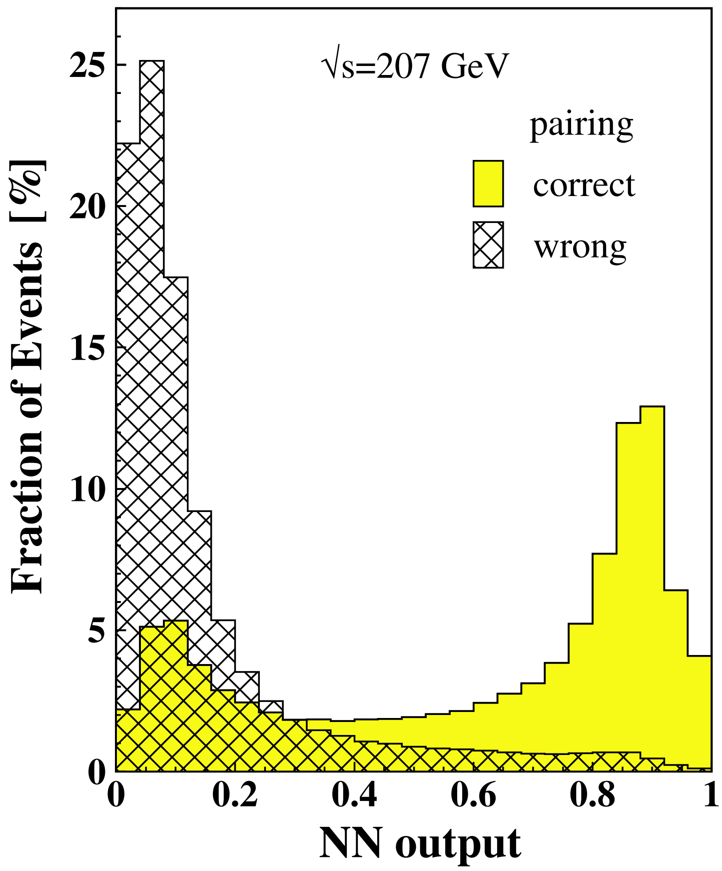

Figure 5.4: *Neural network output of the pairing algorithm at* $\sqrt{s} = 207$ GeV *in fraction of events. The wrong pairing is peaked towards zero. The correctly paired events show a peak at higher values of the neural network output.*

peak is seen for the correct pairs at the lower neural network output values. This comes from badly reconstructed events or events for which the separation between two pairings is difficult to establish.

The pairs are arranged according to their neural network output. The pair with the highest neural network output of an event is classified as the first pairing and consequently the second highest output as the second pairing and the lowest neural network output as the third pairing. Figure 5.5 shows the mass distribution of the Monte Carlo sample at $\sqrt{s} = 207$ GeV for the three pairings. The correct pairing and wrong pairing are shown on the total sample. One can conclude from this that the efficiency of the pairing decreases and the information on the mass reduces conform the classification of the pairing. Hence, I will only use the first pairing for the $qqqq$ events.

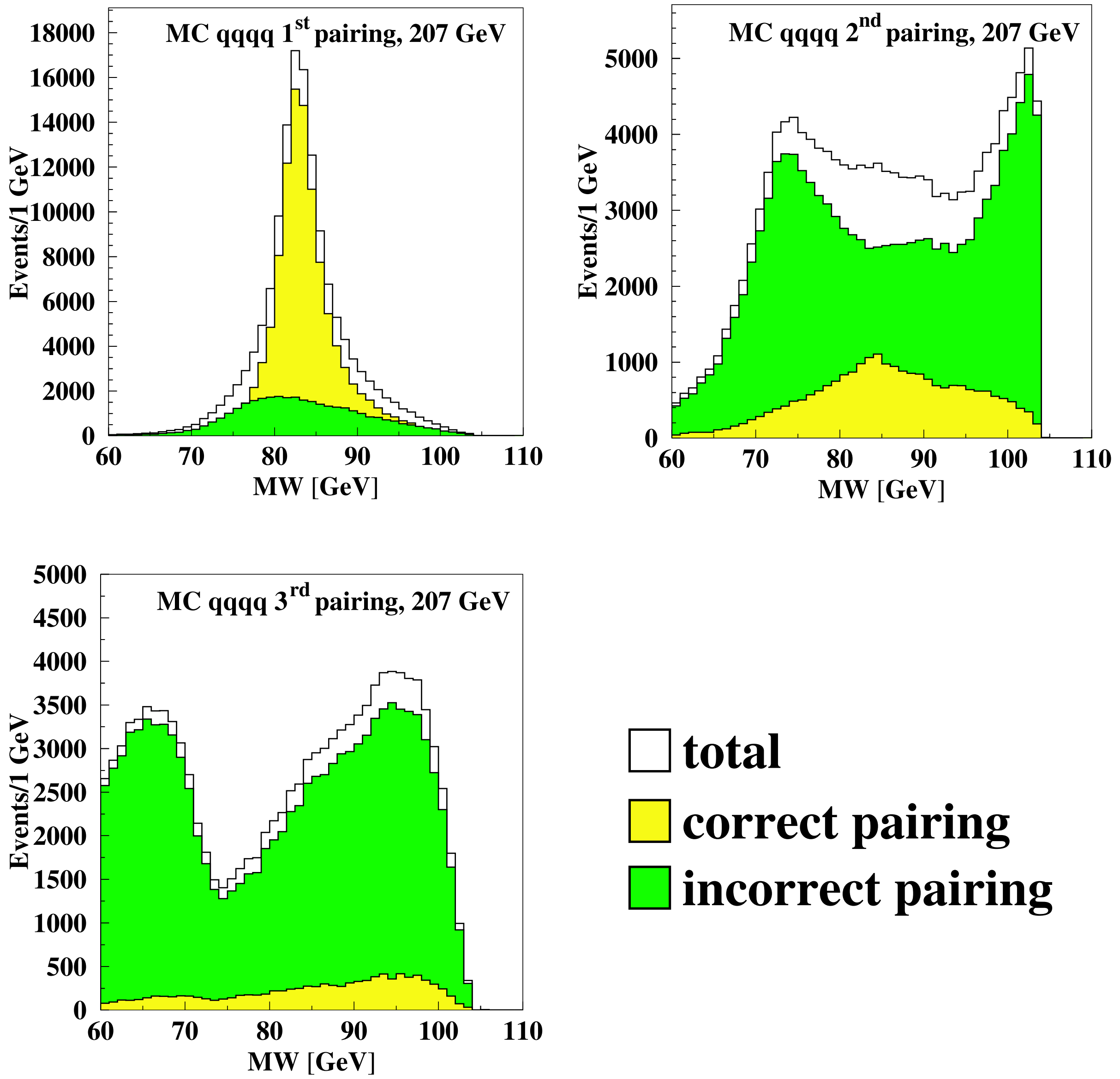

Figure 5.5: *The first pairing has the highest pairing efficiency and shows the* W *mass distribution correctly, in contrast to the second pairing. The second pairing has a lower pairing efficiency and does not exhibit the mass peak in the total sample. The third pairing is even worse and does also not contain any useful information on the mass.*

5.5 Testing the fit method

Sections 5.1, 5.2 and 5.3 describe the procedure to extract the W mass from the data samples. To ensure that the implementation is correct and the fit program determines the correct mass and width of the W boson with the right statistical error, two tests are performed.

In the first test the bias and linearity are examined. The second test, which is described in section 5.5.2, verifies whether the estimated statistical error of the fit is correctly determined.

5.5.1 The linearity test

To ensure that the fit program does determine the measured parameters, M_{W} and Γ_{W}, correctly and to show it has no bias, large Monte Carlo samples with different underlying generated parameters, five for the mass fit and another five for the width fit, are used to fit a reference Monte Carlo sample. Approximately 10,000 events are generated per baseline Monte Carlo sample.

The reference sample has been generated at $\sqrt{s} = 189$ GeV with $M_{\mathrm{W}} = 80.50$ GeV and $\Gamma_{\mathrm{W}} = 2.11$ GeV. This sample is treated as data. The baseline Monte Carlos are produced at five different generated mass values ranging from 80.00 GeV to 81.00 GeV with steps of 0.25 GeV with a corresponding Γ_{W} calculated by the Standard Model relation in equation (1.38). Similarly, different Monte Carlo samples are produced with generated Γ_{W} varying from 1.51 GeV to 2.71 GeV with steps of 0.30 GeV at the fixed mass value of 80.50 GeV.

Figure 5.6 graphically represents the results when the reference sample has been fitted with five different baseline Monte Carlo samples. The left hand-side of figure 5.6 shows the effect on the mass measurement, while the right-hand side illustrates the effect on the width. In the upper part of these figures the generated values are plotted on the abscissa, while along the ordinate the fit values are set. The diagonal line gives the ideal positions of the points. The lower part of the figures shows the difference between the fitted and generated values.

A straight line has been fitted through the difference of fitted and generated value points, i.e.

$$f(M_{\mathrm{W}}) = b_M + s_M(M_W - 80.50), \tag{5.14}$$

$$f(\Gamma_{\mathrm{W}}) = b_\Gamma + s_\Gamma(\Gamma_W - 2.11). \tag{5.15}$$

Parameters b_M and b_Γ are the biases of the fits at the reference points. Their slopes are parametrised by s_M and s_Γ respectively. The straight line fits give $b_M = 12 \pm 13$ MeV, $s_M = -0.039 \pm 0.038$ for the mass and $b_\Gamma = 19 \pm 30$ MeV , $s_\Gamma = 0.036 \pm 0.078$ for the width. One can observe in the figures that the fitted M_{W} and Γ_{W} obtained from the mass and width extraction method are well reproduced within the statistical error.

5.5.2 Statistical error test

In the fit procedure the statistical uncertainty of the mass and width measurement are estimated. These errors are calculated from the log-likelihood curve as the difference between the determined mass at the minimum of the curve and the mass at the point where the log-likelihood is 0.5 higher than at its minimum. The statistical errors depend on the number of data events as well as on the invariant mass distribution.

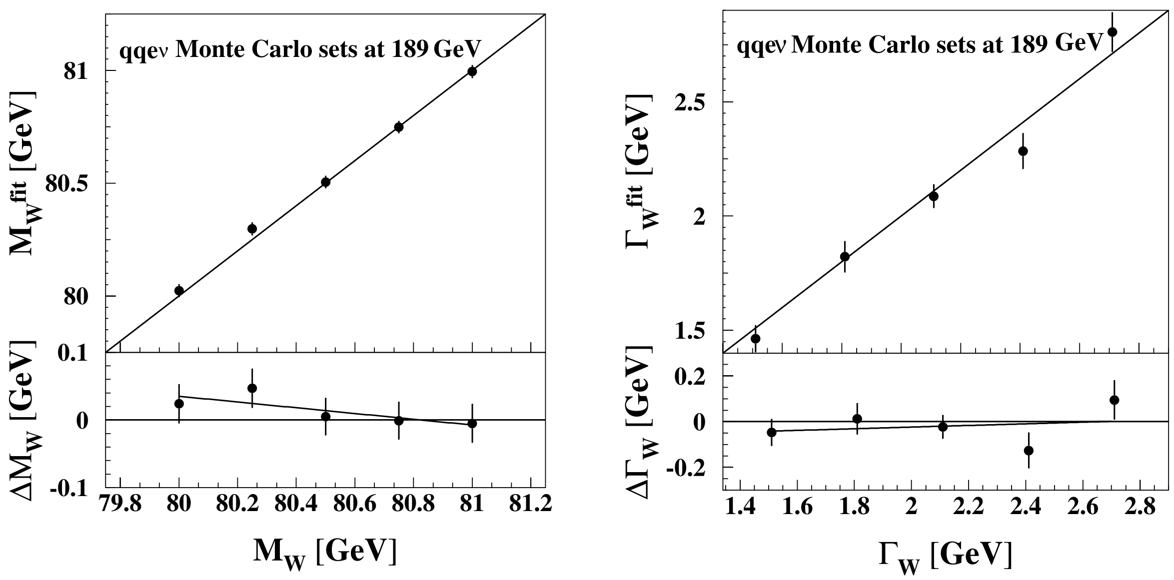

Figure 5.6: *The figure on the left hand-side shows the fit for the mass. On the right hand-side the results for the width are represented. The upper parts of the plots show the results of the fit for different baseline Monte Carlos to the reference sample. In the lower part of the plots the difference between fitted and generated value are shown. From the line which has been fitted through these points, the bias and slope are deduced.*

To confirm that the estimation provided by the fit program is done properly, a Monte Carlo test is performed. By taking events randomly out of one baseline Monte Carlo sample, many small samples can be constructed. These are handled in the same way as data in the mass and width fit program, by fitting them with the parent Monte Carlo. The mass and error are extracted for each small sample and plotted. The root-mean-square (RMS) of the extracted mass distribution should agree with the average of the estimated error distribution.

The size of the samples is chosen such that it agrees with the measured cross-section. To prevent any bias in the estimation, the randomly chosen events are excluded from the baseline Monte Carlo. Approximately 1,000 of such samples are constructed and fitted.

Figure 5.7 shows the histograms for the fitted mass values and the error estimation for the $qqe\nu$ channel at 189 GeV with Monte Carlo samples generated at a mass of 80.50 GeV and a width of 2.11 GeV. The average value of the fitted mass distribution is 80.498 ± 0.012 GeV. Within the error the generated mass value is very well reproduced. The RMS of the mass distribution of 174 ± 9 MeV is compared with the average value of 169 ± 16 MeV of the error estimation distribution. The error on the average fit error comes from the spread of the distribution.

Figure 5.8 shows the plots for the width calculations. The average of the distribution in the left plot is 2.084 ± 0.013 GeV. For the width fit distribution the RMS yields 429 ± 10 MeV and the average of the error 430 ± 48 MeV.

Comparing the results the RMS and the average of the error shows these values to be compatible within their statistical error for both the mass and width.

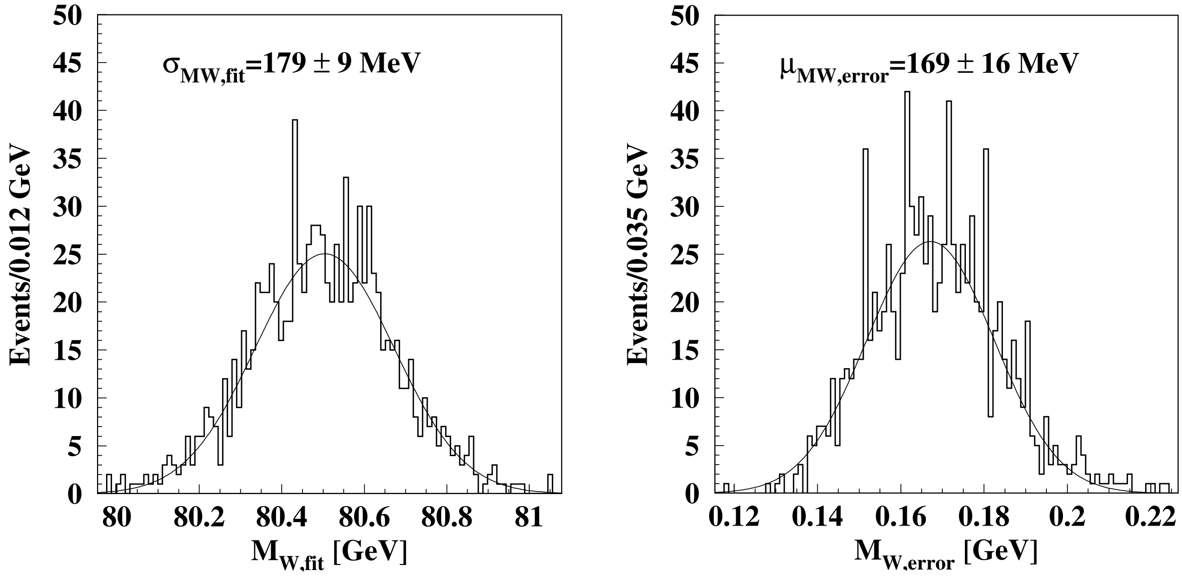

Figure 5.7: *Approximatly 1,000 small samples are fitted with their corresponding baseline Monte Carlo to test the results of the expected errors. On the left plot the fitted mass distribution is shown. The distribution of the expected errors is shown on the right hand-side.*

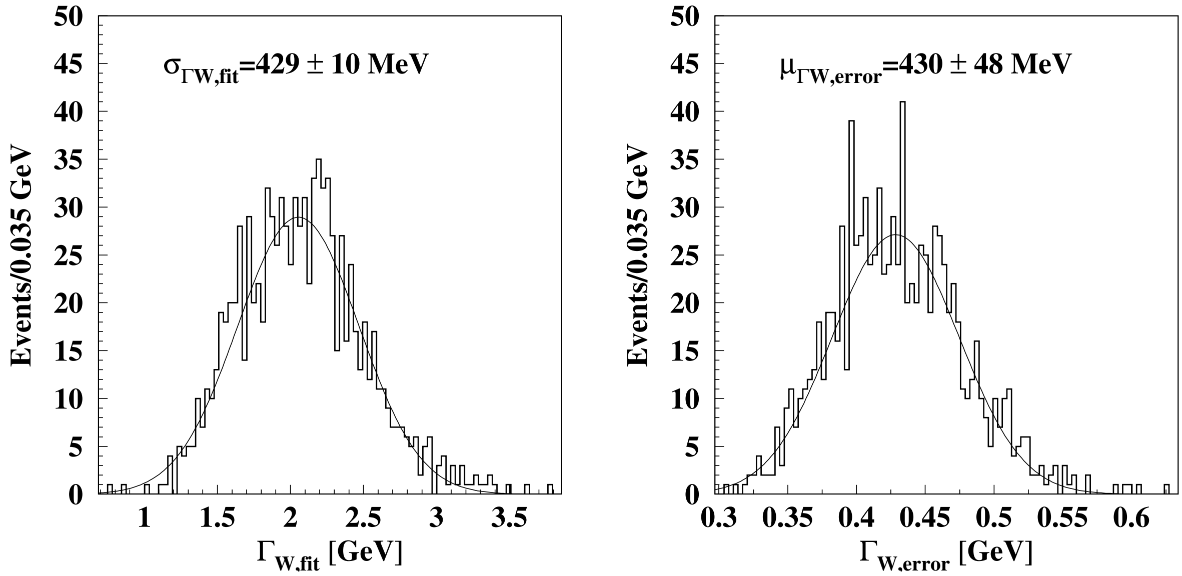

Figure 5.8: *Approximately 1,000 small samples are fitted with their corresponding baseline Monte Carlo to test the results of the expected errors. On the left plot the fitted distribution of the width is shown. The distribution of the expected errors is shown on the right hand-side.*

5.6 Mass and width fit results

The W mass and width are determined in the data samples at each energy point with the unbinned log-likelihood fit by means of the box and reweighting method as described in sections 5.1 , 5.2 and 5.3.

Table 5.1 and table 5.2 contain the results of the analyses for the $qqe\nu$ and $qq\mu\nu$ channels respectively. Both the one- and two-parameter fits are shown. The number of events is the number after rejecting events with a fit probability lower than 5%, to remove background events and badly reconstructed events. Also the range where the fit is applied is restricted to the invariant mass above 65 GeV. Events which are far from the peak are not sensitive to the mass. The Monte Carlo sampling density for these events is very low, which causes the box-size to be more than 1 GeV. The kinematical edge defines the end point of the range in which the fit is performed.

There are too few data at 208 GeV for the two-parameter fit to converge.

Table 5.1: *The mass and width of the* W *boson extracted from the* $qqe\nu$ *final state at* $\sqrt{s} = 189 - 208$ GeV. *The one-parameter fit and two-parameter fit results are presented. The number of events is the number of events used in the fit.*

$\sqrt{s}$ [GeV]	#data events	one-parameter fit	two-parameter fit	
		$M_{\rm W}$ [GeV]	$M_{\rm W}$ [GeV]	$\Gamma_{\rm W}$ [GeV]
189	269	80.06 $\pm$ 0.18	80.05 $\pm$ 0.19	2.59 $\pm$ 0.52
192	58	80.64 $\pm$ 0.48	80.52 $\pm$ 0.54	3.73 $\pm$ 1.24
196	121	80.50 $\pm$ 0.31	80.47 $\pm$ 0.33	2.64 $\pm$ 0.74
200	117	80.32 $\pm$ 0.29	80.31 $\pm$ 0.30	2.26 $\pm$ 0.75
202	46	80.24 $\pm$ 0.50	80.25 $\pm$ 0.51	2.02 $\pm$ 1.25
205	125	80.31 $\pm$ 0.29	80.24 $\pm$ 0.34	2.70 $\pm$ 0.80
207	178	80.40 $\pm$ 0.22	80.43 $\pm$ 0.20	1.50 $\pm$ 0.52
208	6	79.17 $\pm$ 0.79	-	-

The results of the fit for the $qq\tau\nu$ channel are shown in table 5.3. Only the hadronically decaying part is used in the reconstruction. The jet-jet part of the event is rescaled with a factor so that the sum of the energy of the hadronic jets is equal to half the centre-of-mass energy. Events with an invariant mass higher than 65 GeV only are considered in the fit.

Events with a fit probability lower than 5% are also rejected in the $qqqq$ case, as in the $qqe\nu$ and $qq\mu\nu$ channels. The accepted range of the invariant mass is from 65 GeV upwards. The pairing with the highest probability is used in the fit in table 5.4.

Figure 5.9 shows the log-likelihood function for the $qqqq$ data at 208 GeV, which shows a proper parabolic curve, which confirms the fact that the error is symmetric. The minimum of this curve is assigned as the measured mass in this data sample.

Combining all the energy points for the measurements of each channel gives the results in table 5.5. These results are obtained by adding the log-likelihood curves for all energy points of a specific channel. The result of such a combination of log-likelihood curves is presented in Figure 5.10. Figure 5.11 shows the combined data and reweighted Monte Carlo fit.

Table 5.2: *The mass and width of the* W *boson extracted from the* $qq\mu\nu$ *final state at* $\sqrt{s} = 189 - 208$ GeV. *The one-parameter fit and two-parameter fit results are presented. The number of events is the number of events used for the fit.*

$\sqrt{s}$ [GeV]	#data events	one-parameter fit	two-parameter fit	
		M_W [GeV]	M_W [GeV]	Γ_W [GeV]
189	269	80.13 ± 0.21	80.13 ± 0.21	1.91 ± 0.50
192	52	80.58 ± 0.52	80.61 ± 0.44	1.32 ± 1.58
196	135	80.20 ± 0.40	80.15 ± 0.41	3.15 ± 0.98
200	117	80.44 ± 0.38	80.37 ± 0.86	0.89 ± 0.89
202	67	80.40 ± 0.54	80.34 ± 0.63	3.31 ± 1.73
205	113	80.24 ± 0.47	80.23 ± 0.48	2.61 ± 1.05
207	207	80.13 ± 0.32	80.12 ± 0.32	2.38 ± 0.74
208	20	79.50 ± 0.79	-	-

Table 5.3: *The mass and width of the* W *boson extracted from the* $qq\tau\nu$ *final state at* $\sqrt{s} = 189 - 208$ GeV. *The one-parameter fit and two-parameter fit results are presented. The number of events is the number of events used in the fit.*

$\sqrt{s}$ [GeV]	#data events	one-parameter fit	two-parameter fit	
		M_W [GeV]	M_W [GeV]	Γ_W [GeV]
189	430	80.12 ± 0.28	80.12 ± 0.29	2.20 ± 0.62
192	57	80.36 ± 0.84	80.37 ± 0.92	3.96 ± 2.03
196	222	80.69 ± 0.49	80.75 ± 0.52	3.01 ± 1.17
200	181	80.45 ± 0.51	80.44 ± 0.52	2.23 ± 1.08
202	77	79.82 ± 0.74	79.71 ± 1.07	4.19 ± 2.00
205	164	81.60 ± 0.56	81.66 ± 0.63	2.64 ± 1.11
207	287	80.34 ± 0.45	80.35 ± 0.48	3.42 ± 1.02
208	17	79.68 ± 1.04	-	-

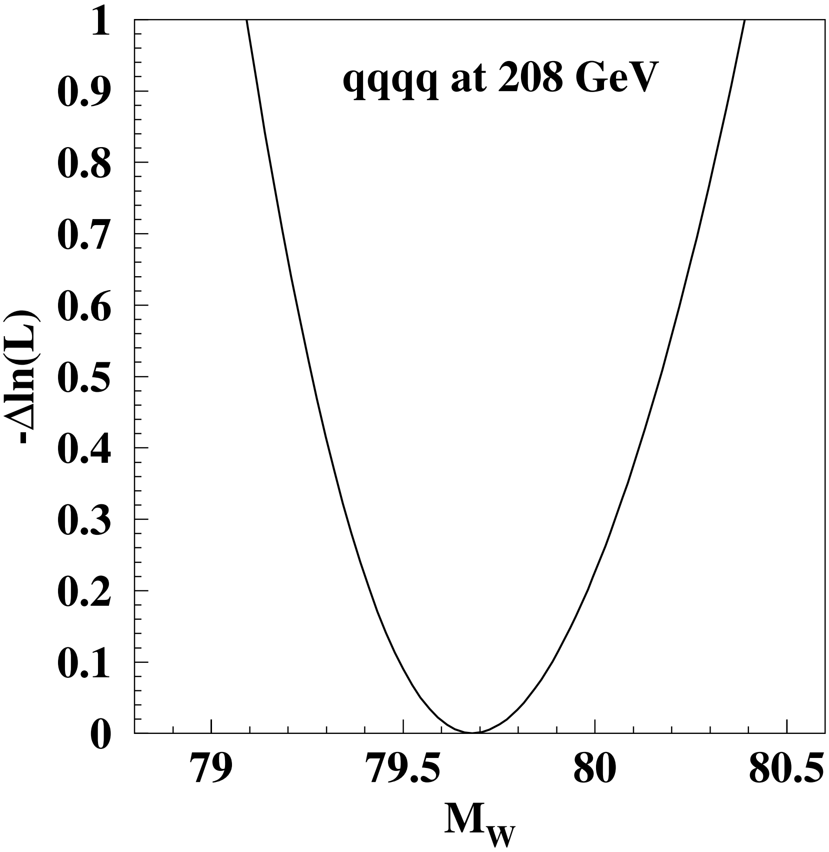

Figure 5.9: *The log-likelihood curve for the $qqqq$ data at 208 GeV. The curve is shifted along the y-axis, by subtracting the minimum value of the log-likelihood, $-\Delta\ln(L)$. The curve is parabolic around the minimum. This attests that the errors are symmetric.*

Table 5.4: *The mass and width of the* W *boson extracted from the* $qqqq$ *final state at* $\sqrt{s} = 189 - 208$ GeV. *The one-parameter fit and two-parameter fit are presented. The number of events is the number of events used for the fit.*

$\sqrt{s}$ [GeV]	#data events	one-parameter fit	two-parameter fit	
		M_W [GeV]	M_W [GeV]	Γ_W [GeV]
189	794	80.51 ± 0.13	80.51 ± 0.13	2.35 ± 0.34
192	146	80.12 ± 0.30	80.12 ± 0.33	2.75 ± 0.79
196	368	80.30 ± 0.19	80.29 ± 0.19	2.19 ± 0.47
200	422	80.17 ± 0.17	80.16 ± 0.18	2.34 ± 0.43
202	162	80.49 ± 0.24	80.48 ± 0.21	1.29 ± 0.60
205	360	80.15 ± 0.18	80.15 ± 0.18	2.10 ± 0.47
207	599	80.48 ± 0.15	80.46 ± 0.15	2.42 ± 0.38
208	33	79.68 ± 0.45	79.57 ± 0.40	1.08 ± 0.69

Table 5.5: *The mass and width of the* W *boson extracted for the combination of the energy points* $\sqrt{s} = 189 - 208$ GeV *for each channel. The one-parameter fit and two-parameter fit results are presented.*

channel	#data events	one-parameter fit	two-parameter fit	
		M_W [GeV]	M_W [GeV]	Γ_W [GeV]
$qqe\nu$	920	80.27 ± 0.10	80.24 ± 0.11	2.42 ± 0.27
$qq\mu\nu$	980	80.21 ± 0.13	80.21 ± 0.13	2.22 ± 0.32
$qq\tau\nu$	1474	80.41 ± 0.17	80.36 ± 0.17	2.43 ± 0.41
$qqqq$	2884	80.34 ± 0.07	80.35 ± 0.06	2.18 ± 0.17

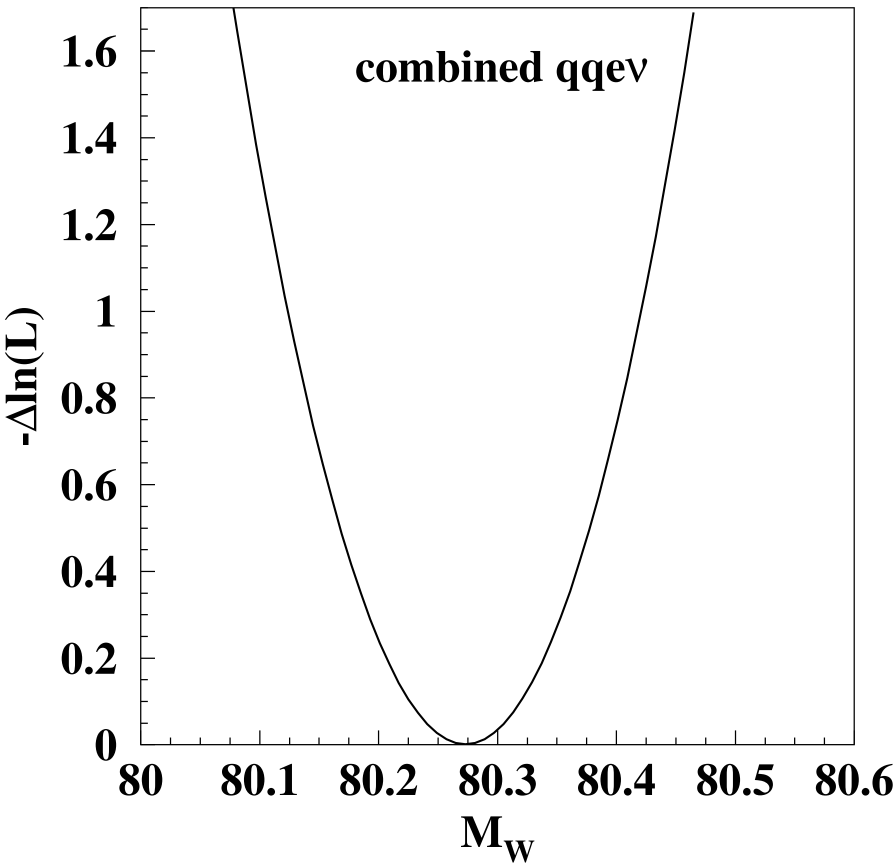

Figure 5.10: *The log-likelihood distribution with the minimum subtracted, $-\Delta\ln(L)$, for the $qq\mathrm{e}\nu$ channel. All separate log-likelihood curves at the different energy points are added together to extract the combined result. The curve is parabolic around the minimum.*

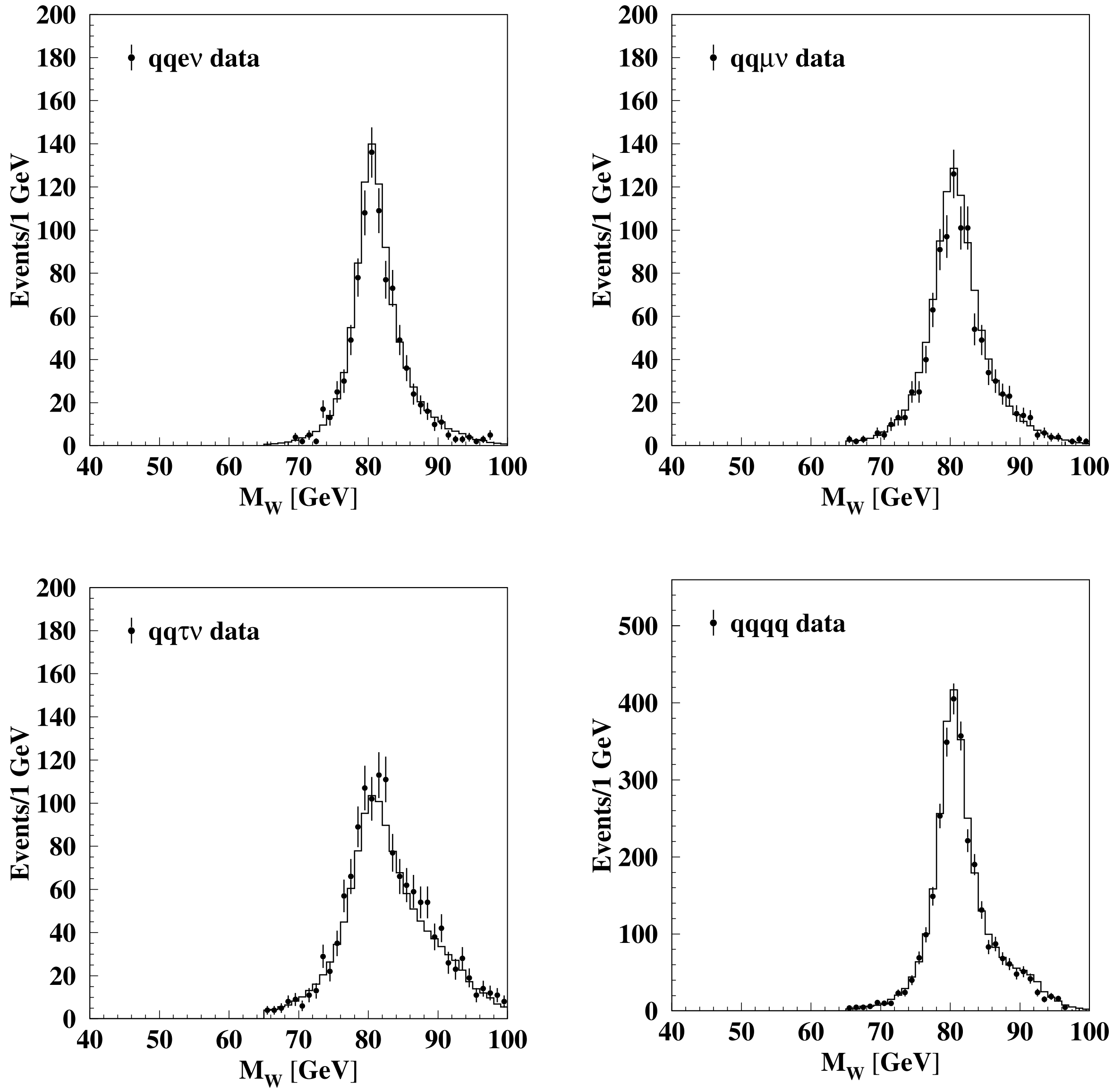

Figure 5.11: *Distribution of the invariant mass for data and the reweighted Monte Carlo.*

Chapter 6

Systematic uncertainties

6.1 Monte Carlo statistics

Although the number of events in the generated Monte Carlo sample is large, the finite number of Monte Carlo events gives rise to a statistical component in the error on M_{W}. In the reweighting method the mass and the width of the W mass distribution are determined by the baseline sample. Using different reference Monte Carlo samples of the same size will show a spread in the fitted values. This variation is the error due to the finite number of events in the baseline sample.

The method described above is not feasible, since there is only one reference sample. To estimate the Monte Carlo statistical error, the sample is split in N_{div} parts with equal number of events. These divided samples are used as baseline to fit the W mass data. The fit results using these reference samples, which correspond to the splitting of the Monte Carlo into N_{div} equal parts, are put into one histogram. The RMS of the mass fit results in this histogram divided by $\sqrt{N_{div}-1}$ is approximately independent of N_{div}.

Figure 6.1 shows the determination of the Monte Carlo statistical error for the mass fit of the $qq\mu\nu$ and $qq\tau\nu$ channels at 189 GeV. In these plots the dots represent the $\mathrm{RMS}/\sqrt{N_{div}-1}$ value for the class of reference samples belonging to N_{div}. The constant number of the line fitted through these points is assigned to the Monte Carlo statistical error for the mass fit.

The same method is applied to determine the Monte Carlo statistical error on the width measurement. Figure 6.2 shows on the left hand-side the $qq\mathrm{e}\nu$ and on the right hand-side the $qqqq$ channel at 189 GeV for the fit of the width.

The constants are calculated only for the 189 GeV Monte Carlo samples. The Monte Carlo statistical error for the other energy points can be determined by scaling the errors at 189 GeV by the ratio $\sqrt{N_{\sqrt{s}}/N_{189}}$, where N_{189} is the total number of Monte Carlo events at 189 GeV and $N_{\sqrt{s}}$ the total number of events of the compared Monte Carlo at the other centre-of-mass energies. The total number of events for each Monte Carlo is almost the same, hence the estimated Monte Carlo statistical error is of the same order for the other Monte Carlo samples at the different energy points. Table 6.1 gives the estimated values. The combination assumes that the values are uncorrelated between different centre-of-mass energies.

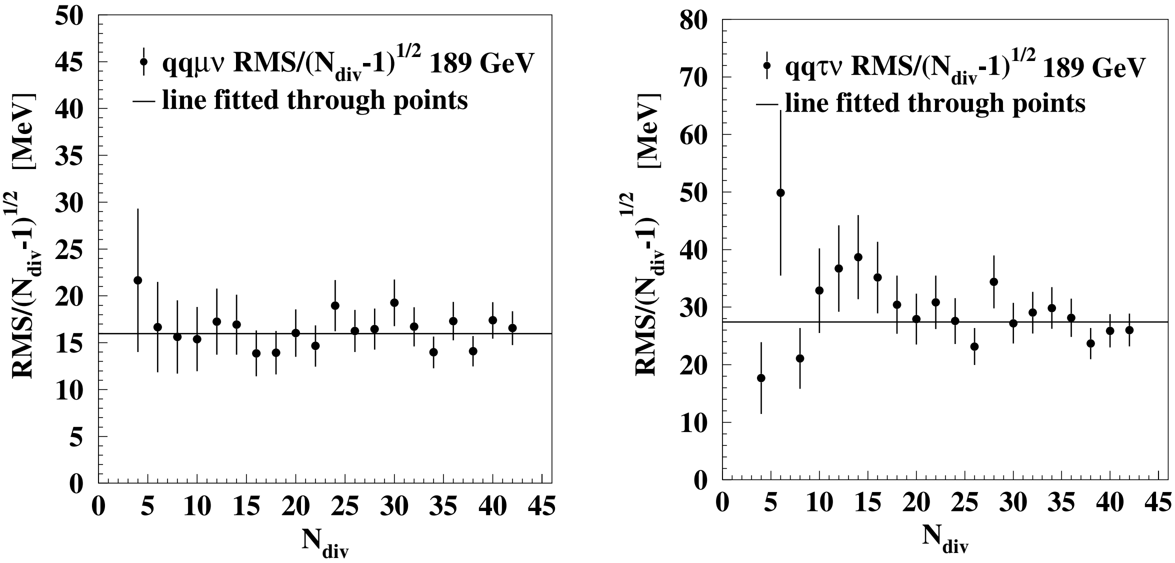

Figure 6.1: *The baseline Monte Carlo is split in a set of N_{div} equal parts. The RMS of the mass fit for each set is divided by $\sqrt{N_{div}-1}$ for the $qq\mu\nu$ and $qq\tau\nu$ channels at $189\ \mathrm{GeV}$. The $\mathrm{RMS}/\sqrt{N_{div}-1}$ distribution is approximately constant. This constant value is the Monte Carlo statistical error.*

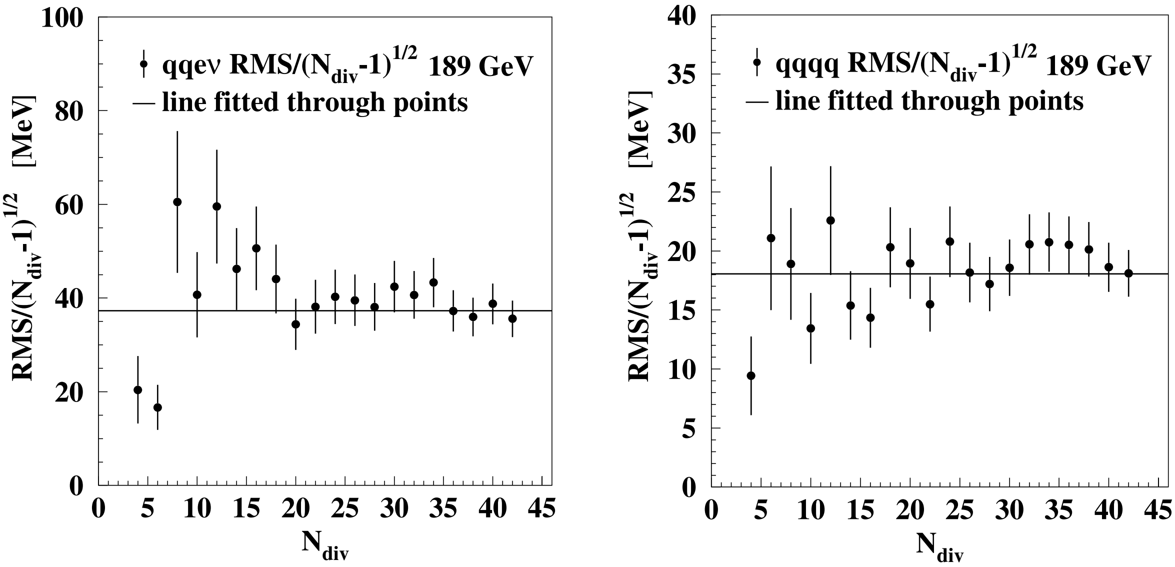

Figure 6.2: *As figure 6.1, for the fit of the* W *width. The results for the* $qqe\nu$ *and* $qqqq$ *channel are shown.*

Table 6.1: *The error on the mass and width due to Monte Carlo statistics for* $\sqrt{s} = 189$ GeV*. The estimations for the other centre-of-mass energies are obtained by multiplying the result at* 189 GeV *by the ratio* $\sqrt{N_{\sqrt{s}}/N_{189}}$*, where* $N_{\sqrt{s}}$ *is the total number of events at another centre-of-mass energies. At the bottom of the table the combined results at all centre-of-mass energies is given.*

$\sqrt{s}$ [GeV]	Monte Carlo statistical error [MeV]							
	ΔM_{W}				$\Delta\Gamma_{\mathrm{W}}$			
	$qq\mathrm{e}\nu$	$qq\mu\nu$	$qq\tau\nu$	$qqqq$	$qq\mathrm{e}\nu$	$qq\mu\nu$	$qq\tau\nu$	$qqqq$
189	14	16	27	8	37	40	84	18
189-208	6	7	13	3	16	20	41	7

6.2 Background

Possible background events leaving a similar signature in the detector contaminate the WW sample selected from data. These events are subtracted in the W mass fit by taking them into account when performing the fit, as has been described in section 5.1.

Uncertainties in these backgrounds introduce systematic errors on the measurement. To estimate the effect, the background cross sections should be modified according to their theoretical uncertainties. For ZZ the uncertainty on the theoretical prediction is $\pm 2\%$, while the uncertainty on the cross section of the Zee background is $\pm 5\%$. Since KandY generates all four fermion final states, these events are included in one Monte Carlo. No effort is made to separate these two background events in the Monte Carlo. Therefore, the total four-fermion background is modified with $\pm 5\%$.

Study has shown that the predicted cross section of the accepted $q\bar{q}(\gamma)$ background is too low for four jet events due to uncertainties in the prediction for events when two gluons are radiated [65]. The $\mathrm{e^+e^-} \to q\bar{q}(\gamma)$ Monte Carlo is weighted with the ratio of the data and Monte Carlo distributions of the y_{34} variable as a function of y_{34} in the Z decay. The accepted cross section in the Monte Carlo, for a neural network output greater than 0.6, is increased by 12.7% to agree with data, while half of the difference is taken as an additional systematic uncertainty for the $qqqq$ channel only.

Table 6.2 shows the estimated uncertainties arising from background events.

6.3 Jet measurement

The mass measurement is affected by the reconstruction of the energy and angles of the electron, the muon and the jets. The simulated Monte Carlo invariant mass spectrum is compared with the data invariant mass spectrum in the box method fit procedure. Accordingly, it is important that the reconstruction of the lepton and jet energy and angles agree between Monte Carlo and data. Di-jet and di-lepton events, selected during calibration runs at the Z-resonance, are used as

Table 6.2: *The accepted cross section of the background Monte Carlo's are rescaled, after which the mass and width fit are reperformed. The observed shift with respect to the shift without rescaling the cross section, is assigned as the systematic error on the mass and width measurement due to uncertainties in the background.*

channel	ΔM_{W} [MeV]	$\Delta\Gamma_{\mathrm{W}}$ [MeV]
$qq\mathrm{e}\nu$	4	30
$qq\mu\nu$	4	37
$qq\tau\nu$	3	87
$qqqq$	16	84

control samples to cross check the reconstruction.

For the jets, the Monte Carlo and the data agree up to $30\ \mathrm{MeV}$ for the absolute measured energy, i.e. the energy scale, up to 0.5% for the energy resolution and up to $0.1°$ for the angular resolution.

The uncertainties on the mass due to uncertainties on the jet measurement, are found using modified Monte Carlo samples. Depending on the channel, the measured energy is increased or decreased by a value between $0.2\ \mathrm{GeV}$ to $1.0\ \mathrm{GeV}$, while the energy resolution of the jet is smeared by 2% to 10% and the jet angle resolution is smeared by $0.5°$ to $3.0°$. The results for the different channels are shown in table 6.3.

However, the modifications in the altered Monte Carlo samples are large compared to the uncertainties on the energy and angle measurements of the jets. For that reason, the uncertainties are scaled down to match the actual energy and angular uncertainties by the estimated Monte Carlo and data comparison at the Z-resonance. If different Monte Carlo samples are available the average shift is taken to determine the effect of the energy scale, the smearing or the angular smearing. The total systematic error due to the jet measurement is determined by combining these values

$$jet\ systematics = \sqrt{(smearing)^2 + (jet\ scale)^2 + (angle\ smearing)^2} \tag{6.1}$$

The resulting errors for the different channels are shown at the bottom of table 6.3.

6.4 Lepton measurement

To determine the uncertainties for the lepton measurement on the $qq\mathrm{e}\nu$ and $qq\mu\nu$ channel an uncertainty of $50\ \mathrm{MeV}$ is chosen on the energy scale, since the calibration was tested with a precision of $40\ \mathrm{MeV}$.

The Monte Carlo is modified by shifting and smearing the energy and angles. The energy scale is varied by 10% of the resolution. This agrees with a shift of about $50\ \mathrm{MeV}$ for the electron according to the energy of the electron. A change in the energy of the muon by 10% of the resolution results in a much larger shift in the energy of the muon than for the electron, due to

Table 6.3: *Uncertainties in the measurement of the jets lead to uncertainties in the mass and width measurement. By shifting the energy and angle scale and by smearing the energy and angle resolution, the error on the mass and width measurements are determined. Since these variations are larger than the expected variations in the jet measurements, the values are rescaled according to the expected uncertainties. At the bottom of the table the total expected systematic error coming from the jet measurement is given.*

	$\Delta M_{\rm W}$ [MeV]				$\Delta\Gamma_{\rm W}$ [MeV]			
	$qq\mathrm{e}\nu$	$qq\mu\nu$	$qq\tau\nu$	$qqqq$	$qq\mathrm{e}\nu$	$qq\mu\nu$	$qq\tau\nu$	$qqqq$
E_{jet} smearing by 2%	-	-	-7	-	-	-	63	-
E_{jet} smearing by 5%	-12	20	-16	2	43	117	188	4
E_{jet} smearing by 10%	-	-	-	4	-	-	-	10
$E_{jet} + 0.2$ GeV	-	37	-	2	-	-10	-	7
$E_{jet} + 1.0$ GeV	66	192	-	6	27	-97	-	10
$E_{jet} + 0.5$ GeV	-	-	61	-	-	-	-12	-
$E_{jet} - 0.2$ GeV	-	-38	-	-5	-	25	-	-10
$E_{jet} - 1.0$ GeV	-74	-197	-	-9	64	111	-	-22
$E_{jet} + 0.5$ GeV	-	-	-62	-	-	-	51	-
jet angle smearing by $0.5°$	-	-4	-	-	-	-1	-	-
jet angle smearing by $1.0°$	-	-	-12	20	-	-	89	38
jet angle smearing by $2.0°$	-11	-19	-	-	71	167	-	-
jet angle smearing by $3.0°$	-	-	-67	-	-	-	633	-
jet systematics	3	6	4	2	6	13	22	4

the difference in the energy resolutions of the two leptons. The results of the muon should be rescaled to agree with the uncertainty of $50\ \mathrm{MeV}$ on the energy scale.

The agreement for the energy and angular resolution is not worse than 25% of the resolution.

The result are shown in table 6.4. The assigned systematic errors on the mass due to the lepton measured are shown at the bottom of the table.

Table 6.4: *The systematic errors due to uncertainties on the lepton measurement are listed. The observed shifts for the muons are down scaled as explained in the text.*

	ΔM_{W} [MeV]		$\Delta\Gamma_{\mathrm{W}}$ [MeV]	
	$qqe\nu$	$qq\mu\nu$	$qqe\nu$	$qq\mu\nu$
E_l shift by $+10\%$ of σ_E	8	58	-2	-3
E_l shift by -10% of σ_E	-12	-55	11	20
E_l smearing by 25% of σ_E	-4	-4	10	26
lepton angle smearing by 25% of σ_θ	0	-3	1	2
lepton systematics	11	15	10	26

6.5 Initial and final state radiation

Radiation of photons from the four fermions in the final state is not included in the matrix element implemented in EXCALIBUR. The KandY Monte Carlo however generates final state radiation (FSR).

To calculate the weight of an event, the FSR photon can be combined with the lepton or jet before the four momenta are passed to EXCALIBUR. Its momentum is added to the momentum of the nearest charged particle. Figure 6.3 shows the FSR spectrum of the electron and the tau channel as generated by the KandY Monte Carlo at $205\ \mathrm{GeV}$.

The effect of FSR is studied by removing all events which have a photon radiated. The observed difference is the systematic error in table 6.5. In the $qqqq$ channel, JETSET takes care of the FSR. Hence, fragmentation and FSR are not treated separately in this channel. Photon radiation affects the four jet channel less than the semi-leptonic channel, since the total energy for each four jet event can be reconstructed. The uncertainty on the four jet channel is taken as about one half of the average shift on the semi leptonic channel

The W pair production and decay in KandY includes the initial state radiation effects up to $\mathcal{O}(\alpha^3)$ in the leading-logarithm approximation in the YFS exponentiation framework. To estimate the uncertainty, mass fits are performed considering only ISR up to $\mathcal{O}(\alpha^2)$ and compared to the full $\mathcal{O}(\alpha^3)$ fit. The full difference is assigned as a systematic error and is listed in table 6.5.

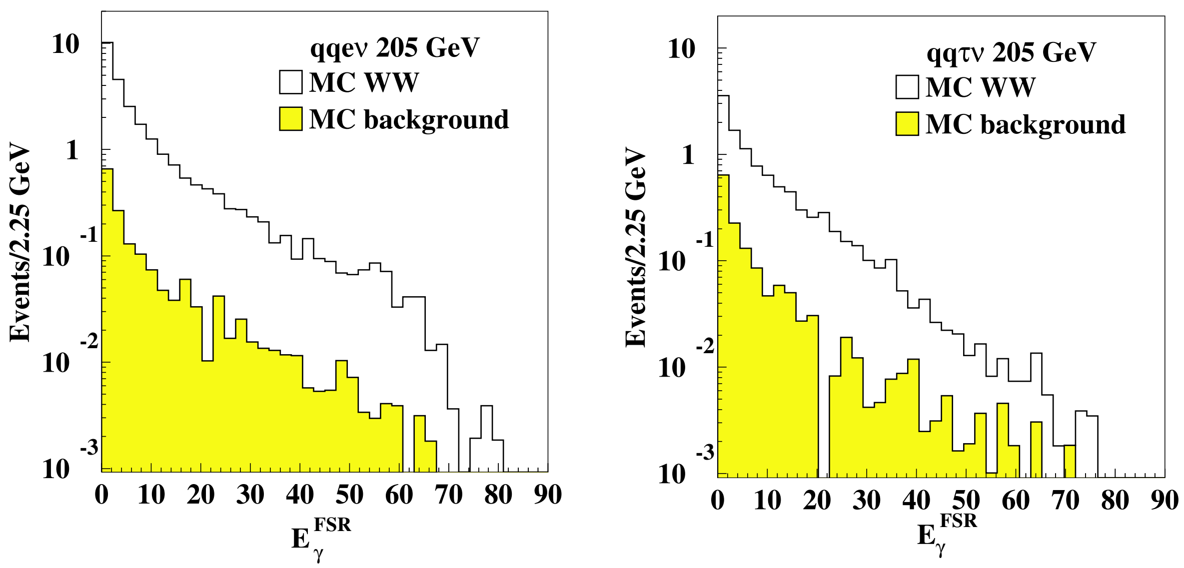

Figure 6.3: *The generated KandY FSR spectrum of the* $qqe\nu$ *en* $qq\tau\nu$ *channel at* 205 GeV *normalised to the luminosity of the data.*

6.6 Fragmentation

Fragmentation is a complex process in which the produced quarks from a W decay evolve to the observed jets. This is a QCD process and has no fully analytical prediction. As has been mentioned in section 1.5.2 various fragmentation schemes exist, which are implemented in the Monte Carlo generators.

JETSET is the default fragmentation model used for KandY baseline samples. Additional KandY Monte Carlo samples are produced with ARIADNE and HERWIG fragmentation schemes. The difference between these three samples should be compared to estimate the systematic error originating from the fragmentation uncertainty.

Each of the models give a satisfactory description of the data. Therefore, the systematic error is estimated by the average of both shifts in table 6.6.

6.7 Final state interactions

Final state interactions are subdivided into colour reconnection and Bose-Einstein correlations. The colour reconnection could lead to momentum transfer which alters the reconstructed quantities and thereby the mass and width measurement.

6.7.1 Colour reconnection

To study the effects of colour reconnection, a variety of phenomenological models exist. Section 1.5.3 gives a overview of these models. The SK1 model is implemented in PYTHIA and has a free parameter κ. This free parameter determines the reconnection probability in the SK1 model. The fraction of reconnected events at a certain κ value depends on the centre-of-mass energy. The difference in mass with respect to the sample without colour reconnection depends

Table 6.5: *FSR values are obtained by removing events which have at least one photon radiated. The ISR effect is estimated by comparing fits when only ISR up to $\mathcal{O}(\alpha^2)$ is considered.*

channel	FSR		ISR	
	ΔM_{W} [MeV]	$\Delta\Gamma_{\mathrm{W}}$ [MeV]	ΔM_{W} [MeV]	$\Delta\Gamma_{\mathrm{W}}$ [MeV]
$qq\mathrm{e}\nu$	4	26	4	26
$qq\mu\nu$	6	25	6	28
$qq\tau\nu$	5	20	0	1
$qqqq$	3	12	0	0

Table 6.6: *Different fragmentation models lead to a shift in the mass and width measurement. These shifts are calculated with respect to JETSET, which is the standard fragmentation model used in the baseline Monte Carlo KandY.*

	$qq\ell\nu$		$qqqq$	
	ΔM_{W} [MeV]	$\Delta\Gamma_{\mathrm{W}}$ [MeV]	ΔM_{W} [MeV]	$\Delta\Gamma_{\mathrm{W}}$ [MeV]
HERWIG	20	2	28	31
ARIADNE	9	6	13	10
fragmentation Systematic	15	4	21	21

on the number of reconnected events, as is shown in figure 6.4 [66] for the fully hadronic channel at a centre-of-mass energy of $189\ \mathrm{GeV}$.

Colour reconnection can be studied in real data by looking at the energy flow between jets, especially between jets from different W's. The results are compared to SK1 Monte Carlo samples with different values of k. The reconnection probability that is most consistent with the data is used to determine the bias due to CR in the measurement of M_{W}. The preliminary LEP combination [66] yields a value of $\kappa = 1.18$ with a 68% CL lower limit of 0.39 and a upper limit of 2.13. This corresponds to a preferred reconnection probability of $49^{+16}_{-26}\%$ in this model at $\sqrt{s} = 189\ \mathrm{GeV}$.

The mass shift due to colour reconnection estimated by the SK1 model is performed with Monte Carlo generated events with a 100% reconnection probability value. The result is shown in table 6.7. This value complies to the result of figure 6.4 around 100% reconnection probability. To estimate the uncertainty due to colour reconnection the central value of 49% is taken. This corresponds to an error of $76\ \mathrm{MeV}$ at $189\ \mathrm{GeV}$. Simulation studies [66] have shown the linear relation in figure 6.5 [66] of the mass shift with respect to the centre-of-mass energy. The errors at the various centre-of-mass energies are estimated from this relation. Combining all the uncer-

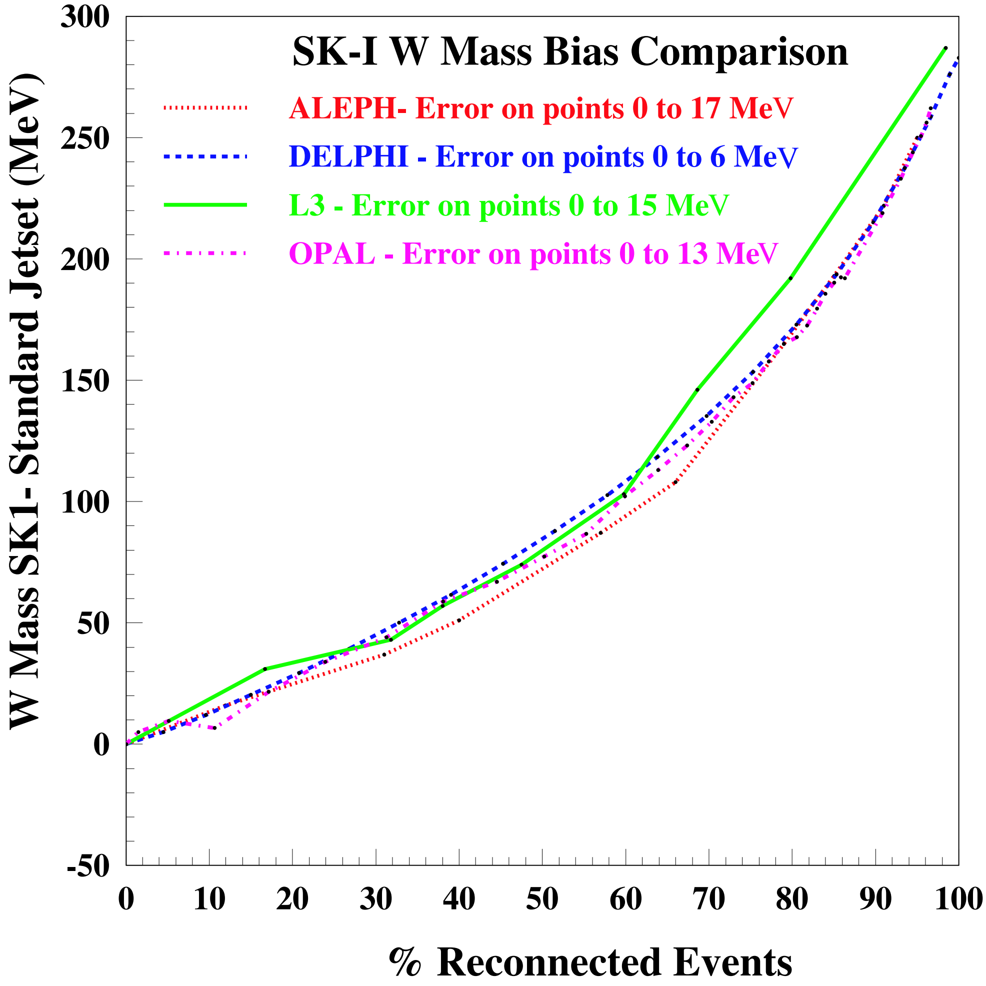

Figure 6.4: *Comparing a SK1 model simulation with a a simulation without colour reconnection as a function of the fraction of events reconnected for the fully hadronic channel at* $\sqrt{s} = 189$ GeV*. The bias at the four LEP experiments show similar sensitivity.*

tainties at the centre-of-mass energies leads to a systematic error of 83 MeV on the mass due to colour reconnection in the SK1 framework. Tabel 6.7 gives a summary of the results.

ARIADNE and HERWIG do not have parameters to adjust the colour reconnection. The average of the observed shifts from the different models is assigned as the systematic error on the mass.

For the uncertainty on the width measurement the average of the observed shift is taken as the uncertainty, but only half of the shift of SK1 is taken in the average.

6.7.2 Bose-Einstein correlations

Another source of uncertainty are Bose-Einstein correlations (BEC). BEC enhances the probability of production of pairs of identical mesons close in phase space. This is observed in LEP1 in hadronically decaying Z bosons. These are correlations between particles originating from the

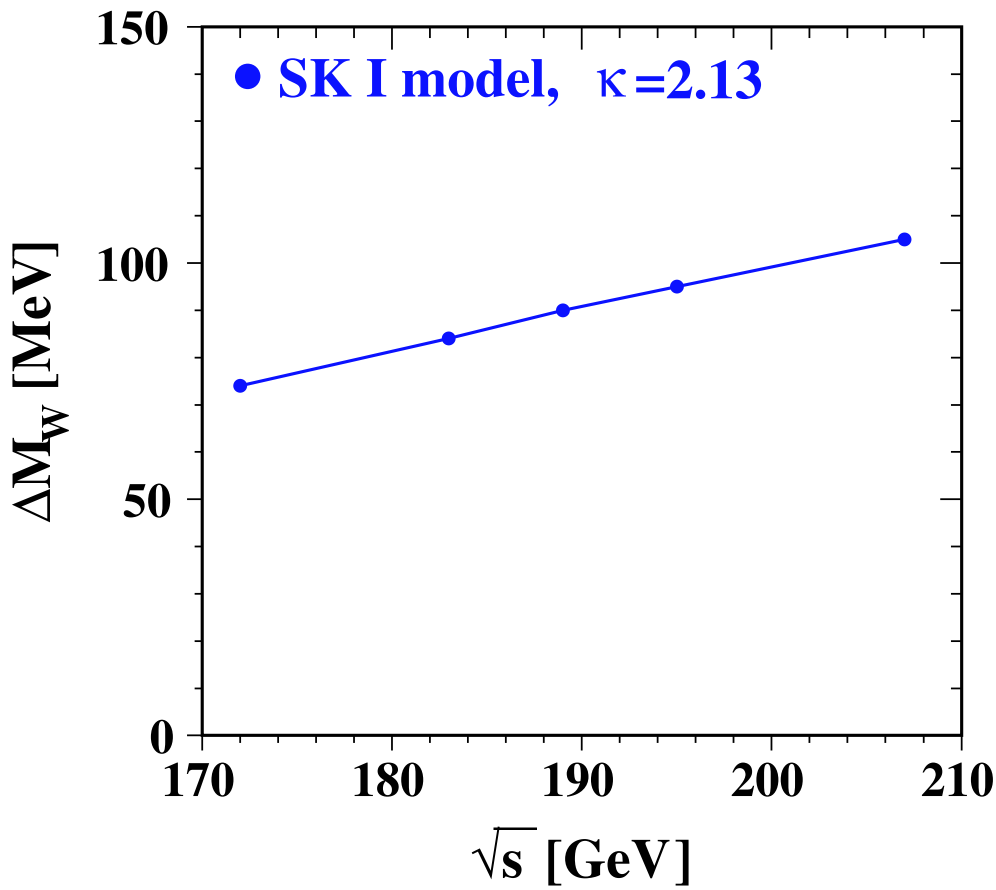

Figure 6.5: *The uncertainty on the mass due to colour reconnection with respect to the centre-of-mass energy for the SK1 model when $\kappa = 2.13$, i.e. when the reconnection probability is 65%.*

Table 6.7: *The error measured from the shift by using the SK1 model is when the reconnection probability is 100%. However, the reconnection probablity determined from the LEP combination analysis leads to a reconnection probability of $49^{+16}_{-26}\%$. Therefore this value is scaled to comply with the determined reconnection fraction.*

	ΔM_{W} [MeV]	$\Delta\Gamma_{\mathrm{W}}$ [MeV]
PYTHIA SK1 (100%)	278	207
Herwig CR	56	24
Ariadne CR2	80	137
CR systematics	73	88

same boson. If this happens between different bosons like in the case of WW decay, a fraction of mis-assigned energy flow could lead to a shift in the mass measurement.

Bose-Einstein correlations studies have been performed by all the four LEP experiments. In L3 the spectra of fully hadronical WW decay is compared to the spectra of mixed semi-leptonic events, in which the leptonic part of the WW decay is removed and the hadronic parts are mixed [67]. This way correlations between particles from the same W are produced, while between-W correlations are not present.

The conclusion from these studies in L3 are that no evidence is found for correlations between different W's. Studies at ALEPH and OPAL show that their results are consistent with no correlations for between-W cross talk. However, DELPHI observes some correlation effects between different W's. The preliminary χ^2 LEP combination indicates a fraction of the values observed of 0.23 ± 0.13 [66] of the full, i.e. inside-W and between-W, PYTHIA BEC.

Table 6.8 shows the bias which is observed if the BE_{23} algorithm from LUBOEI with full BEC is compared with the KANDY samples in which only BEC inside-W exists. In reference to the preliminary LEP combination, one fourth of the difference is taken as the estimated systematic error due to BEC. Calculations from other Monte Carlo models also show a mass shift between 0 and 10 MeV [24–27].

Table 6.8: *The observed shift in the mass and width if Bose-Einstein correlations between-W is taken into account in addition to inside-W BEC.*

	ΔM_{W} [MeV]	$\Delta\Gamma_{\mathrm{W}}$ [MeV]
BE_{23}	30	12
BEC systematic	8	3

6.8 LEP beam energy

The kinematic fit uses the fact that the total energy is conserved in every event. Any error in the beam energy leads to a bias in the reconstructed mass. The uncertainty on the beam energy can be directly translated into a shift in the mass. The error on the mass of the W boson is proportional to the uncertainty on the LEP beam energy,

$$\Delta M_{\mathrm{W}} = \frac{\Delta E_b}{E_b} M_{\mathrm{W}}, \tag{6.2}$$

where E_b is the beam energy, ΔE_b the error on the beam energy and ΔM_{W} the corresponding uncertainty on the W mass.

The measurements of the beam energies at various energy points are highly correlated. Hence it is necessary to take these correlations into account when combining the measurements at the different centre-of-mass energies. The correlation matrix is determined by the LEP Energy Working Group [37]. The uncertainties on the LEP beam energies and the correlation matrix are given in table 6.9.

Table 6.9: *The error on the LEP beam energy at the different centre-of-mass energy is shown together with the correlation matrix in the last 8 rows and columns.*

$\sqrt{s}$	ΔE_b	Correlations of uncertainties on E_b							
[GeV]	[MeV]	189	192	196	200	202	205	207	208
189	10.8	1.00	0.94	0.94	0.94	0.93	0.57	0.50	0.50
192	10.8	0.94	1.00	1.00	1.00	0.99	0.58	0.52	0.52
196	11.6	0.94	1.00	1.00	1.00	0.99	0.58	0.52	0.52
200	11.8	0.94	1.00	1.00	1.00	1.00	0.59	0.52	0.52
202	11.9	0.93	0.99	0.99	1.00	1.00	0.59	0.53	0.53
205	18.5	0.57	0.58	0.58	0.59	0.59	1.00	0.99	0.99
207	20.8	0.50	0.52	0.52	0.52	0.53	0.99	1.00	1.00
208	20.8	0.50	0.52	0.52	0.52	0.53	0.99	1.00	1.00

The results for the channels are presented in table 6.10. From Monte Carlo it is determined that the effect on the width Γ_{W} is about a fourth less than the effect on the uncertainty of the mass.

Table 6.10: *The combined systematic error on the mass and width due to the uncertainties in the LEP beam energy. The correlations between the various centre-of-mass energies are taken into account.*

ΔM_{W} [MeV]				$\Delta\Gamma_{\mathrm{W}}$ [MeV]			
$qqe\nu$	$qq\mu\nu$	$qq\tau\nu$	$qqqq$	$qqe\nu$	$qq\mu\nu$	$qq\tau\nu$	$qqqq$
5	5	5	5	4	4	4	4

6.9 Summary of systematic uncertainties

Table 6.11 and 6.12 gives a summary of the systematic uncertainties on the mass and width measurement due to theoretical modelling, the fit procedure and uncertainties on the measured variables for the four analysed channels. These are the systematic errors for the combination of the centre-of-mass energies from $\sqrt{s} = 189 - 208$ GeV.

The errors are grouped corresponding to correlated and uncorrelated between the different final states. The total numbers are obtained by adding the individual contributions in quadrature.

Table 6.11: *Sources of systematic errors and their respective estimated effect on the mass* M_{W}. *The errors are determined per channel for the measurement at* $\sqrt{s} = 189 - 208$ GeV. *The upper part of the table shows the uncertainties which are uncorrelated between the different final states, while the lower part of the table are the errors which are treated as correlated. Total errors are obtained by adding the individual contributions in quadrature.*

	systematic error on M_{W} [MeV]			
source of uncertainty	$qq\mathrm{e}\nu$	$qq\mu\nu$	$qq\tau\nu$	$qqqq$
Monte Carlo statistics	6	7	13	8
background	4	4	3	16
lepton measurement	11	11	-	-
colour reconnection	-	-	-	73
Bose-Einstein correlation	-	-	-	8
total uncorrelated	13	17	13	76
LEP energy	5	5	5	5
ISR	4	6	0	0
FSR	4	6	5	3
fragmentation	15	15	15	21
jet measurement	3	6	4	2
total correlated	17	19	17	22
total	21	25	21	79

Table 6.12: *Sources of systematic errors and their respective estimated value on the width* Γ_W*. The errors are determined per channel for the measurement at* $\sqrt{s} = 189 - 208$ GeV*. The upper part of the table shows the uncertainties which are uncorrelated between the different final states, while the lower part of the table are the errors which are treated as correlated. Total errors are obtained by adding the individual contributions in quadrature.*

	systematic error on Γ_W [MeV]			
source of uncertainty	$qqe\nu$	$qq\mu\nu$	$qq\tau\nu$	$qqqq$
Monte Carlo statistics	16	20	41	7
background	30	37	87	84
lepton measurement	10	26	-	-
colour reconnection	-	-	-	88
Bose-Einstein correlation	-	-	-	3
total uncorrelated	35	50	96	122
LEP energy	4	4	4	4
ISR	26	28	1	0
FSR	26	25	20	12
fragmentation	4	4	4	21
jet measurement	6	13	22	4
total correlated	38	40	30	25
total	52	64	101	125

Chapter 7

Conclusion and outlook

The previous chapters described the analysis of the W mass measurement. A summary of the obtained results will be presented in this chapter. The measurement will be compared with results of other experiments and their combination.

The following sections will give a brief prospective to future experiments and expectations in the framework of the determination of the W properties.

7.1 Results

The results presented in this thesis are performed on the data collected by the L3 detector during the period from 1998 to 2000. The centre-of-mass energy is increased from $\sqrt{s} = 189$ GeV to 208 GeV during this period. The total integrated luminosity collected by the L3 detector at these energies amounts to $629.3\ \mathrm{pb}^{-1}$.

The W mass and width analysis is performed on the decay of W pairs to the semi-leptonic channels $qq\mathrm{e}\nu$, $qq\mu\nu$ and $qq\tau\nu$ and the fully hadronic channel. A likelihood method with a Monte Carlo re-weighting procedure is used, as is described in chapter 5, to extract M_{W} and Γ_{W} and their statistical errors.

Chapter 6 describes the uncertainties originating from different sources for each channel.

A χ^2 minimisation technique [59] is used to average the individual measurements. The correlations are taken into account by assuming that the measurements are fully correlated or fully uncorrelated in the covariance matrix. For the semi-leptonically decaying W pairs the following mass and width results are obtained:

$$M_{\mathrm{W}} = 80.292 \pm 0.075(stat) \pm 0.040(syst)\ \mathrm{GeV}. \tag{7.1}$$

$$\Gamma_{\mathrm{W}} = 2.36 \pm 0.18(stat) \pm 0.05(syst)\ \mathrm{GeV} \tag{7.2}$$

The same analysis procedure is followed for the fully hadronic channel, which results into:

$$M_{\mathrm{W}} = 80.342 \pm 0.066(stat) \pm 0.079(syst)\ \mathrm{GeV}, \tag{7.3}$$

$$\Gamma_{\mathrm{W}} = 2.18 \pm 0.17(stat) \pm 0.13(syst)\ \mathrm{GeV}. \tag{7.4}$$

Combining these measurements by χ^2 minimisation including the complete systematic errors for which the individual numbers are given in chapter 6 yields:

$$M_{\mathrm{W}} = 80.323 \pm 0.047(stat) \pm 0.051(syst) \text{ GeV}, \tag{7.5}$$

$$\Gamma_{\mathrm{W}} = 2.27 \pm 0.12(stat) \pm 0.07(syst) \text{ GeV}. \tag{7.6}$$

7.2 Mass comparison

The W properties are also measured at LEP by the other three experiments: ALEPH, DELPHI and OPAL. In addition, a complementary study is done at L3, which is used in the final combination of the LEP mass measurement and width measurement.

The measurements done in 1996 at the centre-of-mass energy close to the W pair production threshold at $\sqrt{s} = 161$ GeV exploit the fact that the cross section is sensitive to the W boson mass. This analysis is called the threshold analysis in contrast to the analysis performed at the higher energies, using the mass spectrum to determine the mass and width. Based on the data of [68–71] a summary of the results from the four LEP collaborations is shown in table 7.1.

Table 7.1: W *mass measurement at the production threshold at* $\sqrt{s} = 161$ GeV. *The errors include statistical and systematic contributions.*

Threshold analysis	
experiment	M_{W} [GeV]
ALEPH	80.14 ± 0.35
DELPHI	80.40 ± 0.45
L3	$80.80^{+0.48}_{-0.42}$
OPAL	$80.40^{+0.46}_{-0.43}$

At energies higher than the threshold energy, $\sqrt{s} = 172 - 208$ GeV, the data is analysed through the direct reconstruction of the W invariant mass spectrum. The LEP W mass result is split into a $qq\ell\nu$ and $qqqq$ part. Table 7.2 summarises the obtained results per experiment [66]. The third column in this table gives the combination of both decay channels for the individual experiments.

Studies have been performed which have shown that the four experiments are equally sensitive to colour reconnection effects (as shown in figure 6.4) and Bose-Einstein correlations [66]. Therefore, a common value is used for FSI in calculating the combinations.

The combination of all direct reconstructions of the W boson mass of the four LEP collaborations yields

$$M_{\mathrm{W}}(qq\ell\nu) = 80.411 \pm 0.032(stat.) \pm 0.030(syst.) \text{ GeV}, \tag{7.7}$$

$$M_{\mathrm{W}}(qqqq) = 80.420 \pm 0.035(stat.) \pm 0.101(syst.) \text{ GeV}. \tag{7.8}$$

Table 7.2: *The mass measurement of the* W *boson for centre-of-mass energies from* $172\ \mathrm{GeV}$ *to* $208\ \mathrm{GeV}$ *for the individual collaborations. The result is split into semi-leptonic, fully hadronic channel and the combined value. The results from ALEPH and OPAL include the* $\ell\nu\ell\nu$ *channel in the* $qq\ell\nu$ *results.*

Direct reconstruction			
experiment	M_{W} [GeV]		
	$\mathrm{WW} \to qq\ell\nu$	$\mathrm{WW} \to qqqq$	combined
ALEPH	80.375 ± 0.062	80.431 ± 0.117	80.385 ± 0.058
DELPHI	80.414 ± 0.089	80.374 ± 0.119	80.402 ± 0.075
L3	80.314 ± 0.087	80.485 ± 0.127	80.367 ± 0.078
OPAL	80.516 ± 0.073	80.407 ± 0.120	80.495 ± 0.067
combined	80.411 ± 0.044	80.420 ± 0.107	80.412 ± 0.042

The combined mass value for all channels is:

$$M_{\mathrm{W}}(\mathit{combined}) = 80.412 \pm 0.042\ \mathrm{GeV}. \tag{7.9}$$

The inclusion of the threshold measurement does not change the numerical value of the total result

$$M_{\mathrm{W}}^{LEP} = 80.412 \pm 0.042\ \mathrm{GeV}. \tag{7.10}$$

Figure 7.1 shows the results graphically. The L3 measurement result described in this thesis is somewhat lower than the alternative L3 result but consistent. The complementary L3 results were analysed in 2001 using the KORALW baseline Monte Carlo, whereas the analysis in this thesis is performed with the KandY Monte Carlo, which includes $\mathcal{O}(\alpha)$ corrections in DPA approximation for the four fermion final state.

The W mass is also directly measured by the CDF [72] and D0 [73] experiments at the Tevatron. The combined result is [74]

$$M_{\mathrm{W}}^{Tevatron} = 80.452 \pm 0.059\ \mathrm{GeV}. \tag{7.11}$$

The direct measurements from LEP and Tevatron can be averaged which leads to the world average of:

$$M_{\mathrm{W}}^{Average} = 80.425 \pm 0.034\ \mathrm{GeV}. \tag{7.12}$$

In the Standard Model framework parameters can be determined indirectly via Standard Model relations. The W mass can be derived from a Standard Model fit to electroweak observables to match the experimental data. Using the input parameters measured at LEP1 and SLD yields:

$$M_{\mathrm{W}}^{LEP1+SLD} = 80.373 \pm 0.033\ \mathrm{GeV}. \tag{7.13}$$

If the top mass, m_t, measurements at CDF and D0 are added the result is

$$M_{\mathrm{W}}^{LEP1+SLD+m_t} = 80.386 \pm 0.023\ \mathrm{GeV}. \tag{7.14}$$

Another indirect measurement is done at the NuTeV experiment. In the neutrino-nucleon scattering experiment the electroweak mixing angle $\sin^2\theta_W$ is derived. From this the indirect mass is

$$M_{\mathrm{W}}^{NuTeV} = 80.136 \pm 0.084\ \mathrm{GeV}. \tag{7.15}$$

Measurements done at LEP and Tevatron agree well with each other. The indirect measurements from the electroweak data is also in good agreement with the combination of the direct measurement. However, the result obtained in the NuTeV experiment deviates at the level of 2.9σ from the indirect measurements. There is no systematic effect found that may explain the difference.

Figure 7.2 [74] gives a graphical summary of the presented combined values for the W mass measurements. The upper part of the plot shows the direct measurements whereas the lower part of the plot shows the results obtained from the indirect measurement.

7.3 Width comparison

The W decay width is also measured at LEP by the other collaborations. Table 7.3 shows the results together with the LEP combination.

Table 7.3: *Results of the measurement at the LEP experiments of the* W *width* Γ_{W}.

experiment	Γ_{W} [GeV]
ALEPH	2.13 ± 0.14
DELPHI	2.11 ± 0.12
L3	2.24 ± 0.19
OPAL	2.04 ± 0.18
combined	2.15 ± 0.091

Figure 7.3 shows the agreement between the result from this thesis with the other four results found at LEP.

Direct measurements of Γ_{W} are also performed at CDF and D0. The Tevatron combination from these two experiments yields

$$\Gamma_{\mathrm{W}}^{Tevatron} = 2.102 \pm 0.106\ \mathrm{GeV}. \tag{7.16}$$

Figure 7.4 shows the comparison between the LEP and Tevatron determination. The average of these two measurements is

$$\Gamma_{\mathrm{W}}^{Average} = 2.133 \pm 0.069\ \mathrm{GeV}. \tag{7.17}$$

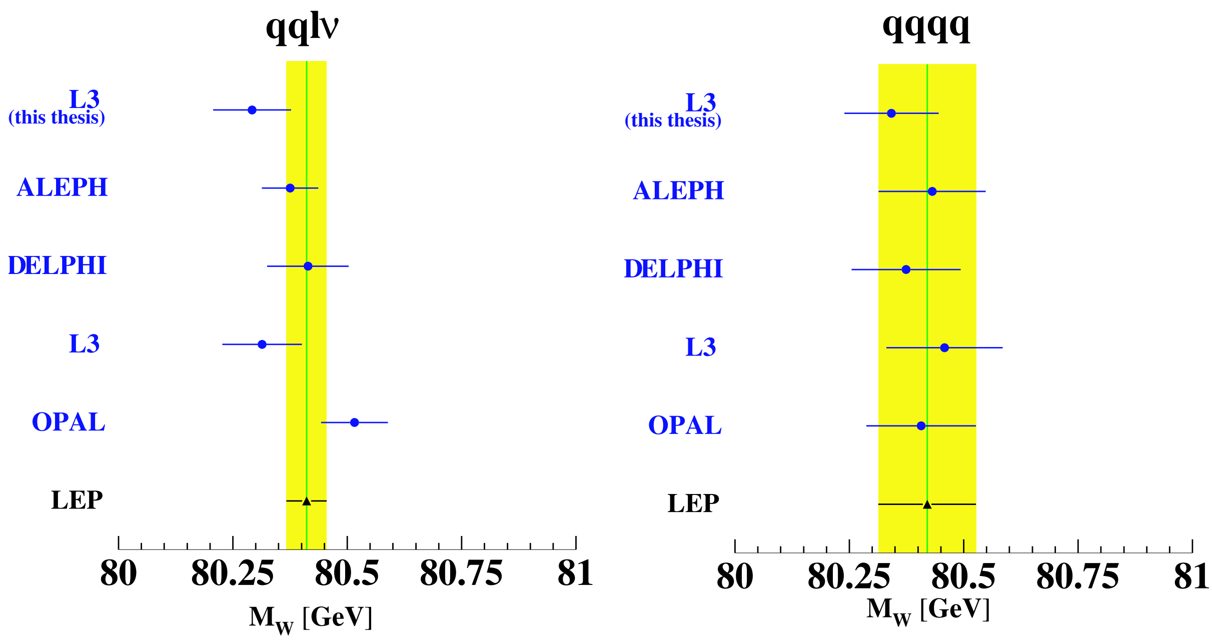

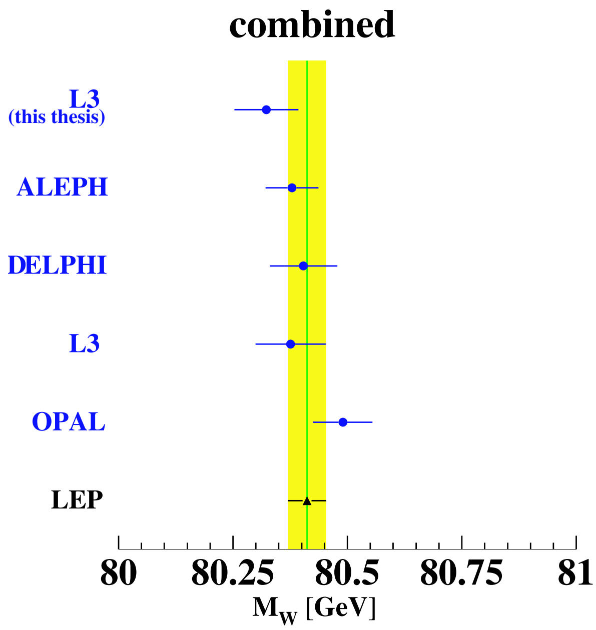

Figure 7.1: *The mass M_{W} per LEP experiment is represented for the $qq\ell\nu$, the $qqqq$ channel and their combination. The combination includes the measurement from the threshold cross section. The LEP combination contains the alternative L3 result.*

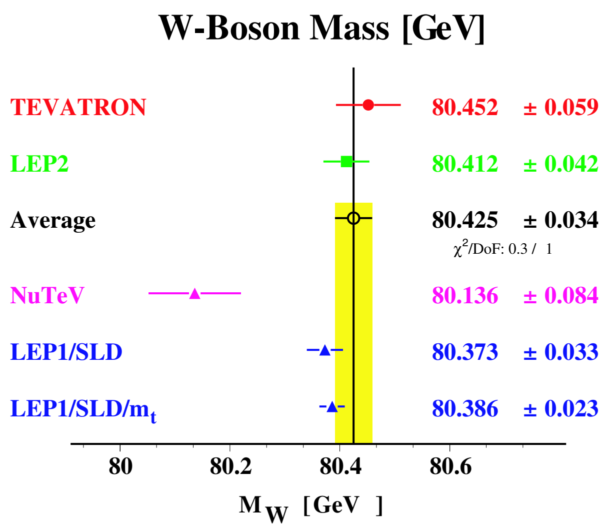

Figure 7.2: *The upper part shows the direct measurements results obtained at LEP and Tevatron. The world average comes from the direct measurements. The indirect measurement is indicated by the triangular point in the graph. Also the NuTeV results, which deviate* 2.9σ *from the indirect measurement, is shown.*

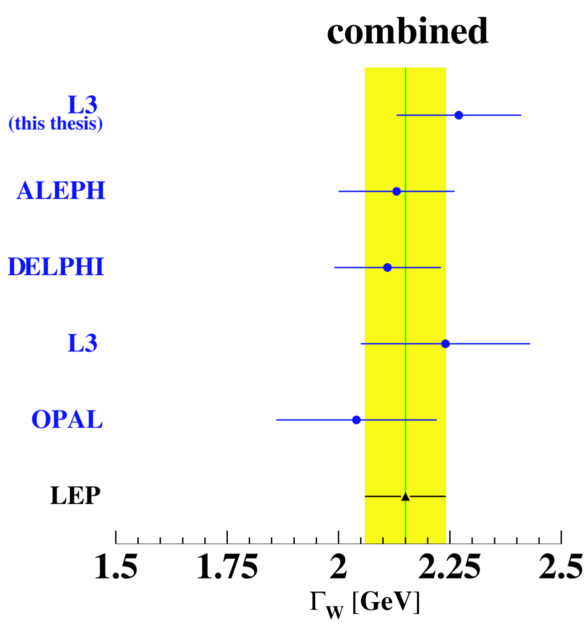

Figure 7.3: *Values found for the width of the* W *boson at all the four experiments at LEP are given individually. The LEP combination includes the alternative L3 result. All the measurements are consistent.*

Just as for the mass of the W, Γ_W can also be determined indirectly from the Standard Model framework parameters measured at LEP1, SLD and Tevatron. A summary is shown in figure 7.4.

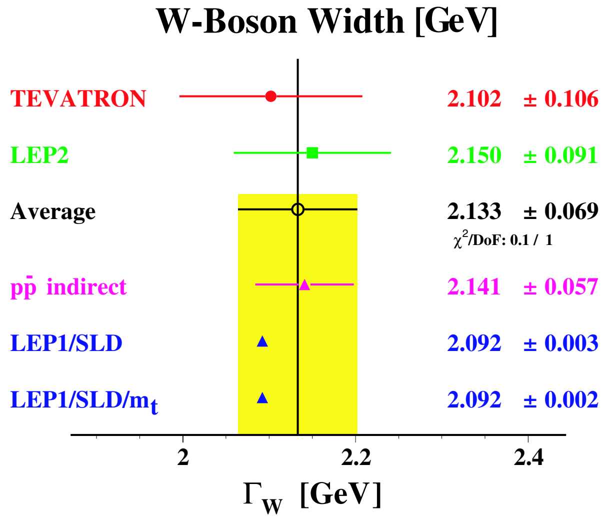

Figure 7.4: *The world average of the* W *boson width is derived from direct measurements of LEP and Tevatron. Indirect electroweak determinations are shown for comparison.*

7.4 Constraint on the Higgs mass

From the electroweak measurements constraints on the mass of the Higgs boson can be inferred.

In section 7.2 the result for the indirect measurement from LEP1 and SLD of M_W is given in equation (7.13). The 68% contour level of the indirect measurements of the W mass and top mass are shown in figure 7.5 [74] as a solid curve. The relation between the W, top and Higgs mass is indicated by the diagonal solid line with the Standard Model prediction of the Higgs mass between 114 and 1000 GeV. As can be seen in figure 7.5 the indirect and direct measurement overlap and prefer a low value of the Higgs mass.

The Standard Model fit provides a constraint on the Higgs mass. The result for the Higgs mass of the fit when all data from LEP, SLD, CDF and D0 is used, corresponds to the minimum of the solid curve in figure 7.6 [74]. This minimum and its one sigma deviation is found at

$$M_H = 113^{+62}_{-42}\ \mathrm{GeV}, \tag{7.18}$$

with non-Gaussian errors considering the Higgs mass enters logarithmically in the fit. The dark grey band around the solid curve takes into account the estimated theoretical uncertainties, due to missing higher order corrections.

The dotted curve shows the variation if the NuTeV results are also considered in the analysis.

From negative results of direct searches of the Higgs boson it follows that the lower limit on M_H is approximately 114 GeV. In figure 7.6 the exclusion region by the direct searches is represented by the grey band. The upper limit on the mass M_H with 95% confidence level, including

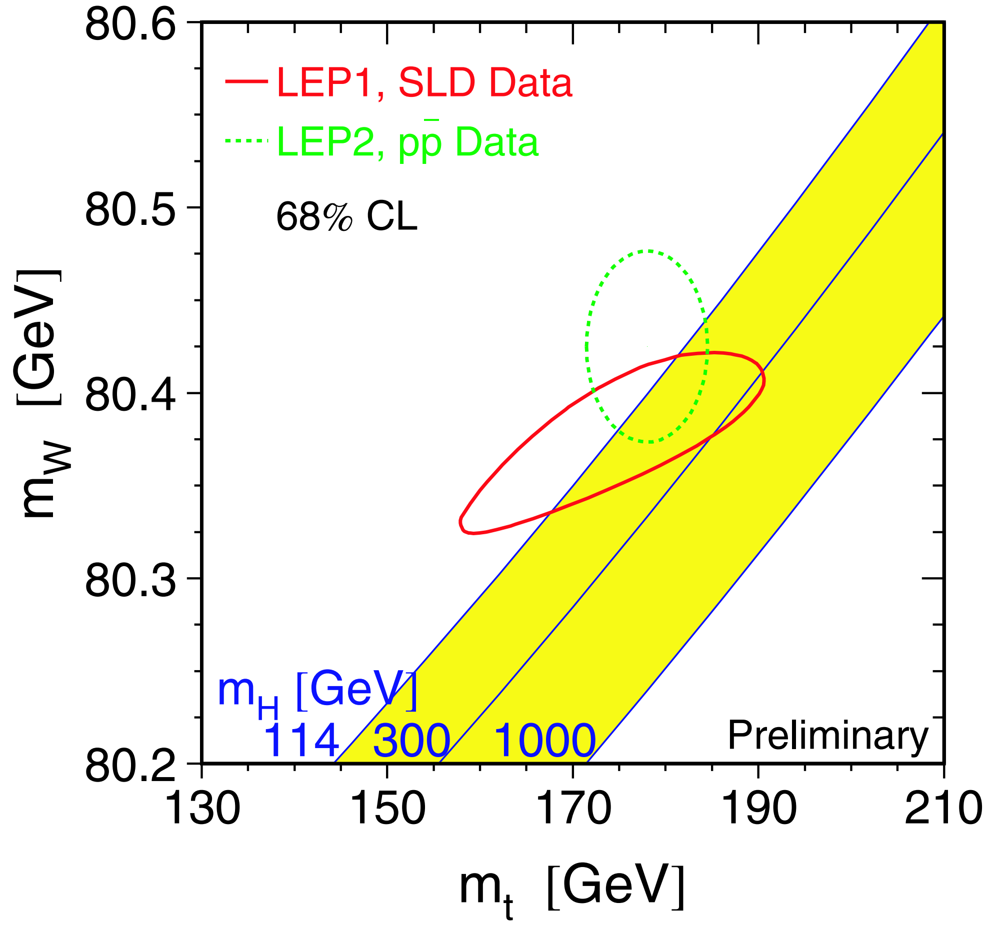

Figure 7.5: *The comparison between indirect (LEP1 and SLD) and direct (LEP2 and Tevatron) measurements of the* W *mass and top quark. The solid contour represents the indirect measurements at* 68% *CL, while the dotted contour is the* 68% *CL from the direct measurement. The band shows the Standard Model prediction for the masses for various values of* M_H.

experimental and theoretical uncertainty is $237\ \mathrm{GeV}$. This constraints the search window to look for the Higgs boson.

7.5 Future colliders

The next generation of colliders to probe deeper into the structure of matter will comprise two complementary types of colliders.

The first type of collider is a circular hadron collider which is currently under construction at CERN, the Large Hadron Collider (LHC). Its very high mass reach and high luminosity will allow possible new physics processes to be covered. High-statistics samples will be used to calibrate the detector and study the standard physics.

The second type of collider is a $\mathrm{e}^+\mathrm{e}^-$ Linear Collider (LC). New particles can be directly produced and studied in detail. Its precision measurements will allow sensitivity to new phenomena

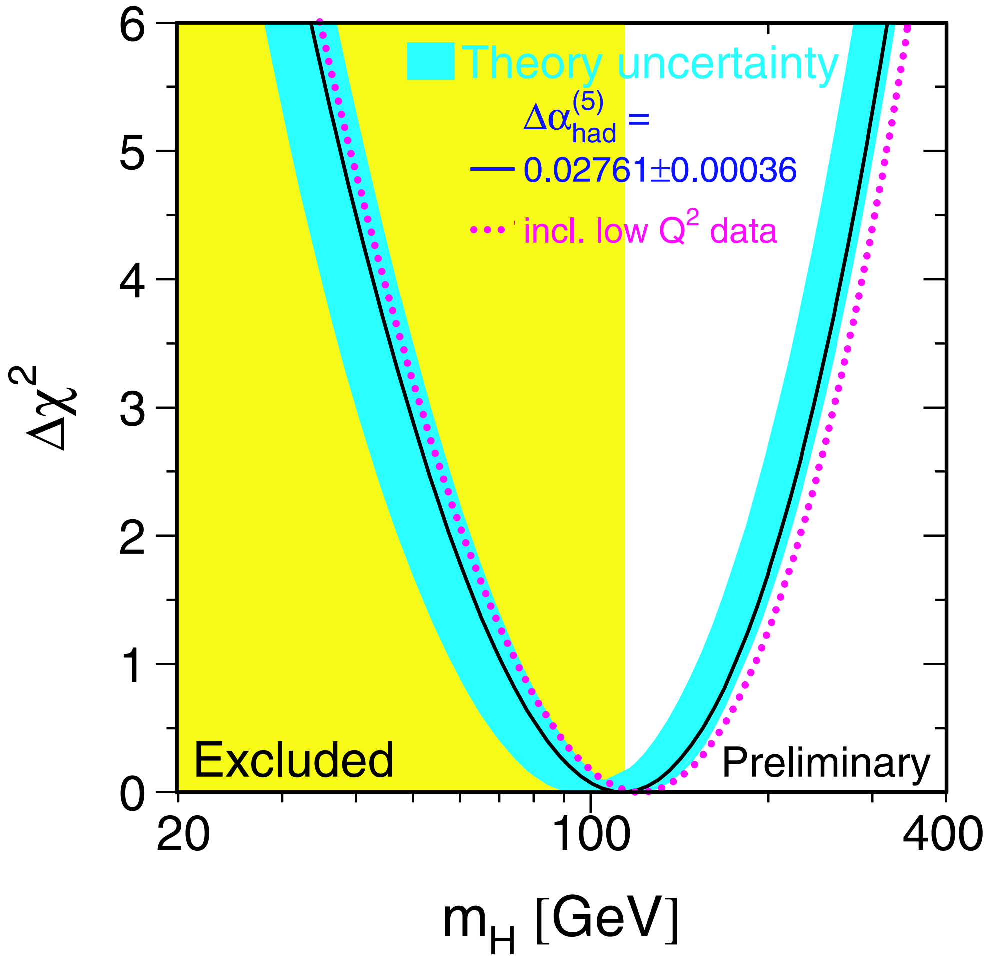

Figure 7.6: *The χ^2 of the Standard Model fit as a function of the Higgs mass. The minimum corresponds to the preferred value of the Higgs mass. The band represents the theoretical uncertainty. Direct searches have excluded the lower values in the shaded band. Inclusion of the NuTeV result is represented by the dotted curve.*

far above the centre-of-mass scale.

7.5.1 Large Hadron Collider

The Large Hadron Collider (LHC) will be operational in 2007. At this accelerator two proton-beams will be collided head-on at a centre-of-mass energy of $14\ \mathrm{TeV}$.

The W boson will be produced by $q\bar{q}$ annihilation.

$$\mathrm{pp} \rightarrow \mathrm{W} + X \tag{7.19}$$

$$\mathrm{W} \rightarrow l\nu_l, \tag{7.20}$$

with $l = e, \mu$, for which the cross section is about $30\ \mathrm{nb}$. Since the boost of the centre-of-mass energy along the beam axis is difficult to determine the longitudinal component of the neutrino cannot be measured. Due to this the transverse mass M_T^{W} is calculated from the transverse momenta of the charged lepton and the neutrino

$$M_T^{\mathrm{W}} = \sqrt{2p_T^l p_T^\nu (1 - \cos\Delta\phi)}, \tag{7.21}$$

where $l = e, \mu$ and $\Delta\phi$ the azimuthal separation between the two leptons. The transverse momentum of the neutrino is obtained from the measured p_T^l and the transverse momentum $\bar{u}$ of the system recoiling against the W.

Figure 7.7 [75] shows the M_T^{W} mass spectrum. The mass could be extracted by a maximum

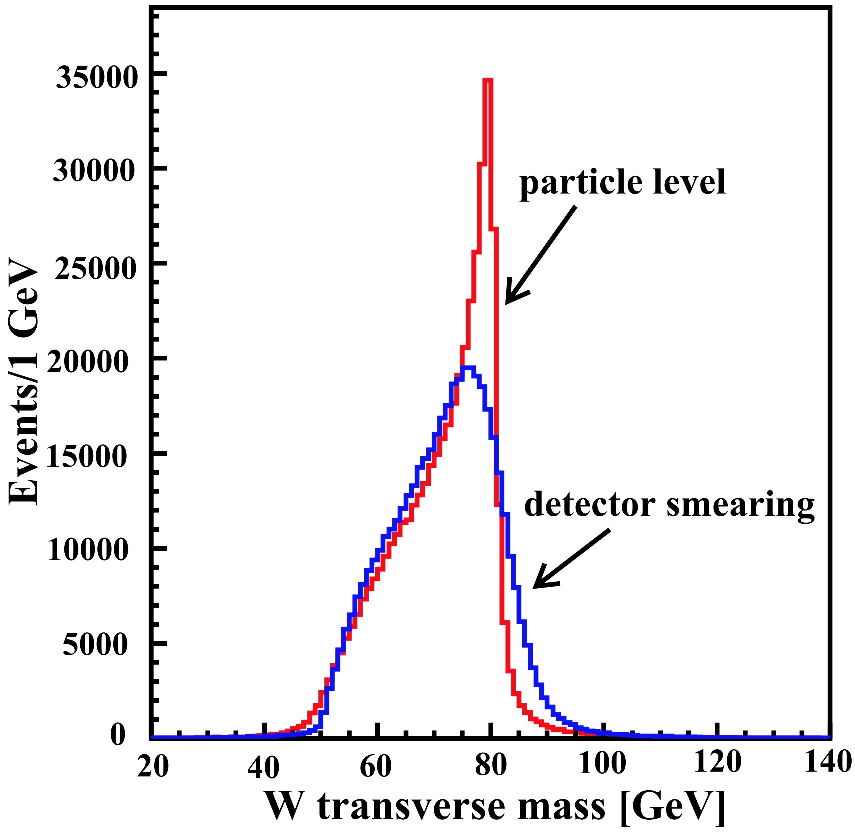

Figure 7.7: *The* W *transverse mass distribution at the LHC. At particle level this distribution exhibits a sharp end-point. Due to detector effects this edge is smeared and the sensitivity to* M_{W} *is reduced.*

likelihood fit to the data with a Monte Carlo probability density distribution. The distribution is smeared out by several effects. This is in particular true for the trailing edge which reduces the sensitivity to the mass. One single bunch crossing may produce multiple interactions, these pile-up events significantly smear the transverse mass. Therefore, the mass measurement is best performed at low luminosity.

LHC will run in the first year with a luminosity of $10^{33}\ \mathrm{cm}^{-2}\mathrm{s}^{-1}$. This will provide an integrated luminosity of the order of $10\ \mathrm{fb}^{-1}$. After the initial phase the instantaneous luminosity will be increased to $10^{34}\ \mathrm{cm}^{-2}\mathrm{s}^{-1}$ collecting an integrated luminosity of about $100\ \mathrm{fb}^{-1}$ a year.

In the first year of LHC running the estimated statistical uncertainty on M_{W} will be smaller than $2\ \mathrm{MeV}$. The dominant part in the error of the mass will come from the systematic uncertainties. The precision of the measurement will be affected by the physics knowledge and detector knowledge. As an illustration table 7.4 [75] shows an estimation of some of the uncertainties at the ATLAS detector.

Table 7.4: *In the first year of LHC running ATLAS is expected to collect a integrated luminosity of* $10\ \mathrm{fb}^{-1}$. *The estimated uncertainty for each lepton family is shown in the table.*

source	ΔM_{W} [MeV]
statistics	< 2
detector performance	
energy and momentum scale	15
energy resolution	5
lepton identification	5
recoil model	5
physics knowledge	
recoil model	5
W width	7
Parton distribution function	10
radiative decays	< 10
p_T^{W}	5
background	5
total	25

The total estimated error for ATLAS and CMS separately is in the order of $25\ \mathrm{MeV}$. Combining both measurements could lead to a precision better than $15\ \mathrm{MeV}$ for M_{W}.

7.5.2 Linear Collider

Another type of collider which is under study is a high-energy high-luminosity electron-positron linear collider (LC). This type of collider could reach a centre-of-mass energy of $500\ \mathrm{GeV}$ with about $500\ \mathrm{fb}^{-1}$ within five years, if a design luminosity of approximately $2 \times 10^{34}\ \mathrm{cm}^{-2} s^{-1}$ is realised.

Although the mass reach of a LC is less than the LHC, it is sensitive to per mill level deviations from the Standard Model, due to its cleaner environment. Such sensitivity corresponds to probing new physics at energy scales as high as $10\ \mathrm{TeV}$ [76].

Such a high-luminosity linear collider will pose an opportunity to measure M_W with a high accuracy. This is best measured with a dedicated run at the threshold of the WW production [77]. The threshold scan requires an accurate calculation of the cross-section dependence on M_W.

The strategy is aimed to look at the WW cross section near threshold where the t-channel electron neutrino exchange process dominates. As in this channel the WW only couples to the $e^+_R e^-_L$ helicity combination, beam polarisation states allow enhancement or suppression of the signal. With a five point scan $160.4 \leq \sqrt{s} \leq 162\ \mathrm{GeV}$ and a point at $\sqrt{s} = 170\ \mathrm{GeV}$ and if a polarisation of 60% can be achieved a precision of $6\ \mathrm{MeV}$ can be attained.

7.6 Muon lifetime

The Standard Model requires 24 parameters in the electroweak sector from experimental measurements. These parameters are six quark masses, six lepton masses, four CKM quark mixing angles and phases, four lepton mixing angles and phases and a set of four other electroweak parameters to be chosen from the set $\{\{\alpha, M_\mathrm{Z}, M_\mathrm{W}, M_\mathrm{H}\}, \{\alpha, M_\mathrm{Z}, \sin\theta_\mathrm{W}, M_\mathrm{H}\}, \{\alpha, M_\mathrm{Z}, G_F\, M_\mathrm{H}\}$. Equation (1.47) gives the interdependence between the M_W on one side and M_Z, α and the Fermi constant G_F on the other side. Their values along with their absolute and relative errors are [78]:

$$\begin{aligned} \alpha &= 1/137.03599911(46) \quad (0.0034\ \mathrm{ppm}); \\ M_\mathrm{Z} &= 91.1876(21)\ \mathrm{GeV} \quad (23\ \mathrm{ppm}); \\ G_F &= 1.16637(1) \times 10^{-5}\ \mathrm{GeV}^{-2} \quad (9\ \mathrm{ppm}). \end{aligned}$$

Accurate precision is achieved for the electroweak parameters M_Z and α in experiments. The uncertainty on G_F can also be improved.

The Fermi constant G_F is directly associated with the muon life time [79]

$$\tau^{-1} = \frac{G_F^2 m_\mu^5}{192\pi}(1 + \Delta q), \tag{7.22}$$

with Δq including higher order QED and QCD corrections calculated in the theory. The theoretical uncertainty is reduced and an experimental result in the order of 0.5 ppm is becoming feasible with respect to the theoretical limit.

The uncertainty on measurement of G_F exists of the following experimental contributions [80]:

$$\frac{\Delta G_F}{G_F} = \sqrt{(\frac{5}{2}\frac{\Delta m_\mu}{m_\mu})^2 + (\frac{1}{2}\frac{\Delta \tau_\mu}{\tau_m u})^2[+(4\frac{m_{\nu_\mu}^2}{m_\mu^2})^2]} = \sqrt{0.38^2 + 9^2 + [10^2/0.3^2]}\ \mathrm{ppm}. \tag{7.23}$$

The m_{ν_μ} is assumed to be non-zero. With the upper bound of $m_{\nu_\mu} \leq 170\ \mathrm{keV}$ the relative shift on G_F is 10 ppm. With the expected reduced upper bound at $30\ \mathrm{keV}$ the uncertainty on G_F becomes in the order of 0.3 ppm The main contribution to the uncertainty in G_F arises from the muon lifetime τ_μ measurement.

The Muon Lifetime ANalysis (μLan) experiment at Paul Scherrer Institute (PSI) is an experiment which aims to measure the positive muon lifetime to 1 ppm precision, thus the Fermi coupling constant to 0.5 ppm [81].

The μLan detector records the decay of approximately 20 muons, which are brought to rest in a target during an accumulation period. The decays are recorded during about 10 muon lifetimes $(22\ \mu s)$. A cycle is repeated until more than 10^{12} decays are recorded.

It is expected to do a full production run at the beginning of summer in 2005 with a fully working experiment.

7.7 Conclusion

This thesis describes the measurement of the mass and width of the W boson. Data recorded with the L3 detector is analysed for centre-of-mass energies between 189 and $208\ \mathrm{GeV}$ taken in the period from 1998 until 2000. This corresponds with a total integrated luminosity of $629.3\ \mathrm{pb}^{-1}$. The invariant mass spectrum of the semi-leptonic and fully hadron decay channels of the W are analysed. The results of these measurements are:

$$M_{\mathrm{W}} = 80.323 \pm 0.069\ \mathrm{GeV}, \tag{7.24}$$

$$\Gamma_{\mathrm{W}} = 2.27 \pm 0.14\ \mathrm{GeV}. \tag{7.25}$$

Direct measurements at LEP and Tevatron gives a world average of:

$$M_{\mathrm{W}}^{Average} = 80.425 \pm 0.034\ \mathrm{GeV}. \tag{7.26}$$

$$\Gamma_{\mathrm{W}}^{Average} = 2.133 \pm 0.069\ \mathrm{GeV}. \tag{7.27}$$

The next generation of colliders will significantly improve the uncertainty on the mass of the W. It is expected that the uncertainty on M_{W} will be better than $15\ \mathrm{GeV}$ for the measurement at LHC. This will be even surpassed by the experiments done at linear collider, which will improve the uncertainty by about a factor of 2 less compared to LHC, resulting in an uncertainty in the order of $6\ \mathrm{MeV}$.

Appendix A

Jet clustering algorithm

A W boson may decay into a quark pair. For the measurement it is essential to reconstruct the momenta of these quarks. However, the quarks cannot be observed as individual particles due to the quark confinement. By fragmentation and hadronisation processes a large number of particles are produced, which are observed in the detector. These particles have to be clustered into jets to represent the primary quarks of the event of interest.

For this purpose the Durham [82] jet finding algorithm has been used in the analysis represented in this thesis.

The Durham algorithm starts with the list of clusters. The energy of the cluster, which can represent a single particle, is determined from the energy deposit in the individual detectors associated with the cluster. These clusters are considered to be massless. Between every cluster pair (i, j) the relative distance y_{ij} is determined from the energies E_i and E_j of the clusters and their mutual angle θ_{ij} by

$$y_{ij} = \frac{2\min(E_i^2, E_j^2)(1 - \cos\theta_{ij})}{E_{vis}^2}, \tag{A.1}$$

where E_{vis} is the visible energy.

The two clusters with the smallest relative distance value y_{ij} are combined together to one object with four-momentum

$$p_k^\mu = p_i^\mu + p_j^\mu. \tag{A.2}$$

The joining procedure is iteratively done until the required final number of objects is reached. These final clusters are the jets. Figure A.1 picturises this procedure schematically. In this thesis four jets for the $qqqq$ and two jets for the $qq\ell\nu$ channel are required.

In the selection of four-jet events the y_{34} value is an important measure for the separation of four-jet events from two and three-jet events. It represents the smallest distance between the two closest jets when a event changes from a four jet to a three jet topology.

Apart from the Durham algorithm several other algorithms exist for the jet clustering. They basically differ from Durham in their definition of the distance measure y_{ij}. MC studies do not show any significant difference in the overall performance for different algorithms used in the analysis [62, 83].

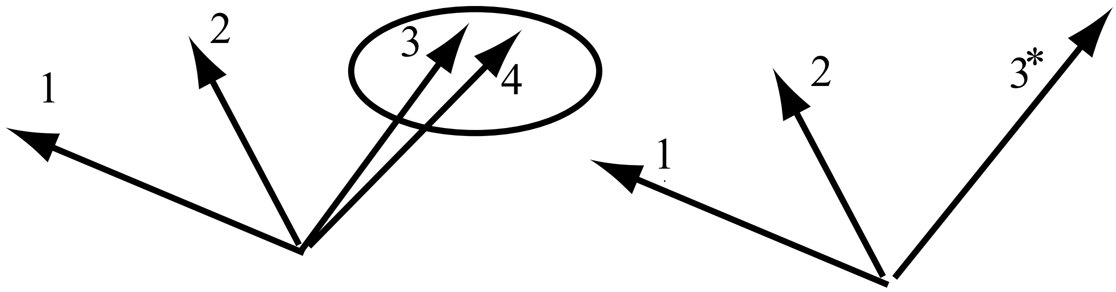

Figure A.1: *Durham algorithm clusters the two object i and j with the smallest mutual angle θ_{ij} and energy $\min(E_i^2, E_j^2)$. Objects 3 and 4 are clustered to a new object number 3^*.*

References

[1] S. Weinberg, *A model of leptons*. Phys. Rev. Lett. **19**, 1264 (1967).

[2] A. Salam, *Weak and electromagnetic interactions*. Originally printed in Svartholm: Elementary particle theory, proceedings of the Nobel symposium held in 1968 at Lerum, Sweden, Stockholm 1968, 367.

[3] T. Muta, R. Najima and S. Wakaizumi, *Effects of the W boson width in* $\mathrm{e^+e^-} \to \mathrm{W^+W^-}$ *reactions*. Mod. Phys. Lett. **A1**, 203 (1986).

[4] V.S. Fadin, V.A. Khoze and A.D. Martin, *On* W^+W^- *production near threshold.* Phys. Lett. **B311**, 311 (1993).

[5] W. Beenakker, F.A. Berends *et al.*, *WW cross-section and distributions*, in *Physics at LEP2*, eds. G. Altarelli, T. Sjöstrand and F. Zwirner, Vol. 1, pp. 79–139. CERN European Organization for Nuclear Research, 1996.

[6] M. Veltman, *Radiative corrections to vector boson masses*. Phys. Lett. **B91**, 95 (1980).

[7] E. Accomando *et al.*, *Four-fermion production in electron-positron collisions*, in *Reports of the working groups on precision calculations for LEP2 physics*, eds. S. Jadach, G. Passarino and R. Pittau, pp. 1–125. CERN European Organization for Nuclear Research, September 2000. CERN 2000-009.

[8] A. Denner, S. Dittmaier, M. Roth and D. Wackeroth, $\mathcal{O}(\alpha)$ *corrections to* $\mathrm{e^+e^-} \to \mathrm{WW} \to \mathrm{4fermions}(+\gamma)$*: first numerical results from RacoonWW*. Phys. Lett. **B475**, 127 (2000).

[9] A. Denner, S. Dittmaier, M. Roth and D. Wackeroth, *Electroweak radiative corrections to* $\mathrm{e^+e^-} \to \mathrm{WW} \to$ *fermions in double-pole approximation — the RacoonWW approach*. hep-ph/0006307, June 2000.

[10] S. Jadach, W. Placzek, M. Skrzypek, B.F.L. Ward and Z. Wąs, *Exact* $\mathcal{O}(\alpha)$ *gauge invariant YFS exponentiated Monte Carlo for unstable* $\mathrm{W^+W^-}$ *production at and beyond LEP2 energies*. Phys. Lett. **B417**, 326 (1998).

[11] S. Jadach, W. Placzek, M. Skrzypek, B.F.L. Ward and Z. Wąs, *Precision predictions for (un)stable* $\mathrm{W^+W^-}$ *pair production at and beyond LEP2 energies*. hep-ph/0007012, November 2001.

[12] S. Jadach, W. Placzek, M. Skrzypek, B.F.L. Ward and Z. Wąs, *The Monte Carlo event generator YFSWW3 version 1.16 for* W*-pair production and decay at LEP2/LC energies*. Comput. Phys. Commun. **140**, 475 (2001).

[13] T. Sjöstrand, *High-energy-physics event generation with PYTHIA 5.7 and JETSET 7.4*. Comp. Phys. Comm. **82**, 74 (1994).

[14] G. Marchesini *et al.*, *HERWIG 5.1 — a Monte Carlo event generator for simulating hadron emission reactions with interfering gluons*. Comp. Phys. Comm. **67**, 465 (1992). HERWIG version 5.9 is used.

[15] L. Lönnblad, *Ariadne version 4: A program for simulation of qcd cascades implementing the color dipole model*. Comp. Phys. Comm. **71**, 15 (1992).

[16] W.J. Metzger, *Tuning PYTHIA 6.2*. L3 note 2745, june 2002.

[17] W.J. Metzger, *Tuning ARIADNE 4.12*. L3 note 2775, august 2002.

[18] W.J. Metzger, *Tuning HERWIG 6.2*. L3 note 2745, june 2002.

[19] T. Sjöstrand and V.A. Khoze, *Does the* W *mass reconstruction survive QCD effects?* Phys. Rev. Lett. **72**, 28 (1994).

[20] T. Sjöstrand and V.A. Khoze, *Soft-particle spectra as probe of interconnection effects in hadronic* WW *events*. Eur. Phys. J. **C6**, 271 (1999).

[21] T. Sjostrand and V.A. Khoze, *On colour rearrangement in hadronic* W^+W^- *events*. Z. Phys. **C62**, 281 (1994).

[22] L. Lönnblad, *Reconnecting coloured dipoles*. Z. Phys. **C70**, 107 (1996).

[23] L. Lönnblad and T. Sjöstrand, *Modeling Bose-Einstein correlations at LEP2*. Eur. Phys. J. **C2**, 165 (1998).

[24] V. Kartvelishvili, R.K. Kvatadze, *Event weights for simulating Bose-Einstein correlations*. Phys. Lett. **B514**, 7 (2001).

[25] K. Fiałkowski, R. Wit, *Implementation of Bose-Einstein interference effects in Monte Carlo generators*. Eur. Phys. J. **C2**, 691 (1998).

[26] S. Mohanty, *Bose Einstein correlations in the Lund model for multijet systems*. Hep-ph/0211174, 2002.

[27] B. Andersson and M. Ringné, *Bose-Einstein correlations in the Lund model*. Nucl. Phys. **B513**, 627 (1998).

[28] E. Fermi, *Versuch einer Theorie der* β*-Strahling*. Z. Phys. **88**, 161 (1934).

[29] Particle Data Group (K. Hagiwara *et al.*), *Review of Particle Physics*. Phys. Rev. **D66**, 010001 (2002).

[30] M.W. Grünewald, *Experimental tests of the electroweak Standard Model at high energies.* Phys. Rep. **322**, 125 (1999).

[31] J.R.J. Bennett, *Design concept for a 100 GeV* e^+e^- *Storage Ring (LEP).* CERN 77-14, (1977).

[32] LEP Injector Study Group, *LEP Design Report Volume I.* CERN-LEP/TH/83-29, (1983).

[33] LEP Injector Study Group, *LEP Design Report Volume II.* CERN-LEP/84-01, (1984).

[34] LEP Injector Study Group, *LEP Design Report Volume III.* CERN-AC/96-01, (1996).

[35] A.A. Sokolov and I.M. Ternov, *On polarization and spin effects in the theory of synchrotron radiation.* Sov. Phys. Dokl. **8**, 1203 (1964).

[36] D. Brand, H. Burkhardt, M Lamont, S. Myers and J. Wenninger, *Accelerator physics at LEP.* Rep. Prog. Phys. **63**, 939 (2000).

[37] LEP Energy Working Group, *Final LEP 2 centre-of-mass energy values.* LEP Energy Working Group Memo, October 2003. http//lepecal.web.cern.ch/LEPECAL/reports/reports.html.

[38] L3 SMD Collaboration, M. Acciarri *et al.*, *The L3 silicon microvertex detector.* Nucl. Instrum. Meth. **A360**, 103 (1995).

[39] M. Acciarri *et al.*, *The L3 silicon microvertex detector.* Nucl. Instrum. Meth. **A351**, 300 (1994).

[40] G. Alverson *et al.*, *Performance of the L3 plastic scintillating fibre calibration system.* Nucl. Instrum. Meth. **A380**, 555 (1996).

[41] A. Straessner, *Measurement of mass and width of the W boson with the L3 detector at LEP.* Ph.D. Thesis, RWTH Aachen, 2000.

[42] M. Skrzypek, S. Jadach, W. Placzek and Z. Wąs, *Monte Carlo program KORALW 1.02 for* W*-pair production at LEP2/NLC energies with Yennie-Frautschi-Suura exponentiation.* Comp. Phys. Comm. **94**, 216 (1996).

[43] M. Skrzypek, S. Jadach, W. Placzek and Z. Wąs, *Initial state QED corrections to* W*-pair production at lep2/nlc - monte carlo versus semi-analytical approach.* Phys. Lett. **B372**, 289 (1996).

[44] F.A. Berends, R. Kleiss and R. Pittau, *All electroweak four-fermion processes in electron–positron collisions.* Nucl. Phys. **B424**, 308 (1994).

[45] F.A. Berends, R. Kleiss and R. Pittau, *Initial-state QED corrections to four-fermions production in* e^+e^- *collisions at LEP2 and beyond.* Nucl. Phys. **B426**, 344 (1994).

[46] T. Sjöstrand *et al.*, *High-energy-physics event generation with PYTHIA 6.1*, October 2000. The PYTHIA manual and more information can be found on the webpage: http://www.thep.lu.se/˜torbjorn/Pythia.html.

[47] S. Jadach, B.F.L. Ward and Z. Wąs, *The precision Monte Carlo event generator $\mathcal{KK}$ for two-fermion final states in* e^+e^- *collisions*. Comp. Phys. Comm. **130**, 260 (2000), hep-ex/9912214.

[48] R. Engel, *Photoproduction within the two-component Dal (p)arton (m)odel: amplitudes and cross sections*. Z. Phys. **C66**, 203 (1995).

[49] R. Engel and J. Ranft, *Hadronic photon-photon interactions at high energies*. Phys. Rev. **D54**, 4244 (1996).

[50] F.A. Berends, P.H. Daverveldt and R. Kleiss, *Radiative corrections to the process* $e^+e^- \rightarrow e^+e^-\mu^+\mu^1$. Nucl. Phys. **B253**, 421 (1985).

[51] S. Jadach, B.F.L. Ward and Z. Wąs, *The Monte carlo program KORALZ version 4.0 for lepton or quark pair production at LEP/SLC energies*. Comp. Phys. Comm. **79**, 503 (1994).

[52] R. Brun *et al.*. *Geant3*, CERN-DD/EE/81-1 (Revised), 1987. The L3 detector simulation is based on GEANT version 3.15.

[53] H. Fesefeldt. RWTH Aachen Report PITHA 85/02, 1985.

[54] B.F.L. Ward, S. Jadach, M. Melles and S.A. Yost, *New results on the theoretical precision of the LEP/SLC luminosity*. Phys. Lett. **B450**, 262 (1999).

[55] L3 Collaboration, P. Achard *et al.*, *Measurement of the cross section of* W*-boson pair production at LEP*. CERN-PH_EP/2004-026, June 2004.

[56] M.A. Rahaman, *Study of* W *properties at LEP200*. Ph.D. Thesis, Tata Institute of Fundamental Research, 2002.

[57] J.D. Bjorken and S.J. Brodsky, *Statistical model for electron - positron annihilation into hadrons*. Phys. Rev. **D1**, 1416 (1970).

[58] R. Nandakumar, W*-Mass determination at the Large Electron Positron collider, CERN*. Ph.D. Thesis, Tata Institute of Fundamental Research, 2000.

[59] A.G. Frodesen *et al.*, *Probability and statistics in particle physics*. Universitetsforlaget, 1979.

[60] F. James, *MINUIT Function minimization and error analysis*. CERN program library long writeup D506.

[61] D.M. Schmidt, R.J. Morrison and M.S. Witherell, *A general method of estimating physical parameters from a distribution with acceptance and smearing effects*. Nucl. Instrum. Meth. **A328**, 547 (1993).

[62] D. van Dierendonck, *Measurement of the W-pair production rate and the W mass using four-jet events at LEP*. Ph.D. Thesis, Universiteit van Amsterdam, 2002.

[63] M. Dierckxsens, *Measurement of the triple gauge-boson couplings in* $\mathrm{e^+e^-}$ *collisions at LEP*. Ph.D. Thesis, Katholieke Universiteit Nijmegen, 2004.

[64] J.P.O. Ricoux, *Optimal pairing algorithm for 4 and 5 jet events at LEP*. L3 note 2786, 2002.

[65] L3 Collaboration, *Measurement of the cross section of* W *pair-production at LEP* . In preparation.

[66] The LEP colaboration ALEPH, DELPHI, L3, OPAL and the LEP Electroweak Working Group the SLD Electroweak and Heavy Flavour Groups, *A combination of preliminary electroweak measurements and constraints on the Standard Model*. LEPEWWG/2003-02, 2003.

[67] J. van Dalen, *Bose-Einstein correlations in* $\mathrm{e^+e^-}$ *events*. Ph.D. Thesis, Katholieke Universiteit Nijmegen, 2002.

[68] ALEPH Collaboration, R. Barate *et al.*, *Measurement of the* W *mass in* $\mathrm{e^+e^-}$ *collisions at production threshold*. Phys Lett. **B401**, 347 (1997).

[69] DELPHI Collaboration, P. Abreu *et al.*, *Measurement and interpretation of the* W*-pair cross-section in* $\mathrm{e^+e^-}$ *interactions at* $161\ \mathrm{GeV}$. Phys Lett. **B397**, 158 (1997).

[70] L3 Collaboration, R. M. Acciarri *et al.*, *Pair-production of* W *bosons in* $\mathrm{e^+e^-}$ *interactions at* $\sqrt{s} = 161\ /\mathrm{GeV}$. Phys Lett. **B398**, 223 (1997).

[71] OPAL Collaboration, K. Ackerstaff *et al.*, *Measurement of the mass of the* W *boson in* $\mathrm{e^+e^-}$ *collisions at* $\sqrt{s} = 161\ \mathrm{GeV}$. Phys Lett. **B389**, 416 (1996).

[72] CDF Collaboration, F. Abe *et al.*, *Measurement of the* W *boson mass*. Phys. Rev. **D52**, 4784 (1995).

[73] D0 Collaboration, S. Abachi *et al.*, *Measurement of the* W *boson mass using electrons at large rapidities*. Phys. Rev. Lett. **85**, 222 (2000).

[74] The LEP Electroweak Working Group. http://lepewwg.web.cern.ch/LEPEWWG/Welcome.html.

[75] ATLAS Collaboration, *ATLAS detector and physics performance. Technical design report. Volume II*, Technical Report CERN/LHCC/99-15, CERN, May 1999.

[76] G. Wieglein, T. Barklow, *LHC/LC study group report* . Draft, April 2004.

[77] R.-D. Heuer, D. Miller, F. Richard, P. Zerwas, *Physics at an* $\mathrm{e^+e^-}$ *linear collider*, in *TESLA The Superconducting Electron Positron Linear Collider with an integrated x-ray laser laboratory*, Vol. Part III. DESY, March 2001. Hep-ph/0106315.

[78] Particle Data Group (S. Eidelman *et al.*), *Review of Particle Physics*. Phys. Lett. **B592**, 1 (2004).

[79] T. van Ritberg and R.G. Stuart, *On the precise determination of the Fermi coupling constant from the muon lifetime*. Nucl. Phys. **B564**, 343 (2000).

[80] Peter Kammel, *Muon capture and muon lifetime* . Nucl-ex/0304019, 2003.

[81] R.M. Carey *et al.*, *A precision measurement of the positive muon lifetime using a pulsed muon beam and the μLan detector*. PSI Experiment R-99.07.

[82] S. Catani, Yu. L. Dokshitzer, M. Olsson, G. Turnock and B. R. Webber, *New clustering algorithm for multi-jet cross-sections in* $\mathrm{e^+e^-}$ *annihilation*. Phys. Lett. **B269**, 432 (1991).

[83] A. Shvorob, *A study of W boson properties with four-jet* $\mathrm{W^+W^-}$ *events at LEP*. Ph.D. Thesis, California Institute of Technology, 2000.

Summary

The Standard Model theory in the weak interaction sector predicts the existence of the spin-1 bosons: the photon γ, the neutral Z boson and the charged W boson. Both the Z and W bosons were discovered in 1983 in $p\overline{p}$ collisions at CERN. The W boson is a massive particle. However, the mass is not predicted by the theory. It has to be determined experimentally. The mass and decay width of the charged W boson is the subject of study in this thesis.

One of the main physics goals of the Large Electron Positron (LEP) collider was the measurement of the mass and width of the W boson. In the first phase of LEP the centre-of-mass energy was approximately equal to the mass of the Z boson. In this phase the properties of the Z boson were extensively studied. In the second phase of LEP the centre-of-mass energy was increased to the W pair production threshold energy and above. These energies made it possible to directly measure the properties of the W particle.

This thesis describes the measurement of the W boson mass and width at the LEP collider with the L3 detector. The analysis presented in this thesis is based on the recorded data from 1998 until 2000. During this period the centre-of-mass energy was increased from 189 to 208 GeV. The total luminosity collected for these years is $629.3\ \mathrm{pb}^{-1}$.

Due to the fact that the W is an unstable particle with a very short lifetime, only the decay products are observed in the detector. The W can decay to a lepton-antineutrino or to a quark-antiquark pair. The four decay channels analysed in this thesis are: $qq\mathrm{e}\nu$, $qq\mu\nu$, $qq\tau\nu$, and $qqqq$ channel. The first three channels are the semi-leptonic channels, while the fourth is called the fully hadronic channel. These events are selected out of other processes which looks very similar to the desired events. They are separately selected, according to their specific properties and analysed.

From the invariant mass distribution of these selected events the mass of the W is determined. The invariant mass is calculated from the energy and angular information of the event. Parameters are measured with a finite precision in the detector. Resolution effects smear the measurements and worsen the reconstruction and therefor the measurement of the mass. A kinematic fit procedure is used in chapter 4 to resolve this problem.

The mass is determined by fitting the invariant mass distribution of the reconstructed selected events with a maximum likelihood method. The cross-section and the differential cross-section, on which the likelihood function depends, are calculated with a so-called boxmethod. One Monte Carlo sample with a certain generated mass and width is reweighted by calculating weight factors for each event in the Monte Carlo to simulate a Monte Carlo with a different mass or width.

Systematic uncertainties arise from the measurement process and the physics behind. Possible sources of systematics effects are studied, including Monte Carlo statistic, background, lepton and jet measurement, initial and final state radiation, fragmentation, colour reconnection, Bose-

Einstein correlation and uncertainties in the LEP beam energy measurement. These effects and results are thoroughly discussed in chapter 6.

Combining all the measurements of the semi-leptonic and fully hadronic decay channels and systematic effects for the data analysed in this thesis yields:

$$M_{\mathrm{W}} = 80.323 \pm 0.047(stat) \pm 0.051(syst)\ \mathrm{GeV},$$

$$\Gamma_{\mathrm{W}} = 2.27 \pm 0.12(stat) \pm 0.07(syst)\ \mathrm{GeV},$$

where the first uncertainty is statistical and the second uncertainty arises from systematic effects. The main contribution in the systematics comes from colour reconnetion, a process that can occur between quarks in the final state, and the fragmentation modelling that describes the evolution of a produced quark to the observed jet.

The next generation of colliders will probe deeper into the structure of matter and will comprise two complementary types of colliders: the Large Hadron Collider (LHC) and a high-energy high-luminosity electron-positron linear collider type. These future colliders will significantly improve the measurement of the W boson mass.

Samenvatting

De Standaard Model theorie voor de zwakke wisselwerking voorspelt het bestaan van de spin-1 bosonen: het foton γ, het neutrale Z boson en het geladen W boson. De Z en W bosonen zijn op het CERN in 1983 ontdekt in $p\overline{p}$ botsingen. Het W boson is een deeltje met een massa. Deze massa wordt echter niet voorspeld door de theorie. Het moet experimenteel bepaald worden. In dit proefschrift worden de massa en vervalbreedte van het W boson bestudeerd.

Een van de fysische hoofddoelen van de Large Electron Positron (LEP) versneller was het meten van de massa en vervalbreedte van het W deeltje. Gedurende de eerst fase van LEP was de zwaartepuntsenergie ongeveer gelijk aan de massa van het Z boson. In deze eerste fase werden de eigenschappen van het Z boson geanalyseerd. Tijdens de tweede fase van LEP werd de zwaartepuntsenergie verhoogd naar de grens waar W-paar productie mogelijk is en hoger. Bij deze hoge energieëen is het mogelijk om de eigenschappen van het W deeltje direct te meten.

In dit proefschrift wordt de meting van de massa en vervalbreedte van de W beschreven. De data opgeslagen in de periode van 1998 tot en met 2000 is geanalyseerd hierin. Tijdens deze periode is de zwaartepuntsenergie verhoogd van 189 tot 208 GeV. De totale luminositeit voor deze jaren is $629.3\ \mathrm{pb}^{-1}$.

Het W boson is een instabiel deeltje met een korte levensduur. Slechts de vervalproducten van de W worden waargenomen in de detector. Het W deeltje kan vervallen naar een lepton-antineutrino of naar een quark-antiquark paar. De vier vervalkanalen, $qq\mathrm{e}\nu$, $qq\mu\nu$, $qq\tau\nu$, en $qqqq$ zijn geanalyseerd. De eerste drie kanalen zijn de zogenaamde semi-leptonische kanalen en de vierde is de volledig hadronische kanaal. Deze processen zijn geselecteerd uit een scala van processen die erg veel lijken op de gewenste gebeurtenis. Elk kanaal is afzonderlijk geselecteerd naar gelang de specifieke eigenschappen en geanalyseerd.

Uit de invariante massaverdeling van deze geselecteerde gebeurtenissen wordt de W massa bepaald. De invariante massa wordt berekend aan de hand van de energie- en hoekinformatie van een gebeurtenis. De meting van parameters in de detector hebben een eindige precisie. Resolutie effecten smeren de meetwaarden en verslechteren de reconstructie en daarmee de totale meting. In hoofdstuk 4 wordt de kinematisch fit toegepast om dit probleem op te lossen.

Met behulp van een maximum likelihood methode fit aan de invariante massadistributie van de geselecteerde gebeurtenissen is de massa bepaald. De likelihood functie hangtaf van de werkzamedoorsnede en de differentiële werkzamedoorsnede. Deze zijn bepaald met behulp van de boxmethode. Omdat één Monte Carlo bestand beschikbaar is per dataset met een gegeven massa en vervalbreedte, moet deze Monte Carlo herwogen worden om Monte Carlo's met een andere massa en breedte te simuleren. Deze herweging gebeurt door voor iedere gebeurtenis uit de Monte Carlo een gewichtsfactor te berekenen.

Systematisch onzekerheden in de meting komen van de meting en van fysische processen.

Mogelijke bronnen van systematische fouten zijn: Monte Carlo statistiek, achtergrond processen, de meting van de lepton en jet, initial en final state straling, fragmentatie, colour reconnection, Bose-Einstein correlatie en onzekerheden in de bepaling van de bundelenergie. Deze effecten en de resultaten zijn in hoofdstuk 6 gegeven.

De combinatie van alle metingen van de semi-leptonische en volledig hadronische vervalkanalen en systematische effecten voor de data die in dit proefschrift zijn geanalyseerd is:

$$M_{\mathrm{W}} = 80.323 \pm 0.047(stat) \pm 0.051(syst)\ \mathrm{GeV},$$

$$\Gamma_{\mathrm{W}} = 2.27 \pm 0.12(stat) \pm 0.07(syst)\ \mathrm{GeV},$$

waarbij de eerste onzekerheid de statistische fout is en de tweede de onzekerheid afkomstig is van systematische effecten. De systematische fout wordt voornamelijk gedomineerd door de colour reconnection, een proces dat tussen twee quarks kan plaats vinden, en van de fragmentatie, die de evolutie van een geproduceerde quark naar de waargenomen jet beschrijft.

De volgende generatie versnellers zullen in staat zijn om dieper in de structuur van materie te gaan kijken. Er zullen twee type complementerende versnellers zijn: de Large Hadron Collider (LHC) en een mogelijke hoog energetisch hoog luminositeits electron-positron lineair versneller. Deze versnellers zullen de meting van de massa van het W boson significant verbeteren.

Dankwoord

Tenslotte de laatste pagina van dit proefschrift. Dit was niet mogelijk geweest dankzij de hulp van vele personen die op hun eigen wijze een bijdrage hebben geleverd aan de voltooiing ervan. Deze pagina wil ik dan ook wijden aan het bedanken van een aantal personen in het bijzonder, zonder onrecht te willen doen aan anderen.

Allereerst wil ik mijn promotor Frank Linde bedanken voor het vertrouwen, de vele adviezen en suggesties die ik heb gekregen. Daarnaast wil ik mijn co-promotor Paul de Jong bedanken voor de begeleiding, steun en motivatie die hij me heeft gegeven tijdens mijn promotie.

I specially enjoyed working with Arno Straessner. I learned almost all the aspects of the W analysis from him. The discussions with him and Luca Malgeri were very fruitful and gave me more insight in the matter.

De oudere generatie L3 promovendi, Auke-Pieter Colijn, Sandra Muijs, Tasja van Rhee en Daniël van Dierendonck hebben me bij de eerste stappen voorzien van vele handige tips.

Gedurende mijn verblijf op het CERN heb ik mijn kantoor gedeeld met Robert van Gulik en Mark Dierckxsens die naast een bron van gezelligheid een onmisbare informatiebron waren van handige tips en trucs.

I have met a lot of people at CERN who were always prepared to answer my questions and fulfil my request regarding my analysis. The list would be to long to name all of them. Therefor, I only say thank to you all.

Mijn verblijf op het CERN is een onvergetelijk ervaring geweest. Mede dankzij de vele plezierige uitstapjes heb ik een geweldige tijd beleefd in Genève samen met Karin, Rutger, Cathelijne, Mark, Robert en Martin. Samen met hun heb ik mijn nieuwe hobby, het snowboarden, ontdekt.

Ook op het NIKHEF heb ik met veel plezier gewerkt. De discussies tijdens het werk en de pauzes waren niet alleen plezierig maar ook heel leerzaam. Ook hier is de lijst van namen te lang om op te noemen. Ik volsta met een ieder van ze veel succes in de toekomst te wensen.

De laatste stap van het onderzoek en de analyse is het manuscript schrijven. Dit is zeer enerverend en ik ben Robert van Gulik en Martin Blom dankbaar voor het lezen van de verschillende versies van mijn manuscript. Chandra Dewkalie heeft het hele concept voor de omslag bedacht en uitgewerkt en Ashwien Ramdas zorgde voor de Photoshop ondesteuning.

Degenen die mij altijd hebben gesteund en gemotiveerd in mijn mooiste en moeilijkste momenten, zonder wie de voltooiing van dit werk niet mogelijk zou zijn geweest, zijn mijn zussen en zwagers, Sharmila, Manoj, Nanda en John.

Mijn moeder heeft mij altijd met veel geduld en liefde bijgestaan in deze periode die met pieken en dalen ging. Haar vertrouwen en onmisbare steun was van onschatbare waarde.

Alles met een begin heeft een eind. Elk eind is het begin van een nieuw begin. Zo ook de voltooiing van dit proefschrift. Hij heeft het begin mogen meemaken maar helaas niet de

voltooiing, maar ik weet dat er één persoon is die nog trotser zou zijn dan mijn moeder. Daarom is de laatste pagina, de laatste alinea, de laatste zin en het laatste woord voor hem, mijn vader.